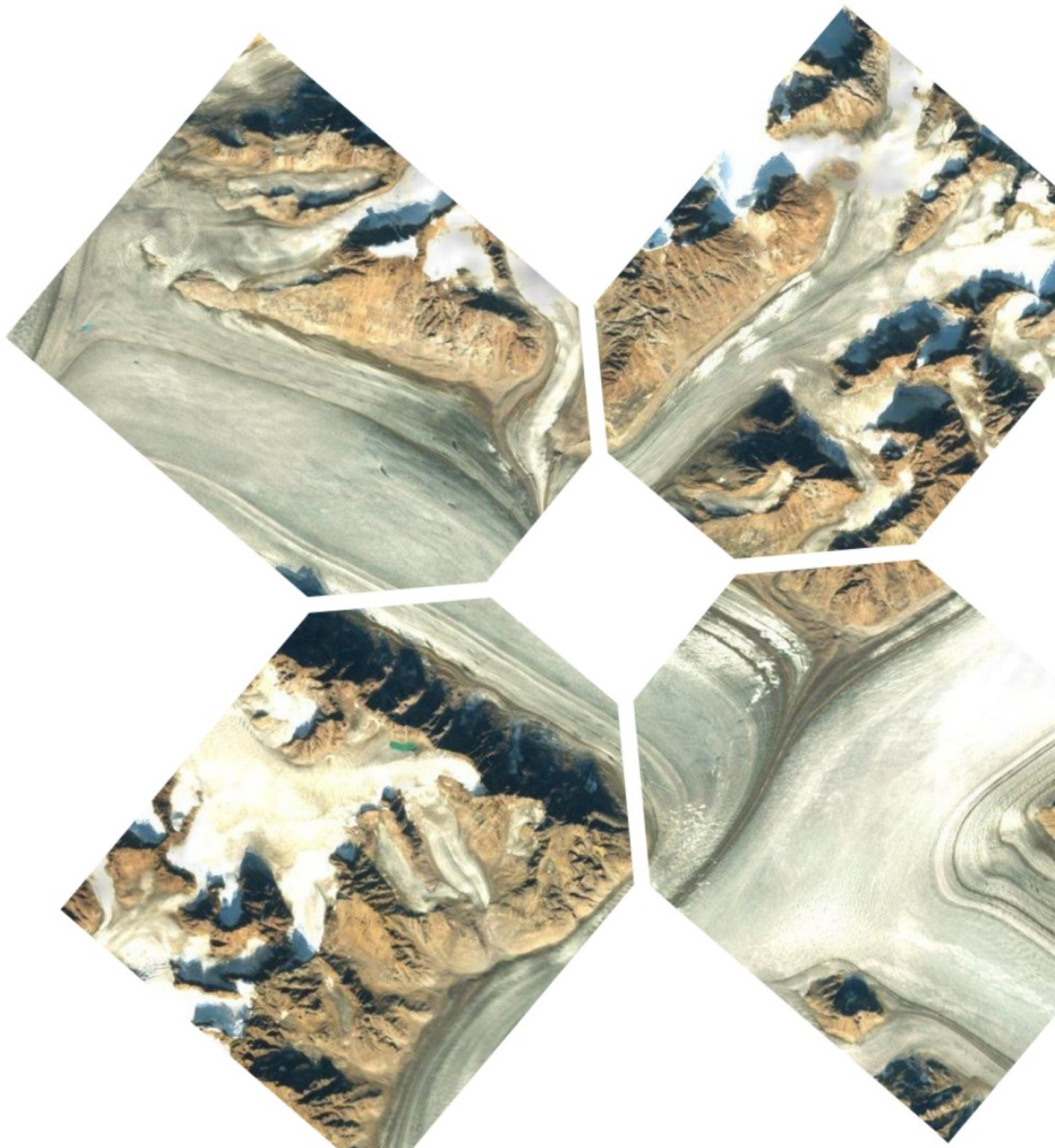


Assessing the Thermo-Mechanical Behaviour of the CORE Hinge for the Deployable Space Telescope

T.R. Gritter



Assessing the Thermo-Mechanical Behaviour of the CORE Hinge for the Deployable Space Telescope

by

T.R. Gritter

to partially obtain the degree of Master of Science
at the Delft University of Technology.
to be defended publicly on Thursday November 5, 2020 at 14:30.

Student number: 4208250
Project duration: February 13, 2020 – November 5, 2020

Thesis committee:

Chair	Dr. J. Guo	TU Delft, SSE
Daily Supervisor	Ir. J. Bouwmeester	TU Delft, SSE
Internal	Dr. Ir. J.M. Kuiper	TU Delft, SSE
External	Ir. M.C. Naeije	TU Delft, A&SM

Cover image: Glaciers on Greenland [28]

Summary

As Earth Observation (EO) satellites require high ground resolutions to be able to take sharp pictures of the ground, their optics need large apertures. In 2014, the Deployable Space Telescope (DST) has been proposed to achieve a large aperture with a telescope that also has a low mass and small launch volume. This telescope will use foldable optical elements, which will be deployed after launch to achieve the aforementioned goals. Currently, the conceptual optical design of the telescope has been carried out and the conceptual mechanical design is well underway. The next step in the design of the DST is to analyse whether the current system complies with stipulated requirements. This phase has been started by two MSc. students, who performed a thermal analysis and mechanical and thermal experiments on one of the components of the Secondary Mirror Support Structure (SMSS), the Compliant Rolling-Element (CORE) hinge, which is a hinge that operates with minimal friction. However, there is still a need for a thermal and a mechanical analysis of the CORE hinge, to be able to evaluate the compliance of the CORE hinge of the DST to the functional requirements. To fulfil this need, the mechanical behaviour of the CORE hinge under the influence of thermal loads is analysed in this thesis. This is done by means of a thermal analysis and a mechanical analysis of the CORE hinge, where the results of the thermal analysis will serve as inputs to the mechanical analysis.

For the thermal analysis, two models have been built. The first model is a geometric model, in which the thermal inputs to the hinge and the heat transfer coefficients within the hinge are determined. The second model is a thermal model, which is used to determine the temperature progression throughout the hinge. The thermal analysis has been divided into two parts. The first part corresponds to the final minutes before the DST enters eclipse, while the second part corresponds to the first minutes after the DST exits the eclipse. The highest temperatures of the CORE hinge are reached in the entry phase. Furthermore, the components of the hinge with the highest temperatures are the strips, the hottest strip being the middle strip, at 18 °C.

With the mechanical analysis, the lateral stability and in-orbit drift behaviour of the CORE hinge have been identified, as well as the angular in-orbit drift behaviour. The lateral stability along the optical axis of the CORE hinge is $4.2 \cdot 10^{-4} \mu m$. This means that the stability requirements are met.

The maximum lateral in-orbit drift is $9.9 \mu m$ and the angular in-orbit drift around the x and y axes is 80.5 and $54 \mu rad$, respectively. Therefore, the in-orbit drift requirements are not satisfied. In order to solve this, it is proposed to elongate the baffle of the DST, such that the CORE hinge is protected from solar radiation for the whole orbit.

Two recommendations have resulted from this thesis. First, it is recommended to carry out mechanical tests with the SMSS to determine its compliance with the functional requirements. Additionally, it is recommended to perform thermal and mechanical tests of the top CORE hinge, the results of which can be used to validate the thermal and mechanical models.

Preface

Over the course of the past eight years, I have been studying at Delft University of Technology with pleasure, learning a lot about aerospace engineering in general and space systems engineering in particular. The conclusion of this period is the MSc. thesis, during which multiple months are dedicated to conducting research into a self-chosen subject: the CORE hinge of the Deployable Space Telescope.

This thesis report is the result of a year of hard work, a year that turned out very different than expected because of the outbreak of COVID-19. However, I have continued to work hard on my thesis and I am proud of what I have achieved.

I would like to thank my supervisor, Jasper Bouwmeester, for his guidance and for the pleasant discussions on the direction of my thesis. Furthermore, I would like to thank my parents, who have welcomed me with open arms when I decided to move back to Amersfoort for the duration of the first Corona wave.

I hope that you will enjoy reading my thesis report, and if you have any questions, please feel free to contact me.

Thijs Gritter
Delft, October 22 2020

Contents

Summary	iii
List of Figures	ix
List of Tables	xi
1 Introduction	1
2 Deployable Space Telescope Project Overview	3
2.1 Overview of Previous Work	3
2.2 Optical Design	4
2.2.1 Optical Layout	4
2.2.2 Aberration Correction System	5
2.3 Mechanical Design	5
2.3.1 Primary Mirror Support Structure	6
2.3.2 Secondary Mirror Support Structure	6
2.3.3 Baffle Design	8
2.4 Analysis of the CORE Hinge	9
2.5 Future work	10
2.5.1 General overview	10
2.5.2 Characterising CORE hinges	11
2.5.3 Thesis Need and Objective	11
3 High-Precision Deployable Structures	13
3.1 Micro-dynamics	14
3.1.1 Load-displacement Non-linearities	14
3.1.2 Hysteresis	14
3.1.3 Micro-lurch	17
3.2 Modelling of Micro-dynamics	18
3.2.1 Hysteresis	18
3.2.2 Micro-lurch	18
4 CORE Hinges	21
4.1 Compliant Rolling-Element	21
4.2 History of development	22
5 Overview of the Thesis Methodology	25
5.1 Thermal Analysis	25
5.2 Thermal Results to Mechanical Input	25
5.3 Mechanical Analysis	26
5.4 Requirements	26
6 Thermal Analysis Method Selection	27
6.1 Lumped Parameter Method	27
6.1.1 General Information	27
6.1.2 Advantages and Disadvantages	28
6.2 ESATAN	28
6.2.1 Using ESATAN	29
6.2.2 Solving the Thermal Model	29
6.3 Selecting a Method for the Thermal Analysis	30
6.3.1 Three Possible Methods	30
6.3.2 The Method Selection Process	32

7	The Geometric Mathematical Model	35
7.1	DST CORE Hinge Geometric Model	35
7.2	Geometric model for the DST	36
7.3	Building the geometric model of the DST CORE Hinge	36
7.3.1	Defining the Geometry	36
7.3.2	Defining the Radiative Case	39
7.3.3	Running the Radiative Case	42
7.4	The Resulting Geometric Model of the CORE Hinge.	43
7.4.1	The CORE Hinge	43
7.4.2	The Other Geometries	46
7.4.3	Comparison to the DST CORE Hinge.	46
8	Thermal Mathematical Model	49
8.1	Building the TMM of the CORE Hinge.	49
8.1.1	CORE Hinge TMM Creation	49
8.1.2	Running the Thermal Model	53
8.2	Influence of Lumped Parameter Method on Results.	54
8.2.1	The Method	54
8.2.2	Results	54
9	Thermal Analysis and Results	57
9.1	Method of the Analysis	57
9.1.1	Hinge of Interest	58
9.1.2	Input.	58
9.1.3	The analysis	59
9.2	Results	60
9.2.1	Entry Phase	61
9.2.2	Exit Phase	62
9.2.3	Conclusions for the mechanical analysis.	64
9.3	Discussion of the Results	64
10	Mechanical Analysis	67
10.1	Changing the method.	67
10.2	Mechanical Model	68
10.2.1	Representing the CORE Hinge	68
10.2.2	Modelling Stiffness and Friction	68
10.2.3	Inputs to the model	69
10.3	Analysis Methodology.	69
10.3.1	Assumptions.	70
10.3.2	Determine the Thermal Loads	70
10.3.3	Determine the Stability	70
10.3.4	Determine the In-Orbit Drift.	71
10.4	Results of the Mechanical Analysis	72
10.5	Discussion of the Mechanical Results	74
11	Conclusions	77
12	Recommendations	79
	Bibliography	81
A	Results of Thermal Analysis	85
A.1	Entry Phase	85
A.2	Exit Phase	86
B	Requirements	89

List of Figures

2.1	The DST team members and what they have worked on. Black arrows indicate work flow, white arrows indicate that members have worked on the project at the same time	4
2.2	Optical lay-out of the DST [9]	5
2.3	Focal plane of the DST [9]	5
2.4	Top and bottom view respectively of the T-frame that supports M1 [38][18]	6
2.5	Schematic of the pre and after deployment positions of the M1 deployment system [7]	6
2.6	Illustration of (a) the position before deployment and (b) the position after deployment [27]	7
2.7	The bottom and top CORE hinges, respectively [38]	8
2.8	View of the spider	8
2.9	Schematic view of the baffle including the SMSS (based on the figure from Arink, 2019)	9
2.10	Schematic showing the locations and names of the thermocouples [23]	10
2.11	Thermal model of Leegwater [23]	10
3.1	A conventional pin-clevis joint with indicated planes of symmetry [20]	13
3.2	Build-up of the non-linear load-displacement response of a mechanical joint [19]	15
3.3	Simplified representation of a hysteresis loop [19]	15
3.4	Relation between the magnitude of the load on a high precision deployment mechanism and the amount of hysteresis in this mechanism [19]	16
3.5	Indication of the inflection point on the hysteresis curve [42]	17
3.6	Micro-lurch behaviour identified in Minimast micro-dynamics experiments [41]	17
3.7	Equilibrium zone identified in Minimast micro-dynamics experiments [41]	17
3.8	Simplified schematic view of frictional load transfer across a mechanical interface [19]	18
3.9	Schematic view of the hysteresis model [19]	18
3.10	Hysteresis behaviour of the simplified model [19]	19
3.11	Schematic view of Warren's model [42]	19
4.1	Illustration of the rolling motion of a CORE hinge [14]	21
4.2	Schematic visualisation of the Rolamite concept [44]	22
4.3	Three phases in the manufacturing of the CORE hinge, with the rightmost depicting the final product [5]	22
4.4	Tension stable CORE hinge concept, with a) a stable equilibrium and b) an unstable equilibrium [13]	23
4.5	Schematic of the two DST CORE hinge concepts [18]	23
4.6	Renders of the top and root CORE hinges, respectively [18]	23
6.1	Node N0 and the four adjacent nodes	28
6.2	Graphical representation of the Input-by-Hand Method	31
6.3	Graphical representation of the combinationmethod	31
6.4	Graphical representation of the standard method	31
6.5	Definition of s , dA_i , dA_j , θ_i and θ_j	33
7.1	Optical Set definition window with the values of the DST CORE Hinge Coating.	37
7.2	The Geometric window of the geometry definition	38
7.3	The Properties window of the geometry definition	38
7.4	Environment definition window for the CORE hinge model	40
7.5	Orbit definition window for the CORE hinge model	40
7.6	Temperature distribution of the Earth from Temperature matrix	41
7.7	Graphical representation of the orbital parameters i , ω and Ω . Obtained from [40] and slightly altered for clarity	42

7.8	Visualisation of the Radiative Case	42
7.9	Upper cam with different parts in colour	44
7.10	Geometric model of the plate	44
7.11	Geometric model of the strips	44
7.12	Side view of the CORE hinge model	45
7.13	Side view of the DST CORE hinge	45
7.14	Front view of the CORE hinge model	45
7.15	Front view of the DST CORE hinge	45
7.16	Top view of the CORE hinge model	45
7.17	Top view of the DST CORE hinge	45
7.18	The full geometric model	46
7.19	Illustration of the difference between the start of the gap (yellow) and the start of the top of the upper cam (green)	47
8.1	Illustration of the Node Combination	51
8.2	Illustration of the shorter interface identified by Workbench (yellow) and the actual interface (red)	52
8.3	Illustration of the conduction paths in preload structure	52
8.4	Illustration of the contact area due to load P	53
9.1	Illustration of the solar radiation that hits the DST at two places along the orbit (mid-day and near eclipse)	57
9.2	The SMSS as seen from the direction of light, with furthest and closest hinges numbered	58
9.3	First result of the temperature of node D85 (part of the middle strip)	60
9.4	Average temperature progression of the three strips in the entry phase	61
9.5	Maximum and minimum temperature progression for the lower and upper cams in the entry phase, including the average temperature as a dashed line, to allow an easy comparison to the strip temperatures.	61
9.6	Average temperature progression of the three strips in the Exit phase	63
9.7	Maximum and minimum temperature progression for the lower and upper cams in the exit phase, including the average temperature as a dashed line, to allow an easy comparison to the strip temperatures.	63
10.1	Illustration of the mechanical model	68
10.2	Three loads: preload, thermal load and resultant force	71
10.3	Illustration of the displacements and rotations of the upper cam	72
10.4	Displacement of the CORE hinge top along the optical axis (z)	72
10.5	Displacement of the upper cam of the CORE hinge along the z-axis	73
10.6	Rotations of the upper cam with respect to the lower cam	74
10.7	Displacement of the upper cam of the CORE hinge along the z-axis	74
A.1	Temperature progression of all nodes of the middle strip for the entry phase	85
A.2	Temperature progression of all nodes of the left strip for the entry phase	85
A.3	Temperature progression of all nodes of the right strip for the entry phase	86
A.4	Minimum and maximum temperatures of the main upper cam components for the entry phase	86
A.5	Temperature progression of all nodes of the middle strip for the exit phase	87
A.6	Temperature progression of all nodes of the left strip for the exit phase	87
A.7	Temperature progression of all nodes of the right strip for the exit phase	87
A.8	Minimum and maximum temperatures of the main upper cam components for the exit phase	88

List of Tables

5.1	Requirements of M2	26
8.1	Node transformation for the middle strip geometries. As geometry Strip_mid is divided into four parts, it consists of four nodes	51
8.2	Minimum, average and maximum difference in temperature between the two models at time $t = 567$. The differences are calculated with respect to the temperature difference between the hottest and coldest nodes (= 100 K). Thus, one percent is equivalent to 1 K	54
8.3	Minimum, average and maximum difference in temperature between the two models at time $t = 5674$. The differences are calculated with respect to the temperature difference between the hottest and coldest nodes (= 101.8 K). Thus, one percent is equivalent to 1.02 K	55
9.1	Initial conditions for the entry phase	59
9.2	Initial conditions for the exit phase	59
9.3	Boundary Conditions for the entry phase	59
9.4	Boundary Conditions for the exit phase	59

List of Abbreviations

Abbreviation	Description
ACS	Aberration Correction System
BYU	Brigham Young University
CFRP	Carbon Fibre Reinforced Plastic
CORE	Compliant Rolling-Element
DOF	Degree of Freedom
DST	Deployable Space Telescope
ECSS	European Cooperation for Space Standardisation
EO	Earth Observation
GMM	Geometric Mathematical Model
GUI	Graphical User Interface
IR	Infrared
JWST	James Webb Space Telescope
M1	Primary Mirror
M2	Secondary Mirror
MCRT	Monte-Carlo Ray Tracing
MLI	Multi-Layer Insulation
NGST	New Generation Space Telescope
PMSS	Primary Mirror Support Structure
SiC	Silicium Carbide
SiOX	Silicium Oxide
SMSS	Secondary Mirror Support Structure
TDI	Time Delay and Integration
TMA	Three Mirror Anastigmat
TMD	Thermal Model Data
TMM	Thermal Mathematical Model
VDA	Vapour Deposited Aluminium

List of symbols

Symbol	Description	Unit
A	Surface area	$[m^2]$
A_i	Nodal surface area	$[m^2]$
b	Contact area half width	$[m]$
B_{ij}	Gebhart factor between nodes i and j	$[-]$
c	Damping coefficient	$[kg/s]$
C_i	Thermal Capacitance of node i	$[J/K]$
c_p	Specific heat capacity	$[J/kgK]$
E^*	Contact modulus	$[Pa]$
E_i	Youngs modulus	$[Pa]$
F	Internal thermal load	$[N]$
F_a	Applied disturbance force	$[N]$
$F_{friction}$	Friction force	$[N]$
F_{ij}	View factor from node i to j	$[-]$
h_c	convective heat transfer coefficient	$[W/m^2K]$
i	Inclination of the orbit	$[^\circ]$
k_i	Thermal conductivity of node i	$[W/mK]$
k	Spring constant	$[N/m]$
K_{ij}	linear conductance constant from node i to j	$[W/K]$
L	Distance between node centers	$[m]$
L_i	Length of node i	$[m]$
L_s	Length of a strip	$[m]$
L_{strip}	Length of a strip	$[m]$
m	Mass	$[m]$
N	Normal force	$[N]$
P	Pretension force	$[N]$
P_{com}	Compressive parameter	$[N]$
P_{ten}	Tensile parameter	$[N]$
Q_i	Heat input to node i	$[W]$
R	Reduced radius of curvature	$[m]$
R_{ij}	radiative exchange constant from i to j	$[m^2]$
R_i	Radius of cylinder i	$[m]$

Symbol	Description	Unit
s	Distance between nodes	[m]
T	Orbital period	[s]
t	Time	[s]
T_i	Temperature of node i	[K]
U_{com}	Peak strain energy during tension	[Nm]
U_{hys}	Energy loss during on hysteresis loop	[Nm]
U_{ten}	Peak strain energy during tension	[Nm]
x	Displacement	[m]
z_{mid}	Displacement of the middle strip in z-direction	[m]
$z_{sideavg}$	Average displacement of the side strips in z-direction	[m]
α	Thermal diffusivity	[m^2/s]
α_{th}	Coefficient of thermal expansion	[m/mK]
α_i	Absorbivity of node i	[–]
δ	Displacement	[m]
δ_{com}	Maximum compressive displacement	[m]
δ_{ten}	Maximum tensile displacement	[m]
ϵ	Strain	[–]
ϵ^T	Thermal strain	[–]
ϵ_i	Emissivity of surface of node i	[–]
η	Normalised hysteresis	[m]
θ	Angle	[°]
μ	Friction coefficient	[–]
μ_k	Kinetic coefficient of friction	[–]
ν	Poisson's ratio	[–]
ρ	Mass density	[kg/m^3]
σ_n	Normal stress	[Pa]
τ	Shear stress	[Pa]
ω	Argument of periapsis	[°]
Ω	Right ascension	[°]

1

Introduction

In the Earth Observation market, having a high ground resolution is critical. In order to achieve these high resolutions, large apertures are needed. To have a system which combines a large aperture with small mass and small launch volume, a space telescope was proposed that uses foldable optical elements to minimise the launch volume and total mass of the system. These foldable elements can be deployed after launch, to achieve the large aperture that is required. This project, called the Deployable Space Telescope (DST), started with a preliminary optical and mechanical design of the telescope in 2014. Over the course of the project, both Master students and PhD. candidates have been continuing the design and analysis of the telescope.

Currently, the conceptual design of the optical and structural elements of the DST has almost been completed. However, the influence of the thermal environment of the DST on the behaviour of the structural and optical elements of the DST is yet to be determined. One of the structural elements of the DST is called a CORE hinge, which is a novel concept that has not been used on telescopes before. There is a need for an analytical characterisation of the thermal behaviour of the CORE hinge and its influence on the mechanical behaviour, in order to know how this type of hinge behaves under the thermal loads that are caused by the thermal environment of the DST and its orbit. To satisfy this need, a thesis project has been carried out, during which a thermal and a mechanical analysis of the DST CORE hinge are conducted.

The purpose of this report is to present the analysis process of the thermal and mechanical analyses, together with the results of these analyses. Furthermore, the implications of these results for the compliance of the CORE hinge with the stability requirements of the DST are presented.

This report is structured as follows. In chapter 2, an overview is given of the current status of the Deployable Space Telescope project. Subsequently, in chapter 3, an explanation is given of micro-dynamics and their influence on the design of high-precision deployable structures, like the DST. A more thorough explanation of the CORE hinge design and development history is given in chapter 4 and in chapter 5, an overview is given of the methodology of the thermal and mechanical analyses. The methodology of the thermal analysis is defined in chapter 6, after which the geometric model of the CORE hinge is described in chapter 7. In chapter 8, an overview is given of the building process of the thermal model. In the following chapter 9, the thermal analysis and its results are highlighted. Finally, in chapter 10, the mechanical analysis and its results are presented, including a description of the mechanical model.

2

Deployable Space Telescope Project Overview

Since the launch of the first satellite in 1957, many more satellites have been launched. One of the satellite market segments is Earth Observation (EO), which has numerous applications, ranging from gathering intelligence to gaining insight in global warming and so on [16]. For most applications, the main requirement of these satellites is the ground resolution of the images that they can produce, as the higher the resolution, the more accurate the images are. In order to obtain the required resolutions, the optical systems of these satellites are generally large, as such high resolutions require very large apertures. This leads to a high spacecraft mass and launch volume.

However, with the size of satellites generally decreasing and considering the rapid rise of microsatellite launches, the high mass and big volume of such systems gets more of a problem. If the launch volume and spacecraft mass could be decreased, these satellites could be launched on smaller rockets. Alternatively, more satellites could be launched with one single rocket. Both result in a decrease of the launch cost.

One of the solutions to this problem is to use deployable optics on a satellite, which can be folded on ground and deployed while in orbit. This would decrease the dimensions of the satellite during launch, while maintaining the large apertures needed for high resolution imagery. The Deployable Space Telescope (DST) is such a deployable system, using four mirror segments to create a very large synthetic aperture. The goal of this chapter is to give an overview of the design activities that have already been performed for the project, and to formulate the research goal and questions that will be answered in the upcoming thesis.

In section 2.1, a short overview is given of the work that has already been carried out. Additionally, a scheme is presented in which all the previous work is summarised. The next two sections delve deeper into the work that has been performed, divided into the optical design and the mechanical design in sections 2.2 and 2.3, respectively. Then, in section 2.4, an overview is given of the analysis activities that have been carried out regarding the CORE hinge. Finally, in section 2.5, an insight is given in the future work that has to or can be performed, which flows directly into the definition of the Thesis proposal.

2.1. Overview of Previous Work

Several master's and PhD. students have been working on the Deployable Space Telescope project since its start in 2014. A quick overview of the project structure is given in figure 2.1, which includes the previous and current students that have worked on the structure and in what order. Dr. Ir. J.M. Kuiper is in charge of supervision and management of the project and since September 2019, Ir. J. Bouwmeester supervises the students working on the thermo-mechanical design of the project. There have been several iterations of the DST team, each with a different number of members and the final one being the current team. These are the following:

- D. Dolkens - 2014/2015
- B.T. van Putten & J.W. Lopes Barreiro - 2016/2017

- G.P. van Marrewijk, M. Corvers & A. Krikken - 2017/2018
- S.M. Pepper, M. Voorn & D. Risselada - 2018/2019
- T.T.D van Wees, E.A. Korhonen, S. Leegwater & J.W. Arink - 2018/2019
- I. Akkerhuis, T.R. Gritter, V. Nagý & F. Hu - 2019/2020

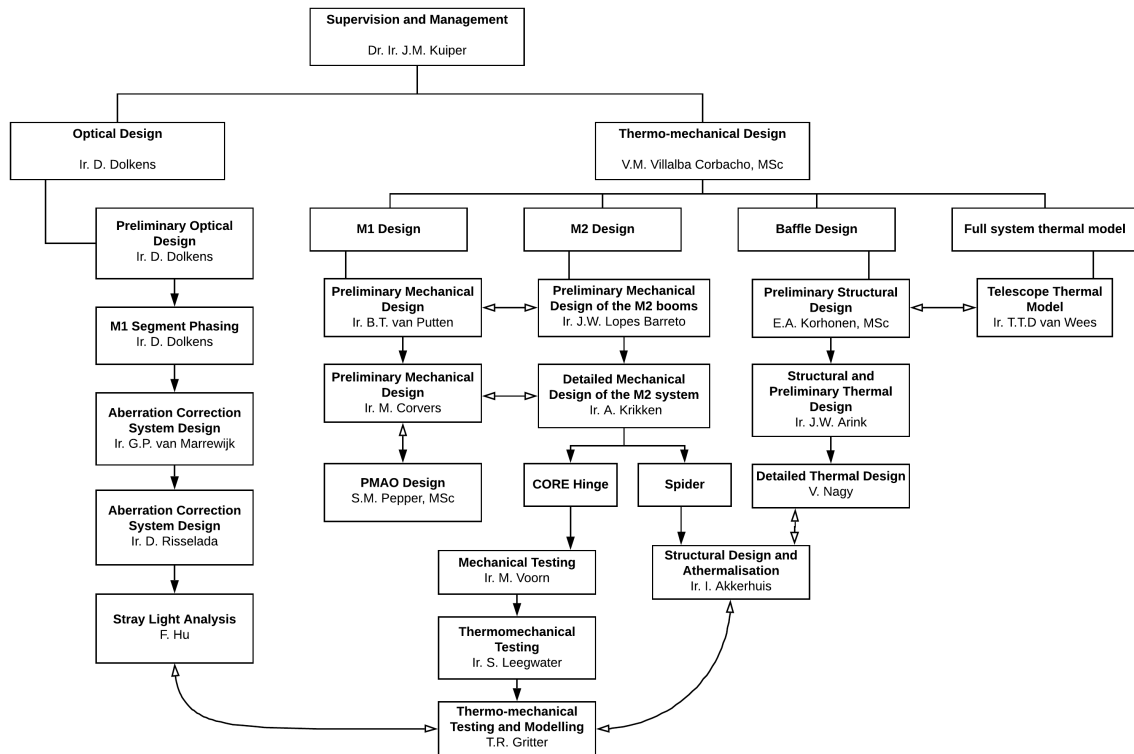


Figure 2.1: The DST team members and what they have worked on. Black arrows indicate work flow, white arrows indicate that members have worked on the project at the same time

2.2. Optical Design

The baseline for the design of an optical system is the optical design. In this section, a short description is given of the optical design of the Deployable Space Telescope. In subsection 2.2.1, the optical layout of the DST is described, along with the process of designing this layout. In subsection 2.2.2, a short overview of the Aberration Correction System is given.

2.2.1. Optical Layout

The first step in the design of a space telescope is the selection of the optical concept and the optical layout. During this step, a trade-off was performed between two synthetic aperture systems; the Michelson Synthetic Aperture and the Fizeau Synthetic Aperture. The first is basically an array of several satellites, which together simulate one big telescope. The second is a telescope of which the primary mirror is divided into multiple segments, which can be easily folded. After the selection of these concepts, a trade-off was performed and it was decided to base the design of the DST on a Full-Field Korsch Three Mirror Anastigmat and optimise it for a low stowed volume and diffraction limited operation for its full field of view. The material of the primary mirror was chosen to be Silicon Carbide (SiC) and the mirrors were given modest radii of curvature [8].

Of the other variants of the Three Mirror Anastigmat (TMA), only the Annular Korsch TMA was deemed viable, but was not selected due to its larger volume, larger distance between the primary mirror (M1) and

secondary mirror (M2), and larger distortions. However, due to the Full-Field Korsch TMA being sensitive to misalignments of M1 and M2, it was later decided to change the design to an Annular Korsch TMA with four mirror segments instead of three. In figure 2.2, the full optical lay-out of the DST is displayed [8][9].

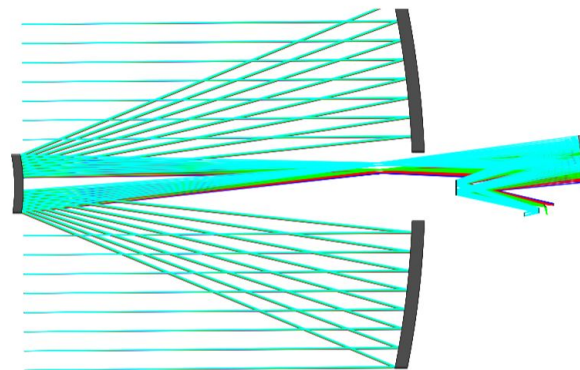


Figure 2.2: Optical lay-out of the DST [9]

The position of the optical detectors of the DST is displayed in figure 2.3. The right part of the figure is zoomed-in from the lower right of figure 2.2. A short overview of the detectors will be given here. Two panchromatic line scan detectors with Time Delay and Integration (TDI) capabilities are placed close to each other. One of these is the primary high-resolution channel, while the second is slightly defocused to be able to retrieve the phase diversity of the point spread function. Next to the two line scan detectors, an array detector is present, which can be used for calibration purposes. The final detectors are multispectral line scan detectors, which are positioned in the outermost part of the focal plane. The pixel size of these detectors is bigger, to compensate for their narrower spectral band [9].

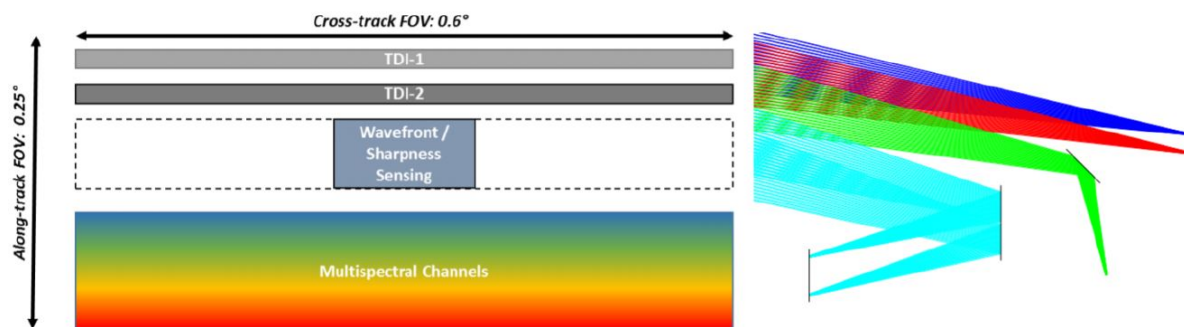


Figure 2.3: Focal plane of the DST [9]

2.2.2. Aberration Correction System

A calibration mechanism is needed in the DST, which should counteract optical aberrations that occur in the system during operation and after deployment. During the preliminary optical design, a calibration strategy of the DST was designed [8]. This design was later translated into an aberration correction system (ACS), using a Deformable Mirror and phase diversity, respectively [35][31].

2.3. Mechanical Design

A stable mechanical design is required to have a stable optical design, which is able to meet the optical requirements imposed on the DST. In this section, the mechanical design of the DST, and the M2 deployment structure in particular, are summarised.

In subsection 2.3.1, a short description of the Primary Mirror Support Structure (PMSS) is given. Subsequently, the Secondary Mirror Support Structure (SMSS) is outlined in subsection 2.3.2. Finally, in subsection

2.3.3, a short overview is given of the design of the baffle that protects the telescope from thermal radiation from the sun.

2.3.1. Primary Mirror Support Structure

The first iteration of the PMSS design was carried out at the end of the preliminary optical design [8], after which the design was further worked out in the preliminary mechanical design phase [36][7]. In this subsection, a short description is given of the current design of the PMSS.

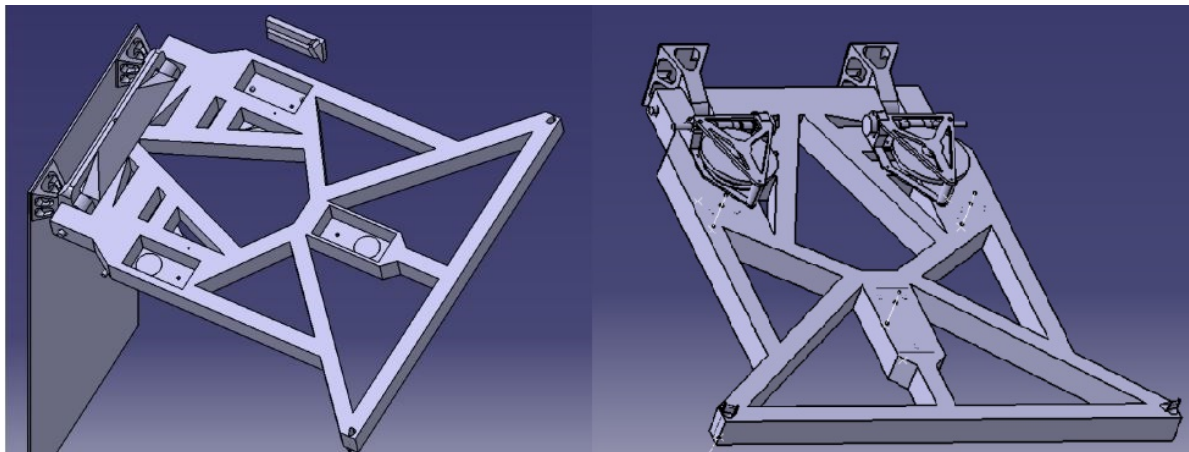


Figure 2.4: Top and bottom view respectively of the T-frame that supports M1 [38][18]

Like its name says, the PMSS supports the primary mirror and handles the deployment of the four mirror segments. The base of this structure is a T-frame which is optimised for weight, like can be seen in figure 2.4. During launch, the T-frame is folded against the spacecraft bus. After launch, the PMSS will be deployed using a boom with three cut-outs, that form tape-spring hinges, and a kinematic interface. A schematic view of this system is provided in figure 2.5. Initially, the actuation of the deployment would be done using the two winches that can be seen on the bottom of the T-frame. These winches are connected to the Secondary Mirror Support System via four tethers, which are guided through the end points of the T-frame. Deployment would be achieved by pulling in the tethers [7]. However, the feasibility of the tethers is currently under investigation, so it is probable that they will not be included in the final design. This is, however, out of scope for this literature study.

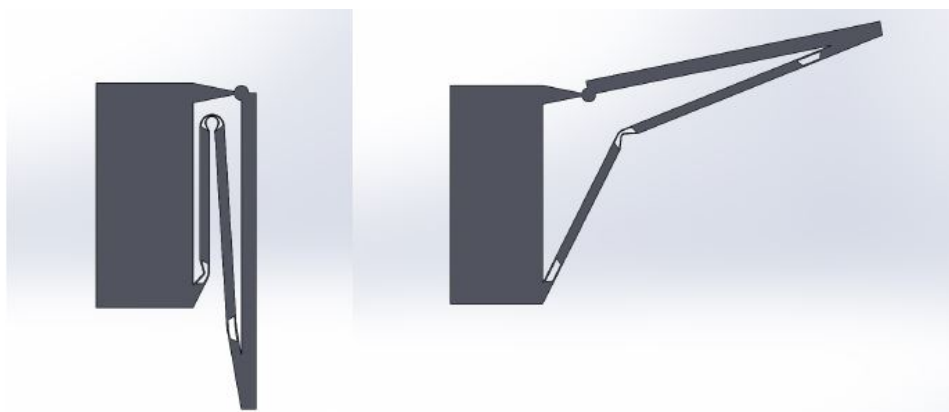


Figure 2.5: Schematic of the pre and after deployment positions of the M1 deployment system [7]

2.3.2. Secondary Mirror Support Structure

Just like the PMSS, the first iteration of the SMSS design was carried out at the end of the preliminary optical design [8]. The SMSS design was continued during the preliminary and detailed mechanical design phases

of the M2 mechanism [25][18]. The latest developments for the SMSS are concerned with the CORE hinge, which has gone through mechanical and thermal testing [39][23]. In this section, the current design of the SMSS is highlighted. This is done in more detail than for the PMSS, as the SMSS is more relevant to the focus of this literature study. This subsection is divided into four parts, the first being a general explanation of the SMSS and the other three each treating their own component. These are the booms, the CORE hinges and the spider.

General overview

The SMSS consists of four booms. Each of these booms is connected to the spacecraft bus and the spider with CORE hinges. The spider is a structure on top of the satellite, to which the secondary mirror is attached. This is done via a kinematically constrained mount. The stability of the spider are ensured by the booms and CORE hinges. The tethers, which are described in subsection 2.3.1, would provide extra support, but, as stated before, their use is currently under investigation.

Booms

Four booms deliver the spacing between M1 and M2 required for the optics, as well as stability for the spider. The booms are made out of carbon fibre and contain one hinge each, such that they can be folded during launch. These hinges are referred to as slotted hinges, and they are formed by cutting two slots in the skin of the boom. This creates a hinge that is similar to a tape-spring hinge. During launch, the hinge is folded over 180 degrees, such that the two sides of the boom touch each-other. During deployment, the boom will stretch, thus deploying the secondary mirror[18]. The pre- and post-deployment positions of the hinge can be seen in figure 2.6.

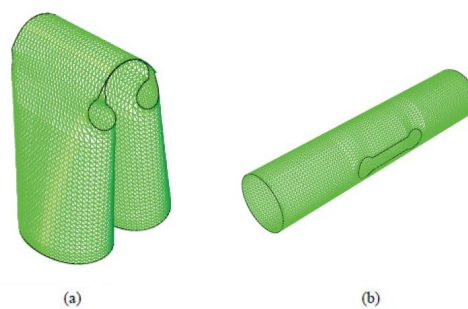


Figure 2.6: Illustration of (a) the position before deployment and (b) the position after deployment [27]

CORE Hinges

The CORE hinge concept has been selected for the top and bottom hinges for the secondary mirror deployment mechanism during the detailed design phase of the SMSS. Furthermore, the specific design of the CORE hinges of the DST has been made during this phase. This hinge comes in two different designs, referred to as the top hinge and the root hinge, which refers to their position along the booms. The difference between the top and bottom hinges is the angle of rotation that they have to allow for, resulting in a lower weight and complexity for the top hinge. The CORE hinge concept has been synthesised by two Master's thesis students of Brigham Young University in the United States. The design is based on several articles published from 1969 to 2001 and will be explained in more detail in chapter 4 [18].

The final iterations on the design of the CORE hinge have been applied during the mechanical testing phase. The changes were applied to increase protection during launch and to prevent shearing between the components [39].

Spider

The spider is a structure that is placed on top of the booms and is responsible for keeping the secondary mirror in place. The design of the spider itself is quite simple and optimised for minimum weight. It's design can be seen in figure 2.8. The tapered beams create a connection point for the secondary mirror, centred between the four booms, and the other beam segments provide bending and torsional stiffness to the spider.

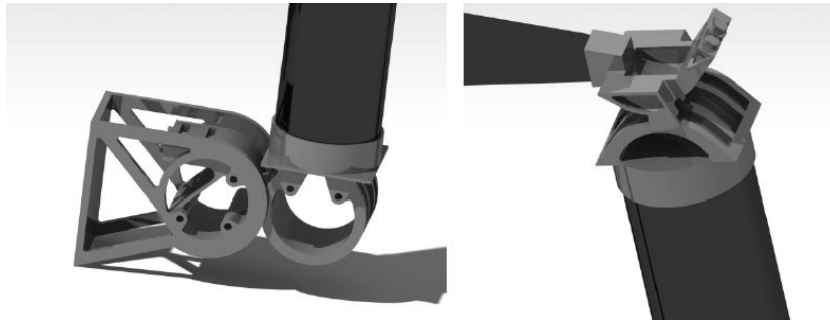


Figure 2.7: The bottom and top CORE hinges, respectively [38]

The secondary mirror is connected to the spider via a mirror interface, called a hexapod. As the name implies, the hexapod is a system consisting of six legs that can be rotated in three directions, with the purpose of athermalising the SMSS. Athermalisation means that thermal expansion of some parts of a structure can be accounted for in other parts, in the case of the DST to keep the distance between the primary and secondary mirror equal. Each of the legs of the hexapod has to constrain one DOF each, which leads to six legs in total, taking redundancy into account [18].

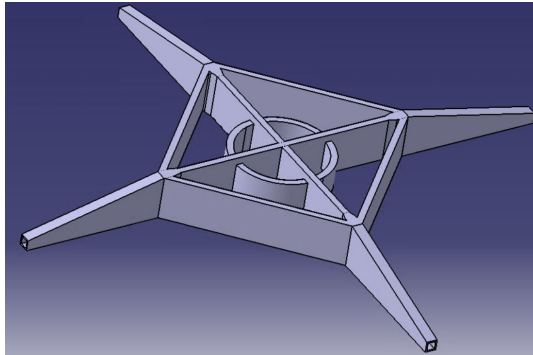


Figure 2.8: View of the spider

2.3.3. Baffle Design

During the preliminary mechanical design phase, it was noticed that in order to provide the telescope with a manageable thermal environment, a baffle is needed to block the sunlight irradiating it [36]. A first iteration of the design of this baffle was performed in two separate theses [17][37], after which the current design of the baffle resulted from the structural and preliminary thermal design of the baffle [2]. In this subsection, a short description of the current baffle design is given.

The baffle mainly consists of a support structure and several layers of Multi-layer insulation (MLI) between them, creating an octagonal shape. The MLI consists of 5 layers of aluminised Kapton, of which the outside is coated with layers of Kapton, VDA and SiOx, respectively, and the inside is covered in a black coating. The reason for 5 layers of MLI is the packing volume of the baffle before deployment. However, five layers is not enough to stay within the temperature budget. Therefore, active thermal control with heaters is incorporated in the baffle. In figure 2.9, a schematic view of the baffle is shown. In this figure, it can be seen that the baffle includes a truncated cone on the top, which proved an effective method to decrease thermal gradients within the telescope.

The structure of the baffle consists of hollow square telescopic CFRP booms and deploys in two degrees of freedom, being the height and the radius. The joints between the radial and lateral parts are prismatic joints and the deployment is actuated by 8 NANO STEM booms from Northrop Grumman [33][2].

It has to be noted, however, that a full redesign of the baffle structure is currently underway, so the design of the baffle will probably change. It was decided to keep these changes outside the scope of this thesis.

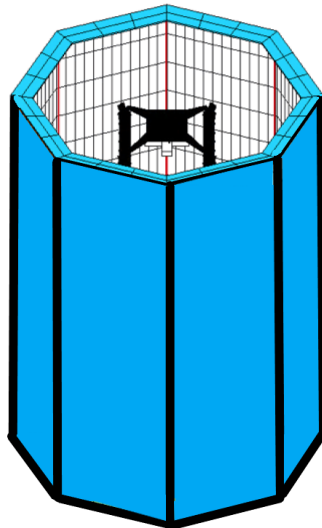


Figure 2.9: Schematic view of the baffle including the SMSS (based on the figure from Arink, 2019)

2.4. Analysis of the CORE Hinge

After the conceptual mechanical design of the SMSS was finished, it was decided to dive deeper into the behaviour of the CORE hinges regarding mechanical and thermal behaviour. To this end, mechanical and thermal tests were conducted. Before these tests could be conducted, two prototypes of the bottom CORE hinge were made for a first stage of testing. Furthermore, the testing procedure was determined. For the tests, a tensile test setup was used, where the CORE prototype was placed in a Zwick-20 kN tensile test bench. Then, several load cycles were applied to the specimen, with increasing maximum load, and the displacements of the CORE prototype were measured. From this, the mechanical behaviour of the prototype could be deduced [39]. Additionally, mechanical tests were performed in which the CORE hinge was subjected to both cyclic loading and temperature differences. Finally, the effect of applying a preload to the CORE hinge was investigated. Applying a preload proved beneficial for the amount of micro-dynamics present in the hinge, but there is a point at which increasing the preload does not result in a decrease in micro-dynamic behaviour [23]. Micro-dynamics are structural phenomena that lead to disturbances on the micro scale. In the SMSS and the CORE hinge in particular, it is important to take micro-dynamic behaviour into account, because of the high precision requirements that are typical for deployable optics [19]. Micro-dynamics are treated more explicitly in chapter 3.

In his thesis report, M. Voorn indicated that five different loads are expected during launch, deployment and operation of the DST, which are the following:

1. Launch loads
2. Deployment torques
3. Loads due to thermal effects
4. Launch and internal vibrations
5. Loads due to manufacturing inaccuracies

However, it was also indicated that during the mechanical tests, a reasonable understanding of the magnitudes of these loads was still missing. Therefore, it was decided to not let the mechanical tests simulate real-life loads, but to use them to test the hinge's behaviour to general load cycles. Thus, even though the tests proved that the CORE hinge could be a suitable hinge for the SMSS, mainly due to its low micro-dynamic behaviour under general loads, this can not be said with reasonable certainty [39].

After the mechanical tests were completed, a thermal analysis of the CORE hinge commenced to find out how the thermal environment influences the behaviour and stability of the CORE hinge. To do this, a thermal model was made of the CORE hinge, which can be seen in figure 2.11. Afterwards, a thermal test was

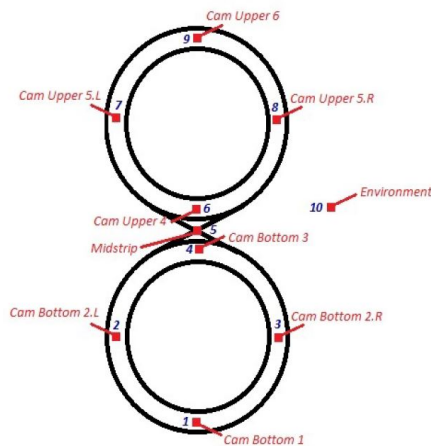


Figure 2.10: Schematic showing the locations and names of the thermocouples [23]

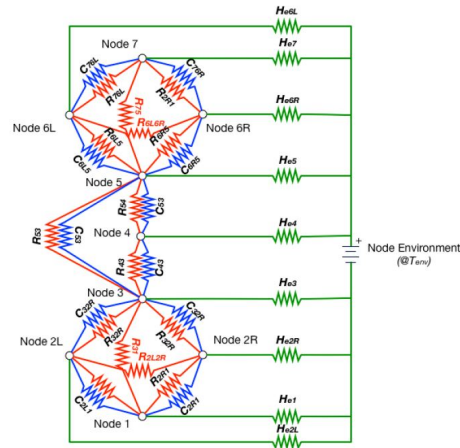


Figure 2.11: Thermal model of Leegwater [23]

conducted in a thermal oven, where the temperature of several points of the CORE hinge was determined using 10 thermocouples. The locations of the thermocouples can be seen in figure 2.10. The goal of these thermal tests were twofold. First, the transient temperature response of the different parts of the CORE hinge was determined and compared to the results of the model. Second, the test results were used to calculate the thermal couplings in the thermal model, such that the results of the model mimic the test results. This was done by means of an optimisation program. [23]

2.5. Future work

Quite some work has already been performed on the Deployable Space Telescope, as can be read in the current chapter. In this section, a description is given of future work to be performed on the DST. Furthermore, at the end of this section, a clear thesis need and goal will be formulated. In subsection 2.5.1, a general overview is given of three possibilities for future work on the DST. One of these is selected. In subsection 2.5.2, the selected possibility is highlighted, after which the thesis need and thesis objective statements are defined in subsection 2.5.3.

2.5.1. General overview

At the end of every thesis, recommendations are made for future work. Furthermore, the DST staff has a good overview of the work that still needs to be performed on the project. Both of these sources were used to gain an overview of the necessary work to be performed for the project. This lead to an indication of three subjects for future work, which are shortly summarised hereafter.

1. **Baffle redesign** Redesign the baffle, while focussing on an optimisation for balancing thermal properties.
2. **Overall stability of the Secondary Mirror Support Structure** Alter the design of the SMSS such that all thermal-related translations can be compensated, in order for the stability of the secondary mirror to stay within budget.
3. **Thermo-mechanical characterisation of the CORE hinge** Continue with the characterisation of mechanical behaviour in the CORE hinge and the thermal analysis of the CORE hinge, possibly including thermal testing.

One of these subjects was to be selected; it was decided to treat the thermo-mechanical characterisation of the CORE hinge in this thesis, with a focus on micro-dynamics. In the remainder of this section, the work that needs to be performed for this subject is described.

2.5.2. Characterising CORE hinges

A reasonable amount of time has been spent in the past on characterising the CORE hinge of the DST. However, there is still some work to be done on the subject. This work will be highlighted in this subsection. It is divided into two parts; the first part is an analytical characterisation of macro and micro-dynamics in CORE hinges and the second part is a thermal analysis of the CORE hinge.

Analytical Characterisation

As explained by M. Voorn in his thesis report, micro-dynamic behaviour can be characterised analytically and experimentally. Supported by multiple reference articles, it was decided to only perform the latter, as an accurate analytical characterisation of micro-dynamic behaviour can be very difficult for reasonably complex applications. This is due to the fact that analytical models of micro-dynamics mainly use empirical relations of which it generally is not known for which situation these are valid [39].

However, it would be beneficial for the DST project if a simple analytical model of the CORE hinge could be made to characterise its macro and micro-dynamic behaviour. This model could be validated by comparing its results to the results of the mechanical tests that have been performed.

As described in section 2.4, it was not yet possible to perform mechanical tests under real-life loading cases. However, if the results of the proposed analytical model can be validated, the model could be used to characterise micro-dynamic behaviour under real-life loads, without performing the actual experiments again. Thus, such a model could answer the question whether the mechanical behaviour of CORE hinges will adhere to the DST stability requirements with higher certainty than the mechanical tests. This would be valuable information for the DST project. Therefore, it was decided to incorporate this activity into the thesis work.

Thermo-mechanical Analysis

As indicated before, a thermal model of the CORE hinge has already been built. Although the optimisation program that was used for solving this model was able to calculate values for the 34 thermal couplings in his model, 18 of these values were not valid.

According to the definition of the thermal couplings, their values are positive if heat is flowing from high to low temperatures and negative if heat is flowing from low to high temperatures. In real-life, heat always flows from high to low temperatures and thus, by definition, the thermal couplings should always be positive. However, many of the calculated thermal couplings are negative, which should not have happened. Furthermore, the sensitivity analysis that was performed indicated that small changes in the input parameters led to totally different results [23]. Both of these problems indicate that something has gone wrong during the optimisation program, or that the used method is incorrect.

Due to these problems, there is still a lot of work to do before a useful and accurate thermo-mechanical analysis of the CORE hinge can be performed. Therefore, it was decided to incorporate a thermo-mechanical analysis of the CORE hinge into the thesis work. This includes identifying the cause of the non-validity of the previous results, creating a new thermal model, and performing the thermo-mechanical analysis itself.

Due to the reasons described above, it is currently not yet possible to determine with reasonable certainty that the CORE hinge will be able to fulfil the stability requirements of the DST under the thermal environment that it will be subjected to. Therefore, the proposed thermo-mechanical analysis will be valuable for the progress of the DST.

2.5.3. Thesis Need and Objective

Now that a clear overview has been given of the tasks that can be performed during this thesis, The thesis need and goal can be formulated. Both are described in this subsection.

Thesis Need Statement

In general, not much is known about the lateral and angular accuracies in the core hinge, and there are still several things that have not been researched in previous work on the CORE hinge. Therefore, there is a need for a characterisation of the influence of the CORE hinge thermal behaviour on the lateral and angular accuracies of the CORE hinge and thus of the deployment mechanism. As the requirements are in the micro scale, micro-dynamics have to be considered in this analysis.

Thesis Need Statement

There is a need for an analytical characterisation of the influence of the thermal environment on the lateral and angular stability of the DST CORE hinges in order to be able to evaluate the compliance of the current CORE hinge design to the mechanical requirements.

Thesis Goal

The thesis need expressed before leads to the following thesis goal.

Thesis Goal

The goal of this research project is **to** characterise the lateral and angular stability of the DST CORE hinges **by** analysing the mechanical behaviour of these hinges under loads induced by the DST thermal environment, and to evaluate whether the overall stability adheres to the stability requirements of the DST.

3

High-Precision Deployable Structures

In the past, deployable structures have been deployed with highly pre-loaded pin-clevis joints (See figure 3.1), which leads to high levels of friction during deployment. Also, geometric uncertainties remain in these deployable structures after deployment, for instance misalignments between the different components of the system, caused by backlash between components. These uncertainties would then actively be alleviated after deployment, while being in orbit. As the misalignments were considerable, strong requirements were put on these active mechanisms [41].

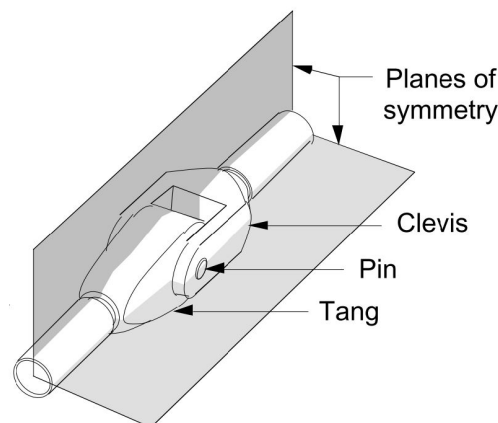


Figure 3.1: A conventional pin-clevis joint with indicated planes of symmetry [20]

During the 90's of the last century, numerous studies on deployable space structure design have been performed at the University of Colorado and NASA Langley Research Center. The main goal of these studies was to gain the required knowledge of deployable structures, to be used during the design of the James Webb Space Telescope (JWST), then called the New Generation Space Telescope (NGST). These studies have led to general guidelines for designing high-precision deployable structures and a profound understanding of the dynamics of deployable structures [21][22]. In a paper from 1998 that resulted from this research, two definitions are given to assess the overall precision of deployable structures:

1. **Deployment precision** This is related to the difference between the actual and predicted final deployment shape of the structure.
2. **Post-deployment stability** This is related to the variations of the deployed shape that are caused by in-orbit thermal and mechanical loads.

From this, it can be deduced that the main focus lies on the stability of the structure after deployment. The stability of the structure during the deployment sequence is not important and is thus not considered.

The developments in deployable space structures that came out of aforementioned research, enable these structures to be deployed with much higher post-deployment accuracies, to the micron level [41]. In this range, structural behaviour phenomena come into play that were only considered to be secondary criteria before. These low-level and dynamic mechanisms are known as micro-dynamics, which are non-linear by nature [19]. Gaining a profound understanding of micro-dynamics is important in deployable structures, as this enables the optical performance requirements to be translated into structural requirements at the component level and therefore, it is also important for the design of the Deployable Space Telescope. [43]

In this chapter, an explanation is given of micro-dynamic responses, and how they can be modelled. It is divided into two sections: section 3.1 is concerned with the overview of micro-dynamic responses and section 3.2 is concerned with the modelling of micro-dynamics.

3.1. Micro-dynamics

As stated before, micro-dynamics are structural phenomena that lead to disturbances on the micro scale. Currently, many aspects of micro-dynamic response are not well understood, and they are difficult to predict [41][19]. However, the mechanisms from which micro-dynamics originate are known to much more detail, enabling characterisation of micro-dynamic behaviour. Micro-dynamics are commonly accepted to be dominated by instabilities in mechanical joints, which primarily arise from frictional load transfer and friction-induced slippage between structural components, causing energy to be lost within the structure. Therefore, it can be reasoned that in order to reduce micro-dynamics, the friction in a mechanism or joint needs to be minimised.

This is illustrated by the fact that micro-dynamics are related to hysteretic behaviour within the deployable structure. Hysteresis is one of the types of micro-dynamic behaviour and is the topic of subsection 3.1.2. Taking the above into account, if a high precision is required from a deployable structure, it is paramount to have a low-hysteresis response to the load cycles that occur in the structure [19]. Next to hysteresis, there are several more non-linear dynamic response phenomena that occur at the micron scale. In this section, a more detailed look is taken at these micro-dynamic responses.

In subsection 3.1.1, an overview is given of three load-displacement non-linearities, after which one of them is explained into more detail in subsection 3.1.2. Finally, an explanation of micro-lurch is given in subsection 3.1.3.

3.1.1. Load-displacement Non-linearities

In White (2001), three non-linear load-displacement responses have been identified, called free play, non-linear elasticity and the aforementioned hysteresis, the latter being the most prominent of the three.

1. **Free play** Free play typically occurs in mechanisms in which clearances are present between components to allow for articulation, and is comparable to backlash. Due to free play, multiple equilibrium points can be achieved by the mechanism, as an infinite number of configurations could be achieved by it.
2. **Non-linear elasticity** Non-linear elasticity occurs as different internal load paths exist in tension and compression, due to a difference in stiffness in tension and compression. Another cause of non-linear elasticity is the fact that under an increasing load, the amount of regions of contact at mechanical interfaces increases. The main consequence of this behaviour is a distortion of dynamic steady state loads.
3. **Hysteresis** Also referred to as hysteretic damping, hysteresis is the dissipation of energy during cyclic loading and unloading of a frictional joint or interface. In the next section, a more detailed explanation of hysteresis will be given.

In Figure 3.2, the effects of free play, hysteresis and non-linear elasticity on the load-displacement curve of a mechanical joint are illustrated, including the total response if these three responses are combined [43].

3.1.2. Hysteresis

Hysteresis is a phenomenon that occurs in many different areas, from magnetism to aerodynamics and also in mechanics. In deployment mechanisms, hysteresis means that the state of a structure is not only dependent on the final load condition, but also on the history of loading and unloading. This works as follows.

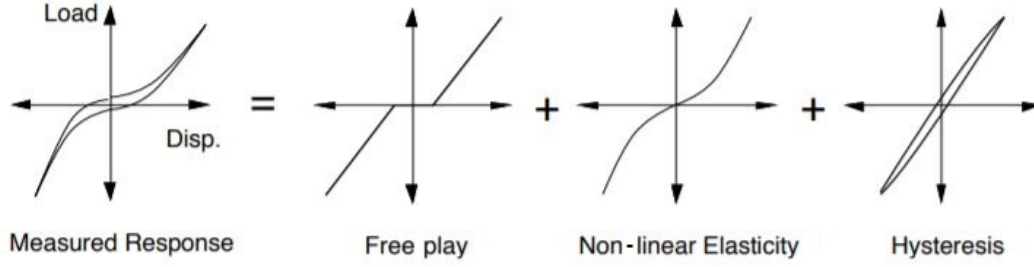


Figure 3.2: Build-up of the non-linear load-displacement response of a mechanical joint [19]

In structures that exhibit hysteretic behaviour, multiple equilibrium states exist. Which of these equilibrium states will be assumed by the structure is dependent on said loading history. This is disadvantageous for the structure, as this leads to dynamic instabilities under a dynamic loading. Furthermore, hysteresis makes it difficult to predict the state of the system, as knowledge about the complete loading history is required. However, by gaining an insight in the mechanisms behind hysteresis, it is possible to evaluate and mitigate the influence of hysteresis on the stability and predictability of a mechanism [19].

Normalised hysteresis

Lake proposes a method to determine the hysteresis in a joint from experimental data, which is based on the concept of energy loss during one hysteresis loop, U_{hys} , which is equal to the area within the hysteresis loop. From this energy loss, the normalised hysteresis can be calculated, as it is defined as the total energy loss of a cycle divided by the maximum elastic strain energy of the cycle.

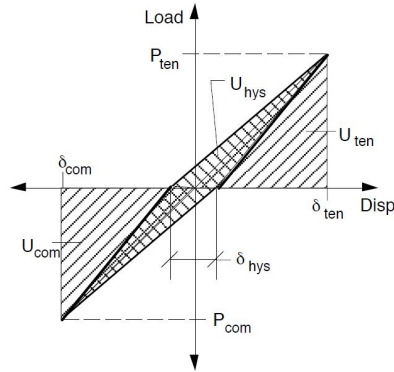


Figure 3.3: Simplified representation of a hysteresis loop [19]

By simplifying the hysteretic response of figure 3.2 to figure 3.3, the area within the loop can easily be calculated using equation 3.1, where P_{ten} and P_{com} are the tensile and compressive parameters and δ_{hys} is the zero load hysteretic displacement. The tensile and compressive peak strain energy can be determined using equations 3.2 and 3.3, respectively. Here, δ_{ten} and δ_{com} are the maximum tensile and compressive displacements. Finally, the normalised hysteresis can be calculated using equation 3.4, which can be simplified to equation 3.5 if the assumption is made that the peak tension and compression loads are equal. In the equations, η_{hys} is the normalised hysteresis [19].

$$U_{hys} = \frac{1}{2}(P_{ten} + P_{com})\delta_{hys} \quad (3.1)$$

$$U_{ten} = \frac{1}{2}P_{ten}\delta_{ten} \quad (3.2)$$

$$U_{com} = \frac{1}{2}P_{com}\delta_{com} \quad (3.3)$$

$$\eta_{hys} = \frac{U_{hys}}{U_{ten} + U_{com}} = \frac{(P_{ten} + P_{com})\delta_{hys}}{P_{ten}\delta_{ten} + P_{com}\delta_{com}} \quad (3.4)$$

$$\eta_{hys} = \frac{\delta_{hys}}{(\delta_{ten} + \delta_{com})/2} \quad (3.5)$$

Hysteresis and load magnitude

Hysteresis can result from several different structural effects, each dominating their own load regime. In figure 3.4, a qualitative representation of the variation of normalised hysteresis with the load magnitude is illustrated. Furthermore, it displays the aforementioned load regimes. As can be seen from the figure, the region with the highest amount of hysteresis is dominated by friction [19]. In the next paragraph, a short explanation of the figure will be given. It has to be noted that the amount of hysteresis is indicated as percent hysteresis, which is another name for a normalised hysteresis.

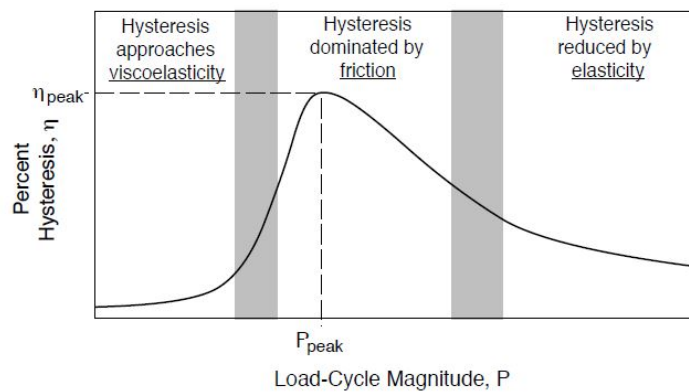


Figure 3.4: Relation between the magnitude of the load on a high precision deployment mechanism and the amount of hysteresis in this mechanism [19]

At low load-cycle magnitudes, there is almost no friction-induced slippage within the structure and the amount of normalised hysteresis approaches visco-elastic hysteresis. Visco-elastic hysteresis is also referred to as material hysteresis, as it is the hysteresis that occurs within the material itself.

If the load magnitude is increased, there is a dramatic increase of normalised hysteresis, reaching hysteresis levels that are much higher than material hysteresis. This can be explained by the fact that at these load levels, friction-induced slippage is rapidly increasing, while the elastic deformations are still small.

Finally, if the load magnitude is increased even further and the amount of static friction is limited, normalised hysteresis decreases substantially. This is due to the fact that at higher loads, elastic deformations are large compared to slippage-induced deformations [19].

Micro-slip

The most dominant cause for hysteresis is considered to be frictional load transfer, which is underlined by figure 3.4 [19]. The main source of this friction induced hysteresis is called micro-slip, which works as follows. By preloading surface interfaces, the surfaces are brought into contact. Due to this, normal stresses occur across the nominal contact area. Even if shear forces are then applied that would be below the macroscopic Coulomb limit, part of the contact area can slip by several microns with respect to the other surface. When this happens, hysteresis occurs [15]. As opposed to micro-slip, friction that is governed by coulomb friction is called gross stick-slip [19].

Implications for Mechanism Design

From the discussion of the different aspects of hysteresis, Lake has drawn several conclusions which may have an impact on the design of deployable mechanisms.

- According to current insights in micro-dynamics, micro-slip does not cause high-frequency instabilities, but rather non-linear variations in the vibrational response of a structure. Therefore, if the disturbance forces on a high-precision deployment mechanism stay within the micro-slip range, the micro-dynamic response of the structure is expected to be small.
- Hysteresis in high-precision deployable structures under low loads is dominated by micro-slip.
- The presence of a peak in the normalised hysteresis response presented in figure 3.4 indicates that a coulomb threshold is present in the hysteretic response. This threshold load occurs around the inflection point in the curve, and can be considered as an operational upper limit for deployable structures. This is illustrated in figure 3.5, which is a similar graph to figure 3.2, but with information on the slip regimes corresponding to the curve.
- Irrespective of the sort of friction (micro-slip or gross stick-slip), the presence of hysteresis indicates that loads on the deployment mechanism are transferred via traction forces that are present within the mechanism. This means that in order to reduce the hysteretic response of a deployable structure, its design has to be modified to reduce frictional load transfer.

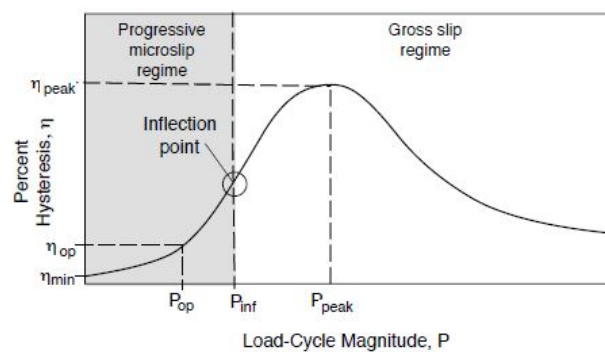


Figure 3.5: Indication of the inflection point on the hysteresis curve [42]

The motivation for the existence of an operational limit is related to the first conclusion. At loads below the inflection point, micro-slip occurs, which leads to considerably lower displacements than under gross stick-slip. Thus, it is beneficial for the structure to stay in this regime.

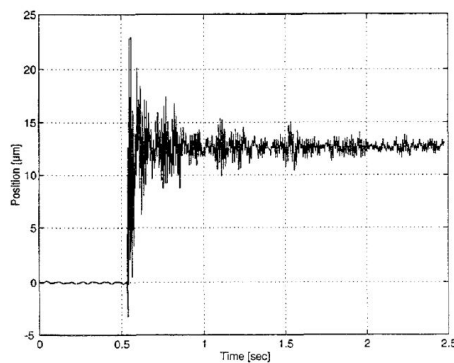


Figure 3.6: Micro-lurch behaviour identified in Minimast micro-dynamics experiments [41]

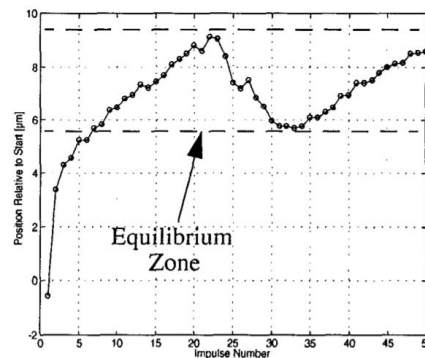


Figure 3.7: Equilibrium zone identified in Minimast micro-dynamics experiments [41]

3.1.3. Micro-lurch

Micro-lurch is an abrupt permanent shape change mechanism that is caused by a transient dynamic loading. The observed motions due to micro-lurch are generally in the same range as micro-slip behaviour [42]. The biggest problem with micro-lurch is that it can accumulate, shifting the post deployment position of the structure to the so-called Equilibrium Zone. This results in a displacement in the range of several microns.

The phenomenon of micro-lurch has been characterised experimentally [41]. The reason for this characterisation was that by understanding the characteristics of micro-lurch, its effects could be anticipated during the design of high-accuracy deployment systems.

3.2. Modelling of Micro-dynamics

There are two ways of characterising micro-dynamic effects. The first way is an experimental characterisation, in which the amount of, for instance, hysteresis in a hinge under different loadings is tested. For the DST CORE hinge, this has already been done [39]. The second way is to make an analytical model that is able to analyse micro-dynamic behaviour in a hinge. In the past 30 years, several attempts have been made to build such models. In this section, two of these models are described, which are both applicable to another micro-dynamic responses mechanism. In subsection 3.2.2, a model of micro-lurch, made by Warren, is presented and in subsection 3.2.1, a model of hysteresis is outlined, which is proposed by Lake.

3.2.1. Hysteresis

As stated before, it is very difficult to make precise predictions of the magnitude of hysteresis in a (deployable) structure. Next to the dependency on the total loading history, deployable structures are generally rather complex. Luckily, it has been demonstrated that substantial knowledge of the mechanical implications of hysteresis can be achieved by using fairly simple models [19]. An example of such a model can be found in figure 3.9, which simulates the normal and shear stresses along a frictional interface.

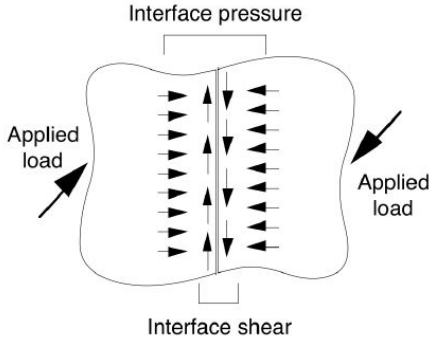


Figure 3.8: Simplified schematic view of frictional load transfer across a mechanical interface [19]

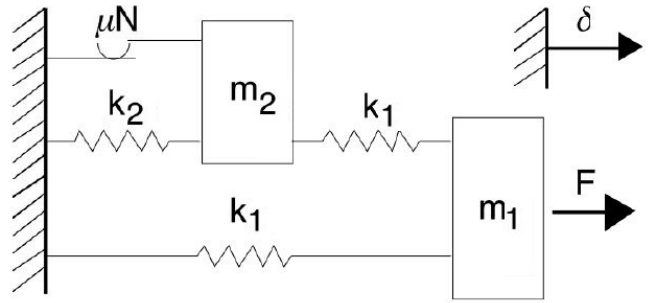


Figure 3.9: Schematic view of the hysteresis model [19]

The schematic in figure 3.8 indicates how forces that are applied close to a mechanical interface can lead to normal pressure and shear stresses along the interface. These effects are simulated by the model in figure 3.9, in which the normal pressure is represented by the elastic load with only the spring and the shear stress is represented by an inelastic load path with two springs and the friction element, μN . As can be seen, this model is quite similar to the model for micro-lurch, the only difference being the absence of the damping of mass 1, c_1 [19]. The equations of motion are therefore the following:

$$m_1 \ddot{x}_1 = -2k_1 x_1 + k_1 x_2 + F_a \quad (3.6)$$

$$m_2 \ddot{x}_2 = -(k_2 + k_1)x_2 + k_1 x_1 - \mu N \text{sgn}(\dot{x}_2) \quad (3.7)$$

The hysteretic response that is displayed in figure 3.4 can also be reproduced with this simple model, which leads to figure 3.10. The simplified model predicts a reasonably similar response as more complex analyses, which can be seen as the normalised hysteresis peak from the original figure is present, as well as its decrease to a limit at loads higher than the peak-hysteresis load.

3.2.2. Micro-lurch

In 1999, an article was published on the sub-micron mechanical stability of a deployable telescope structure [42]. In this article, a description is given of the process and results of micro-dynamics testing that was carried out on a test mechanism. Furthermore, a simple non-linear analytical model is presented. This model

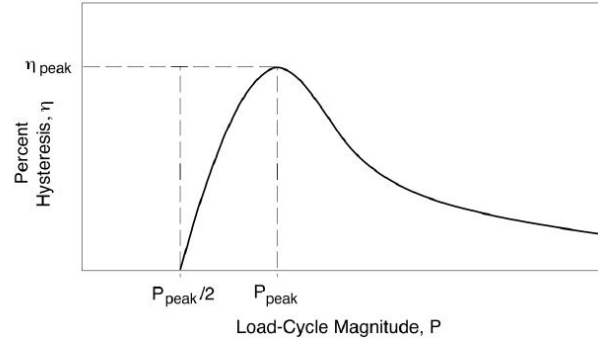


Figure 3.10: Hysteresis behaviour of the simplified model [19]

aims to represent the micro-lurch trajectories and the mechanics of the equilibrium zone resulting from the experiments as good as possible, using known friction mechanics. A schematic view of the model can be seen in figure 3.11.

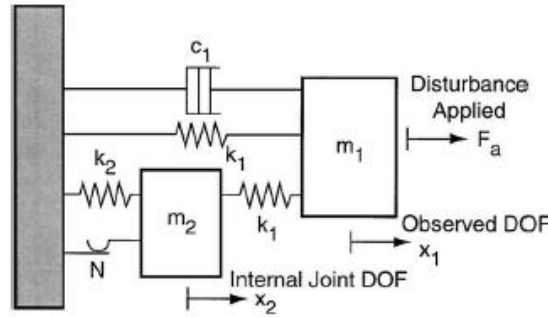


Figure 3.11: Schematic view of Warren's model [42]

From this schematic, it can be seen that the model contains two masses, m_1 and m_2 . Mass 1 is connected to the wall by a spring with linear stiffness k_1 and a damper with viscous damping c_1 , and it has a mass of m_1 . Furthermore, mass 1 is connected to mass 2 with a spring, again with linear stiffness k_1 . Mass 2 is connected to the wall with a spring with linear stiffness k_2 and with a stick-slip Coulomb friction force N . The system can be excited by a force F_a , which is applied at m_1 . In the process of matching the analytical results with the experimental results, it was determined that a simpler single-degree-of-freedom mass-spring system with a parallel friction force was not good enough, as it was unable to capture the convergent micro-lurch behaviour that the experimental data showed. Therefore, this kind of model was discarded. The coupled equations of motion for the model are displayed in equations 3.8 and 3.9.

$$m_1 \ddot{x}_1 = -2k_1 x_1 + k_1 x_2 - c_1 \dot{x}_1 + F_a \quad (3.8)$$

$$m_2 \ddot{x}_2 = -(k_2 + k_1)x_2 + k_1 x_1 - \mu N \text{sgn}(\dot{x}_2) \quad (3.9)$$

In order to transform the equations of motion into the response of the system to an impulse disturbance, the equations of motion have been integrated numerically. From the resulting system response, it can be concluded that the results of the model are similar to the results of the experiments; the model accurately predicts the magnitude of the micro-lurches and the convergence rate of the dynamics.

4

CORE Hinges

A short description of the DST CORE hinges has already been given in chapter 2. In this chapter, a more thorough explanation of this type of hinge in general will be given. In section 4.1, an explanation of the CORE hinge characteristics is given, and in section 4.2, the development of the CORE hinge is treated, from the invention of the Rolamite concept in 1967 to the current DST CORE hinge design.

4.1. Compliant Rolling-Element

The name Compliant Rolling-Element hinge gives a good indication of what such a hinge is. The word compliant is mostly used in the term compliant mechanism and is related to the word (to) comply. In structural engineering, this is a synonym to flexible. The word compliant illustrates that it is a mechanism that uses flexible links to achieve its goal, which can be, for example, to transform a certain input to a specific output. In the thesis of Halverson, a compliant mechanism is defined as 'any mechanism that transfers or transforms motion or energy through the deflection of one or more of its members' [13]. In a CORE hinge, these flexible links connect the two cam halves to each-other. In figure 4.3, the compliant link between the rolling elements can clearly be seen.

The combination rolling-element indicates that the hinge consists of several elements, in this case two, which are rolling over each-other. More specifically, the CORE hinge is designed as such that the two parts roll over each-other in pure rolling under a no-slip condition. This rolling is illustrated in figure 4.1. In order to achieve this, however, a preload generally has to be applied [13].

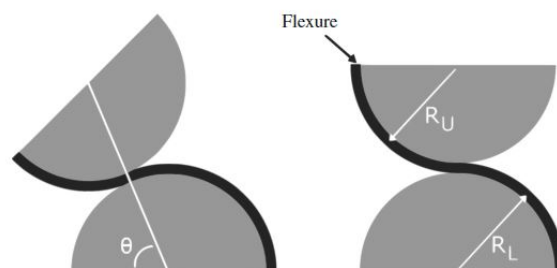


Figure 4.1: Illustration of the rolling motion of a CORE hinge [14]

Comparison to other hinge types

Next to the CORE hinge, there are several other types of hinges which can be used for the same applications, like pin-clevis joints (see figure 3.1 in chapter 3). However, CORE hinges have several advantages over these other hinges, which are stated below. The first three are assured by constraining the radius of the compliant strips, and thus also the stress in the strips, and the fourth assumption is reached by allowing the surfaces to roll over each-other, which creates a contact guided mechanism [14][18].

1. A large range of motion
2. Increased off-axis stiffness
3. Avoidance of stress concentrations
4. Reduced wear and friction and thus low hysteresis and no or reduced need of lubricants

However, CORE hinges also have the following two disadvantages. First, due to the thermal environment, thermal snap can occur, causing damage to the compliant flexures. Secondly, if the cams and strips are made of the same material, cold welding could occur in space, which is the joining of two parts in contact under an impact or wear, in a vacuum [39].

4.2. History of development

Already in 1967, a concept comparable to the CORE hinge was presented by Sandia National Labs and a patent was registered in 1969 [45][4]. The concept is called Rolamite and it consists of two rollers, around which a band is wound. The band is then connected to a plate at both ends, which makes a connection due to which the two plates can be linearly translated with low friction levels [13]. In figure 4.2, a schematic view of the Rolamite concept is shown.

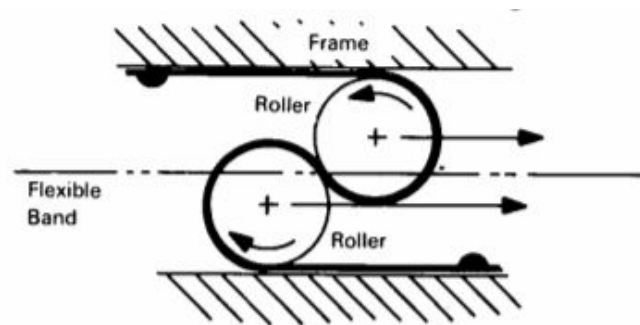


Figure 4.2: Schematic visualisation of the Rolamite concept [44]

It was shown in 1996 that the Rolamite concept could also be used for Cylindrical-Planar and Cylindrical-Cylindrical mechanisms [32]. The second of these applications was picked up for a thesis at Brigham Young University (BYU), in which the band of the Rolamite was replaced by compliant links, the result of which became the CORE hinge [5], which can be seen in figure 4.3.



Figure 4.3: Three phases in the manufacturing of the CORE hinge, with the rightmost depicting the final product [5]

Three years later, another master's student at BYU would build upon the earlier thesis work in his own thesis, to create a tension-stable CORE hinge. This CORE hinge is attained by attaching a cam to the circular CORE surface, which is not fully round, but has two straight surfaces, creating stable and unstable configurations. In figure 4.4, the CORE hinge is displayed in stable and unstable equilibrium, respectively. In order for the CORE to be moved from an unstable to a stable configuration, a tensile force has to be applied [13].

As stated before, the CORE hinge was selected for the DST during the detailed mechanical design of the SMSS, after which the design of the CORE hinge was adapted to be applicable for the project. The decisions that were made were concerned with the dimensions, material and preload application method for the CORE hinge. However, before that was done, a change was made to the concept of the CORE hinge, which is illustrated in

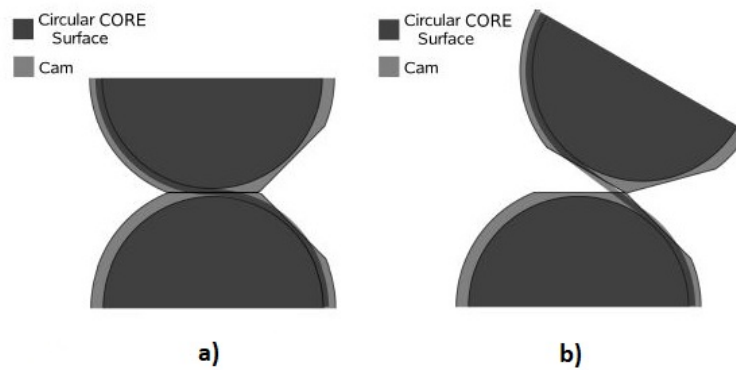


Figure 4.4: Tension stable CORE hinge concept, with a) a stable equilibrium and b) an unstable equilibrium [13]

figure 4.5 [18]. Instead of the two cams being separated by the flexure, like in the CORE hinge design of BYU, the two cams are in contact with each-other, while the strips, that are rolling over smaller diameter part of the cams, hold them together. This alteration was made in order to prevent the cams from separating and impacting again. This is achieved by the presence of an additional vertical force component in the system. Furthermore, a preload is applied to the strips, further decreasing the chance of cam separation. As in this concept, the cam halves are in contact, cold welding might be an issue. Therefore, it was decided to add a Keronite Endure surface treatment [30] to the cam halves.

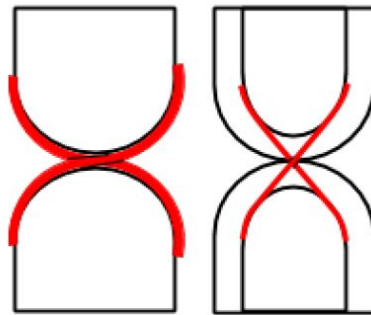


Figure 4.5: Schematic of the two DST CORE hinge concepts [18]

The strips are 0.3 mm thick, and have a total width of 31 mm. The cam halves have a outer radius of 35 mm, and inner radius of 29.6 mm and the total cam contact surface is 20 mm. The hinge has a total width of 54 mm. For the preload device, a bolt and Belleville washers are selected, as this creates a stiff connection which also has an almost constant preload [18]. In figure 4.6, CATIA renders of the top and root CORE hinges are displayed.

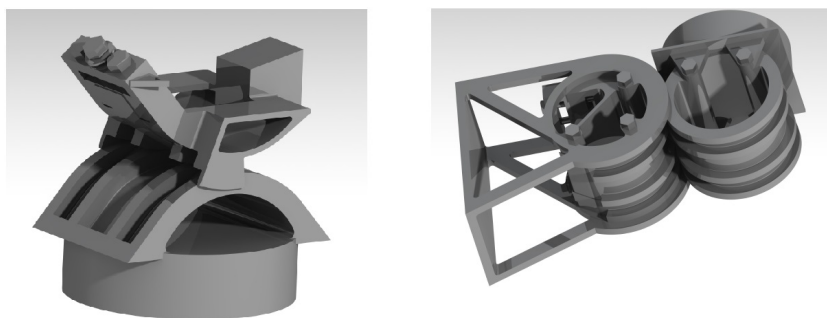


Figure 4.6: Renders of the top and root CORE hinges, respectively [18]

The final iteration of the DST CORE hinge has been made at the start of the mechanical testing phase. During this iteration, shear protection for during launch has been added to the root hinge design, the amount of contact surfaces between the cams has been reduced from four to two and the material of the cams was changed from titanium to aluminium [39].

5

Overview of the Thesis Methodology

As explained in section 2.5, the objective of this thesis is to determine the stability of the CORE hinge under mechanical loads caused by thermal loads. This means that both a thermal and a mechanical analysis have to be performed, where the results of the former have to be translated to inputs for the latter. In this chapter, an overview is given of the steps that have been performed, in order to achieve the objective. In later chapters, the different steps will be treated in more detail. In section 5.1, the general methodology of the thermal analysis will be described. In section 5.2, it will be explained how the thermal results will be translated into inputs for the mechanical model by means of a thermo-mechanical analysis. Afterwards, in section 5.3, the mechanical analysis itself will be highlighted. Finally, in section 5.4, the stability requirements of the DST are described, in order to put the stability results into perspective.

5.1. Thermal Analysis

The thermal analysis is the first analysis that is performed. For this analysis, a thermal model is built of the CORE hinge. The goal of this analysis is to determine the temperature distribution of the CORE hinge along an orbit. This result is influenced by many parameters, most of which influence the results via the solar, albedo and infra-red radiation that the different components of the DST are subjected to. These influencing parameters are: the orbit of the telescope around the Earth, the planetary characteristics, like albedo and infra-red temperature, the attitude and the geometry of the telescope and the location along the orbit. For example, if the DST is in eclipse, the DST will receive less radiation, and thus will be colder on average than in sunlight. Because of the dependence of the thermal behaviour on the incoming thermal radiation, it is logical that the radiation distribution of the DST is an important input for the thermal model. Another important influence on the temperature distribution of the DST is the amount of heat exchange between the different components of the telescope. This leads to a second important input of the thermal model, which are the thermal couplings between the components.

More detailed information on the thermal analysis methodology and the way in which the aforementioned inputs are determined can be found in chapter 6. Furthermore, different methods for the thermal analysis and the selection of one of these methods is treated in that chapter.

5.2. Thermal Results to Mechanical Input

A mechanical model will be used at the end of the thesis to calculate the behaviour of the CORE hinge under certain thermal loads. However, before the mechanical analysis can be started, the results from the thermal analysis have to be translated into mechanical inputs, like forces, stresses or displacements. A thermo-mechanical analysis is used to perform this translation. In such an analysis, the temperature distribution and thermal gradients within a structure are used to determine the displacements and stress distributions inside the structure. The coefficient of thermal expansion is an important characteristic here, as expansion and shrinkage of the components of a structure determine the nature of the stresses and displacements. Several tools and programs have been developed with which thermo-mechanical analyses can be performed. One such program is MSC.NASTRAN. However, there is a problem. The results from a Lumped Parameter

based analysis are incompatible with a finite element based analysis. This issue can be solved with ESA's program SINAS IV. SINAS IV can convert the results of thermal lumped parameter analyses into input data that can be used in thermo-elastic finite element analyses. This works by mapping thermal lumped parameter results onto a finite element mesh built in MSC.NASTRAN using purely geometrical interpolation or conductive finite-element interpolation. [11]

5.3. Mechanical Analysis

The goal of the mechanical analysis is to determine the stability of the CORE hinges and their behaviour under thermal loads. This analysis is performed with a lumped parameter mechanical model, consisting of masses, springs and friction elements. These simple elements represent the components of the CORE hinge and are combined to build a model that is mechanically representative of the CORE hinge. In section 3.2, two examples of such a model have been described, which serve as a basis for the mechanical model of the CORE hinge, especially the model in figure 3.9. As this model describes a frictional interface, multiple of which exist in the CORE hinge, several of these models are linked together to get an accurate representation of the CORE hinge.

On the other hand, a more simple model as in section 3.2, could already give an insight in the mechanical behaviour of the CORE hinge. However, such a model should, as a minimum, be able to determine both the lateral and angular stability of the CORE hinge are subject of this thesis.

The model building process is divided into two phases. First, the simple model described in subsection 3.2.1 is adapted to represent the CORE hinge, in order to get acquainted with such a model and to identify problems that are much harder to solve for a more detailed model. Second, the more detailed mechanical model is built by connecting several interface models to each other.

When the final mechanical model has been built, the mechanical model is converted into a system of ordinary differential equations, which is solved using the ode45 function in Matlab.

In chapters 10.2 and 10, the mechanical model and the mechanical analysis will be described in much more detail, respectively.

5.4. Requirements

Assessing the stability of the CORE hinge only leads to useful information if the stability is compared to the stability requirements that have been defined for the DST. In this section, the stability requirements of the DST that are relevant for the CORE hinge are described.

In the requirements revision document of the DST project, all DST requirements are defined. The requirements that are most interesting for the CORE hinge stability are part of the functionality requirements of the secondary mirror and consist of the following two types. The first type of requirements are the requirements on the stability of the M2 mechanism. These requirements are related to short-term vibrations, with a frequency above 1 Hz. The second type of requirements are requirements on the in-orbit drift of the mechanism. Both of these types consist of six requirements, one lateral and one angular per axis.

The M2 mechanism stability requirements The in-orbit requirements are related to fluctuations in the longer term, with frequencies below 1Hz [10]. These requirements are summarised in table 5.1. The requirements are stated in appendix B.

Table 5.1: Requirements of M2

Requirement	Lateral			Angular		
	X-axis	Y-axis	Z-axis	X-axis	Y-axis	Z-axis
In-orbit drift	4 μm	4 μm	2 μm	6 μrad	6 μrad	12 μrad
M2 mechanism stability	1 μm	1 μm	0.5 μm	1.5 μm	1.5 μm	3 μm

6

Thermal Analysis Method Selection

Several choices have to be made before the thermal analysis can be started with. These choices determine how the thermal analysis is performed and which computer programs are used. In this chapter, these choices are described and an explanation is given of the reasoning behind these choices.

In section 6.1, an overview of the lumped parameter method is given, after which the choice for the Lumped Parameter method is explained. Consequently, the thermal analysis program ESATAN will be described in section 6.2. Finally, in section 6.3, several possible methods of using ESATAN are described, after which the method selection process is explained.

6.1. Lumped Parameter Method

There are several different methods to perform a thermal analysis. For the thermal analysis of the DST CORE hinge, the Lumped Parameter method is a likely candidate. The Lumped Parameter method is a way to discretise an object, mechanism or structure. This leads to a discrete nodal network, all nodes together representing the capacitance of the whole system.

In subsection 6.1.1, an explanation is given of how the lumped parameter method works and in subsection 6.1.2, a description is given of the advantages and disadvantages of the method, based on which a decision will be made whether the method will be used for the thermal analysis of the CORE hinge.

6.1.1. General Information

The following equation is the general Lumped Parameter equation, which incorporates material properties, internal dissipation and the conductive, convective and radiative heat transfer between two nodes i and j into one equation.

$$C_i \frac{dT_i}{dt} = \sum_{j \neq i} K_{ij} (T_j - T_i) + \sum_{j \neq i} R_{ij} \cdot \sigma \cdot (T_j^4 - T_i^4) + Q_i \quad (6.1)$$

In this equation, the subscript tells which node is involved, where node i is the node of interest and node j represents the surrounding nodes, the influence of which is summed up. C is the capacitance of the node, T is the temperature of the node, Q is the heat input to the node. Finally, K_{ij} and R_{ij} are the linear conductance and radiative exchange constant, respectively, from node j to node i . These are calculated as follows: $K_{ij} = h_c A + \frac{k_i A}{L}$ and $R_{ij} = B_{ij} \epsilon_i A$. Here, h_c is the convective heat transfer coefficient of the material, A is the surface area of the node, k_i is the thermal conductivity of node, L is the distance between the node centres, B_{ij} is the Gebhart factor between the nodes, which is the radiation exchange factor between a number of nodes and ϵ_i is the emissivity of the surface. Of the parameters in the equation, C_i , R_{ij} and Q_i are outputs of the geometric model. K_{ij} is an output of the geometric model in the case of fused nodes, but in the case of two nodes in contact, the value has to be defined by the user. The temperatures are not gained from the geometric model, as these are calculated by the thermal model.

The general Lumped Parameter equation is valid for transient calculations. If a steady-state case is solved, the left hand term is equal to zero. In order to solve the Lumped Parameter equation, finite-differencing schemes are used. [26] This will be described in more detail in subsection 6.2.2.

6.1.2. Advantages and Disadvantages

The main advantage of using the lumped parameter method is its simplicity. Whereas a continuous system is represented by differential equations, a lumped parameter model can be represented by a system of algebraic equations which can be solved by regular techniques. Furthermore, it allows this system to be solved by hand or using a computer program. Additionally, lumped parameter models are easy to construct and can be used to model complex geometries. [26]

Unfortunately, lumped parameter models also have some drawbacks. The accuracy of a lumped parameter model is fully dependent on the notion that conductivity between parts is accurately known and interfaces are accurately defined before the analysis. This is not always the case.

The second drawback has to do with the discretisation of the structure. As a structure is discretised, information gets lost. In the lumped parameter model, the resulting temperature for a node is the temperature that would be in the middle of that node. This means that with such a model, one is only able to determine the temperature at the node centres. The temperature distribution between the centres is not known, which means that eventual temperature extremes between the nodes are not noticed.

Although the lumped parameter method has some drawbacks, the advantages of the lumped parameter method make this method an attractive method for the CORE hinge model. This is due to the following. Because of the simplicity of the lumped parameter method, more time can be spent on characterising the conductivity between parts, to make sure that they are accurately represented in the model.

Furthermore, it is expected that, despite the second disadvantage, the relatively small size of the DST CORE hinge allows the thermal model to be accurate enough for the goal of the thesis. The reason for this is the fact that because of the small size of the hinge, not many nodes are needed to achieve small distances between nodes. Thus, not many nodes are needed to get a reasonable accuracy. In order to test whether this is true, a sensitivity analysis is performed during the model validation. This sensitivity analysis is described in section 8.2.

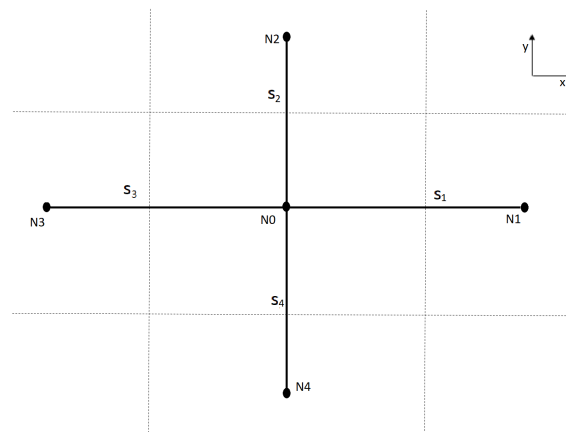


Figure 6.1: Node N0 and the four adjacent nodes

6.2. ESATAN

It is very well possible to write a computer program that uses the lumped parameter method to perform a thermal analysis. However, there are already several computer programs that use the method for thermal analyses, like SINDA/G and ESATAN-TMS. As these programs have already been verified, using them for the thermal analysis of the CORE hinge makes sure that more time can be spent on the actual analysis. In earlier stages of the DST project, several thermal analyses have already been performed, all of them on the complete telescope. These analyses have all been performed in ESATAN, a license of which is available for DST team members. Because of the above, it has been decided to use ESATAN for the thermal analysis to be performed on the DST CORE hinge.

ESATAN-TMS, or simply ESATAN, is a thermal analysis software program designed for the European Space Agency (ESA) and is used for all ESA projects. As the program uses the lumped parameter method, With the models made in ESATAN, both steady-state and transient analyses can be performed. Furthermore, several solution routines are predefined in the ESATAN package, which can be called with simple commands in the TMM or the ESATAN GUI. [12]

In this section, a description of the program is given. In subsection 6.2.1, the general approach of modelling in ESATAN is highlighted, after which the Lumped Parameter Method will be described, which is used to solve the model. Finally, in subsection 6.2.2, it will be explained how ESATAN uses the geometric and thermal models to calculate the temperature of every single node.

6.2.1. Using ESATAN

Models built in ESATAN consists of two separate models, which can be written in code, or built in a dedicated Graphical User Interface (GUI), called ESATAN-TMS Workbench. These are the Geometric Mathematical Model (GMM or geometric model), and the Thermal Mathematical Model (TMM or thermal model). In the geometric model, the geometry of the satellite or part of its components is modelled. This model is used for calculating the solar and planetary fluxes on the spacecraft and the thermal couplings (radiative, convective and conductive) between components. In the thermal model, the satellite parts are reduced to nodes and the thermal couplings of radiation and conduction between these nodes are defined. Furthermore, node properties such as thermal conductance, nodal area, conductivity and many more are defined in this model.

The standard method for performing a thermal analysis in ESATAN is as follows. First, the geometric model is created after which the thermal model is built. In the thermal model, internal dissipation, conductive interfaces, initial conditions and boundary conditions are defined. The two models can either be built and run in the Workbench Graphical User Interface, or by writing a script and running them directly in the Command Window. The nodes and radiative couplings for this thermal model are automatically determined from the defined geometrical model by ESATAN, while the initial conditions, boundary conditions and solution control are specified by the programmer.

6.2.2. Solving the Thermal Model

When a thermal model is created, ESATAN transforms the corresponding nodal network, where the nodes are connected via the thermal couplings, into a system of equations. As the thermal model consists of boundary nodes and non-boundary nodes, there are two types of equations. For the boundary nodes, the boundary condition is transformed into a finite differencing form. For the non-boundary nodes, a finite difference approximation of the Lumped Parameter equation is derived. This is done to make the system of equations solvable for a computer.

In this subsection, the working of this process is described for the conductive part of the analysis. The radiative and convective parts are derived with the exact same method, so they will not be treated here.

Lets consider a nodal network that has a rectangular grid. For random node N0, only the adjacent nodes have to be taken into account to derive the finite differencing form of the lumped parameter equation f. Therefore, only node N0 and its four adjacent nodes N1, N2, N3 and N4 are considered when explaining the procedure. This part of the rectangular grid is displayed in figure 6.1. The goal here is to derive a first order finite difference approximation of the heat equation, which is shown in equation 6.2.

$$\frac{\delta T}{\delta t} = \alpha \nabla^2 T = \frac{\kappa}{\rho c_p} \left(\frac{\delta^2 T}{\delta x^2} + \frac{\delta^2 T}{\delta y^2} \right) \quad (6.2)$$

To calculate $\nabla^2 T$, T is expanded in a Taylor series about point N0, which leads to the following expressions for T_1 , T_2 , T_3 and T_4 .

$$T_1 = T_0 + \frac{\delta T}{\delta x} s_1 + \frac{\delta^2 T}{\delta x^2} \frac{s_1^2}{2} + \frac{\delta^3 T}{\delta x^3} \frac{s_1^3}{3} + O(s_1^4) \quad (6.3)$$

$$T_2 = T_0 + \frac{\delta T}{\delta y} s_2 + \frac{\delta^2 T}{\delta y^2} \frac{s_2^2}{2} + \frac{\delta^3 T}{\delta y^3} \frac{s_2^3}{3} + O(s_2^4) \quad (6.4)$$

$$T_3 = T_0 + \frac{\delta T}{\delta x} s_3 + \frac{\delta^2 T}{\delta x^2} \frac{s_3^2}{2} + \frac{\delta^3 T}{\delta x^3} \frac{s_3^3}{3} + O(s_3^4) \quad (6.5)$$

$$T_4 = T_0 + \frac{\delta T}{\delta x} s_4 + \frac{\delta^2 T}{\delta x^2} \frac{s_4^2}{2} + \frac{\delta^3 T}{\delta x^3} \frac{s_4^3}{3} + O(s_4^4) \quad (6.6)$$

It can be seen that the two equations for odd temperatures deal with unknowns in the x direction and the two equations for even temperatures deal with unknowns in the y direction. Therefore, the equations for T_1 and T_3 can be solved for $\frac{\delta^2 T}{\delta x^2}$, and the equations for T_2 and T_4 can be solved for $\frac{\delta^2 T}{\delta y^2}$. The resulting equations can then be substituted in the heat equation. If higher than second order terms are neglected, the heat conduction equation evaluated at N0 becomes the following:

$$\frac{dT_0}{dt} \approx 2 \frac{\kappa}{\rho c} \left[\frac{T_1 - T_0}{s_1(s_1 + s_3)} + \frac{T_2 - T_0}{s_2(s_2 + s_4)} + \frac{T_3 - T_0}{s_3(s_1 + s_3)} + \frac{T_4 - T_0}{s_4(s_2 + s_4)} \right] \quad (6.7)$$

For a steady-state analysis, the fraction $\frac{dT_0}{dt}$ is equal to 0, so the only unknown parameters are the temperature of every node. Furthermore, in a steady-state analysis, there is one equation for every node in the system. This means that there are as many equations as there are unknown parameters, thus the system of equations can be solved. For a transient analysis, however, several extra steps have to be taken.

The first extra step is to apply a time-related finite difference scheme to the equation. An example of such a scheme is a forward differencing scheme, which looks like this.

$$\frac{dT_0}{dt} \approx \frac{T_{0,t_{n+1}} - T_{0,t_n}}{\Delta t_n} \quad (6.8)$$

By substituting equation 6.7 this can then be rewritten to:

$$T_{0,t_{n+1}} \approx T_{0,t_n} + \Delta t_n \cdot 2\alpha \left[\frac{T_{1,T_n} - T_{0,T_n}}{s_1(s_1 + s_3)} + \frac{T_{2,T_n} - T_{0,T_n}}{s_2(s_2 + s_4)} + \frac{T_{3,T_n} - T_{0,T_n}}{s_3(s_1 + s_3)} + \frac{T_{4,T_n} - T_{0,T_n}}{s_4(s_2 + s_4)} \right] \quad (6.9)$$

With these extra equations - n equations for every time step Δt_n - enough equations are present for transient analyses to also be performed. [26]

6.3. Selecting a Method for the Thermal Analysis

The second choice that has to be made is concerned with the methodology that will be followed for the execution of the thermal analysis. In this section, the methodology of the thermal analysis is presented, including an explanation of why these methods were selected and how they will influence the results. In subsection 6.3.1, an overview of the different methods is given, as well as a description of the method selection process. Furthermore, in subsection 6.3.2, it is explained which of the methods has been selected.

6.3.1. Three Possible Methods

As described in subsection 6.2.1, the standard analysis method of ESATAN is to create a geometric model of the to-be-modelled satellite and using the output of this model as input to a thermal model. With the thermal model, the actual thermal analysis is performed. This is, however, not the only option. During the literature study, two additional methods for using ESATAN have been identified. In this subsection, it will be explained how these additional methods work and the method selection will be described.

Firstly, it is possible to build only a thermal model. In this case, the incoming fluxes, if any, and thermal couplings of the model can be determined and included manually. Computing the radiative couplings in this way can be computationally intensive, especially for bigger models, or models that consist of complex geometries. Therefore, this is not a convenient method for such models. Instead, the method is useful for models where only a small system is modelled, but for which it is not necessary to build and model the whole satellite in ESATAN. Furthermore, it is useful when ESATAN would be used for non-space applications. In the remainder of this section, this method will be referred to as the input-by-hand method. In figure 6.2, a graphical representation of the method is shown.

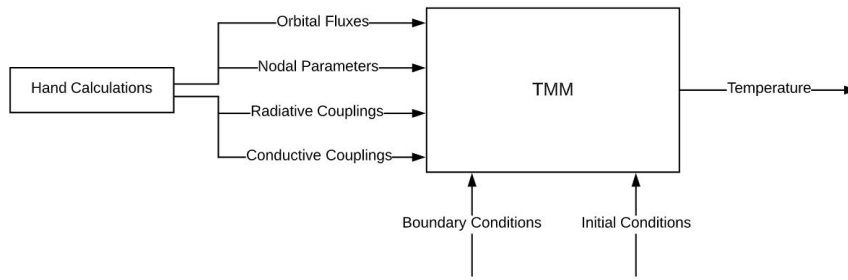


Figure 6.2: Graphical representation of the Input-by-Hand Method

Secondly, a combination of the two previous methods can be applied. This method is called the combination method, and is illustrated in figure 6.3. Whereas in the standard method, the nodes of the geometric model and their characteristics are automatically copied to the thermal model by ESATAN, there is no direct link between the geometric and thermal models in this method. Instead, the geometric model is only used to calculate inputs for the thermal model and the nodes of the thermal model are defined separately. Stronger, in the combination method, the geometric model can even be built in another computer program. The difference between the two methods can also be seen when comparing figure 6.4 to figure 6.3. Three differences with the standard method stand out. In figure 6.3, there is no arrow going from the GMM directly to the TMM. Furthermore, the conductive couplings are hand calculated instead of calculated in the GMM. Finally, the nodal parameters are no output from the GMM, but are specified in the TMM.

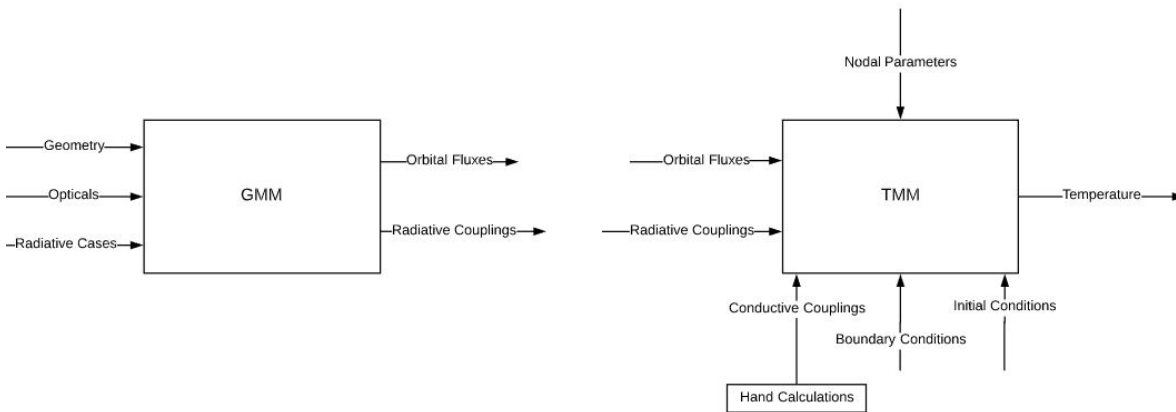


Figure 6.3: Graphical representation of the combination method

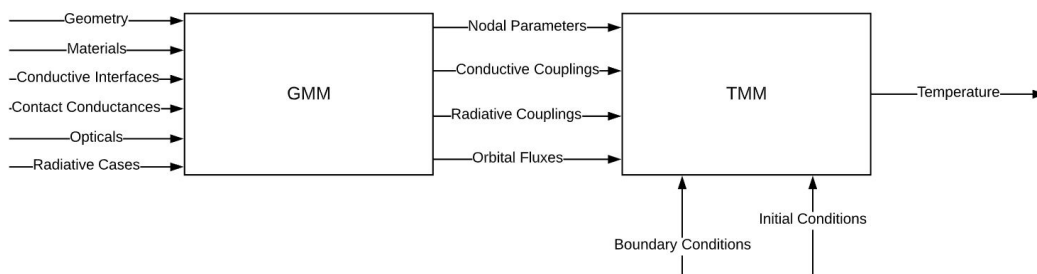


Figure 6.4: Graphical representation of the standard method

By using the combination method, the radiative couplings and orbital fluxes (solar, albedo and infra-red) are not required to be calculated by hand, while the advantages of the previous method, most importantly not having to model the whole satellite in detail, are still valid. This makes this method a viable alternative for bigger models or models with more complex geometries.

6.3.2. The Method Selection Process

As explained before, three thermal analysis methods have been identified: the standard method, the input-by-hand method and the combination method. One of these methods will be selected for the thermal analysis. As the method selection will have a major influence on the remainder of the thermal analysis, the selection process will be described in the following paragraphs. First, an explanation will be given as to why the standard method will be discarded, after which the selection of one of the other methods will be described.

The Standard Method

The standard method was the first option to be discarded, because of several reasons.

First, the CORE hinge is only a small part of the Deployable Space Telescope. Thus, it is not necessary to model the whole telescope in detail, which is what the standard method is optimised for. Second, the thermal tests of the DST CORE hinge were not conducted in a vacuum. Therefore, convective heat transfer occurred in the test. If the results of the thermal tests are to be used for validating the thermal model, the convective heat transfer has to be modelled. This is not possible in ESATAN Workbench, but it is possible with the input-by-hand and combination methods.

The final reason has to do with the two types of geometries that can be used for the model building: shells and solids. Shells are the most simple type of geometry, which consists of only one node that represents the whole geometry. This node contains information on the heat capacity of the node, as well as the surface properties and the surface area of the node.

The solid geometry type consists of both a solid node, representing the mass and thus the heat capacity of the geometry, and surface nodes, which represent the surfaces of the geometry and contain information on the surface properties and surface area of the surface. Originally, the shell geometry type was the only available type in ESATAN. In a later version of the programme, the solid type was introduced, in order to facilitate analysing temperature gradients in materials.

An additional advantage of the solid geometry type is the fact that it allows more complex geometries to be represented by ESATAN. This makes it possible to build an accurate geometric model of the DST CORE hinge, as the shell type did not offer the possibility to model parts of the CORE hinge, for instance the cams. However, according to Niels van der Pas, who is a thermal engineer at Airbus DS the Netherlands, for models in which the geometry is represented by a small amount of solid nodes only, considerable modelling inaccuracies can occur, which is not wanted. Because of this and the fact that the CORE hinge geometry can only be built accurately using the solid geometry type, the standard method is the least applicable method and is thus discarded.

Input-by-Hand

The input-by-hand method is an attractive method for the CORE hinge thermal analysis, as the CORE hinge is only a small part of the Deployable Space Telescope and the input-by-hand method is, as indicated before, better suited for thermal analyses on a component level. However, two main problems have been encountered with this method, which have to do with the geometrical complexity of the DST CORE hinge. These problems are caused by the calculation of the radiative couplings on the one hand and the calculation of the orbital fluxes on the other.

As stated before, using the input-by-hand method for bigger models, or models with complex geometries, can be computationally intensive. This is due to the calculation of the radiative couplings between the nodes, more specifically the calculation of the Gebhart factors. This is the first main problem, but before it is treated, it is important to know how radiative couplings are calculated.

$$B_{ij} = F_{ij}\epsilon_j + \sum_{k=1}^n (1 - \epsilon_k)F_{ik}B_{kj} \quad (6.10)$$

The radiative coupling between nodes i and j is calculated using the equation: $GR(i, j) = \epsilon B_{ij}A$. Here, B_{ij} is the Gebhart factor from i to j , which is defined as the ratio of energy absorbed at node j that originates from

node i , divided by the total radiation emitted from node i [6], and is calculated in practice by using equation 6.10. As can be seen in the equation, one of the parameters needed for calculating Gebhardt factors is the view factor F . View factors can be calculated in two different ways.

$$F_{ij} = \frac{1}{A_i} \int_{A_i} \int_{A_j} \frac{\cos\theta_i \cos\theta_j}{\pi s^2} dA_j dA_i \quad (6.11)$$

The first method of calculating a view factor F_{ij} is dividing two surfaces i and j into many differential surfaces dA_i and dA_j and evaluating the double integral shown in equation 6.11. The definition of s , dA_i , dA_j , θ_i and θ_j is given in figure 6.5. In order for the results of this method to be accurate, the surfaces have to be divided into many differential surfaces. As each of the differential surfaces of A_i must be connected to each differential surface of A_j , a big amount of calculations has to be done, which makes this method time consuming.

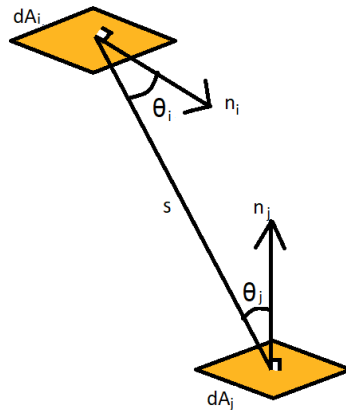


Figure 6.5: Definition of s , dA_i , dA_j , θ_i and θ_j

The other method uses tables and graphs that have been generated by evaluating the view factors of many configurations of standard geometries. This is done by evaluating the double integral in equation 6.11. These tables and graphs are then used to calculate several of the view factors in the system, after which the other view factors are determined using simple rules. Examples of these rules are the reciprocity rule, $A_i F_{ij} = A_j F_{ji}$, and the rule that the summation of all view factors from a single surface is 1.

In the above, two difficulties can be identified. First, as can be seen in equation 6.10, the view factors and Gebhardt factors of all other surfaces are required for the calculation of the Gebhardt factor of a single surface. This means that the bigger the model is, the more time has to be spent to calculate a single Gebhardt factor. Second, if the view factors within a part cannot be calculated using the predefined tables and figures, for example if the part consists of non-standard, complex geometries, evaluating the double integral in equation 6.11 becomes necessary. This is time consuming as well. These two difficulties combined are causing the first problem. As the DST CORE hinge mainly consists of geometries that are not specified in the predefined tables and figures and because the amount of nodes will be considerable, calculating the radiative couplings by hand will take a lot of time.

The second main problem, which is related to the calculation of the orbital fluxes, is that the magnitude of the fluxes on a node is dependent on many parameters. These are, for instance, the position of the satellite along the orbit, the attitude of the satellite with respect to the earth and the relevant position of the node to the other nodes in the model, which cause shadowing effects. Due to the amount of dependencies, calculating the solar, albedo and infra-red fluxes for all nodes by hand will take a lot of time.

The Combination Method

It has been determined that calculating the inputs to the thermal model by hand can be very time consuming. The combination method solves this considerable disadvantage of the input-by-hand method, by applying a Monte-Carlo ray-tracing (MCRT) algorithm for determining the radiative couplings and orbital fluxes. MCRT algorithms are mainly used in optics, but have also proven to be a reliable method of approximating the view

factors in a system. The algorithm works by sending a finite number of thermal radiation energy packets, referred to as rays, from a radiative surface in random directions, after which it records, for every radiative surface a ray encounters, how much of the energy is absorbed and reflected. Furthermore, the method takes multiple reflections per ray into account, which is why MCRT is also useful for calculating Gebhardt factors. Additionally, MCRT can be used to determine orbital fluxes. Here, the Earth and the Sun are also considered to be radiative surfaces. An MCRT algorithm has been implemented in ESATAN, where it is used for calculating the radiative couplings, as well as the solar, albedo and infra-red radiation for every node in the model. To be able to use the MCRT algorithm, the geometric model has to be defined, to let the algorithm know when a ray encounters a geometry.

Within the combination method, there are two possibilities. The first possibility is to write an own Monte-Carlo ray-tracing algorithm. The second possibility is to use a readily available algorithm.

Because of a lack of knowledge on how to write an MCRT algorithm and the amount of time that it would take to write such an algorithm, this option would not be ideal. Instead, it would be preferred to use a readily available MCRT algorithm.

The Method Selection

Now that the main advantage of using the combination method over the input-by-hand method has been identified, the choice between these two methods is clear; the combination method is selected for the thermal analysis of the DST CORE hinge. The main reason for this selection is the fact that both the radiative couplings and the orbital fluxes can be calculated using one single model; building the geometric model requires some work, but it solves two problems in one go.

As stated before, it would be preferred to use a readily available MCRT algorithm. It was decided that the Monte-Carlo ray-tracing will be performed with ESATAN, as ESATAN already contains such an algorithm. Therefore, both the geometric model and the thermal model are built in ESATAN. In practice, this works work as follows. First, a geometric model of the CORE hinge is built, using only geometries of the solid type. Afterwards, the thermal model is generated, where the solid and surface nodes are combined into one diffusion node. This diffusion node is similar to a node of a shell geometry, and it contains the heat capacity defined in the solid node, the surface properties defined in the surface nodes and the incoming heat flux from all surface nodes combined.

The process of building the geometric model and the thermal model, as well as the resulting models, will be described in chapters 7 and 8, respectively.

7

The Geometric Mathematical Model

It has been determined that the model of the DST CORE hinge will consist of a geometric model and a thermal model. The geometric model is a geometrical representation of the satellite that is to be modelled. Whereas the nodes in a thermal model only represent a point mass with a specified surface area and optical properties and are thus one dimensional, the nodes in the geometric model represent a geometry and are three dimensional. In this chapter, the process of building the geometric model, referred to as GMM, is described after which an overview of the resulting model and its characteristics is given. The chapter will end with a comparison between the geometric model and the real CORE hinge. In section 7.1, two guidelines for building the geometric model of the CORE hinge are explained. Consequently, a description is given of the already existing geometric model for the DST in section 7.2. In section 7.3, the building process of the DST CORE hinge is described and finally, in section 7.4, the resulting geometric model is presented.

7.1. DST CORE Hinge Geometric Model

The geometric model will be used to determine the incoming fluxes on the hinge and the radiative heat couplings between the different parts of the hinge. In this section, the process of building the geometric model of the CORE hinge is described.

During the initial stages of the thesis project, two guidelines have been defined for building the geometric model. Firstly, the geometric model of the CORE hinge has to be representative for the real CORE hinge. This is because the accuracy of the thermal analysis results can only be as high as the accuracy of the model when compared to the actual CORE hinge. This can be difficult to achieve due to the challenges associated with the limited amount of geometry types. These challenges will be treated in subsection 7.3.1.

Secondly, although the CORE hinge is the only part of interest, it is necessary to include the parts of the DST that block the radiation from the Sun and the Earth in the Geometric model. This in order to obtain an accurate result for the orbital fluxes. In the case of the DST CORE hinges, this is mainly important for the solar flux; as the DST is always pointed towards the Earth, the CORE hinge constantly has an almost unobstructed view of the Earth's surface, so the other parts of the DST will have a negligible influence on the albedo and infra-red radiation, which comes from the Earth's surface.

Another reason for including the other parts in the geometric model is that, in real life, the non-CORE hinge parts of the telescope will be irradiated by or radiating onto the CORE hinge in real life, changing the temperature of both. Including these in the model as boundary nodes, will make the model more accurate.

The non-CORE hinge geometries are based on the geometries of the DST geometric model, described shortly in the next section. Some of them are simplified quite a bit. The three other CORE hinges, secondary mirror and spider are, for instance, approximated by a rectangular prism. This does not influence the amount of radiation that they block, as the maximum dimensions of the prisms are the same as the original components. The following geometries are included: the baffle, the baffle bottom, the booms, the other CORE hinges, the connections between the hinges and the spider, the spider itself and the secondary mirror. Some geometries are not included, as they have almost no influence on the solar and infra-red radiation that reaches the CORE hinge.

7.2. Geometric model for the DST

Before the start of this thesis, a model of the Deployable Space Telescope had already been made. This model was built by Tim van Wees, whose thesis was concerned with a thermal analysis of the whole telescope[37]. This model was later adapted by Jan-Willem Arink[2] and Ilja Akkerhuis, to represent design changes and modelling inaccuracies. As this model adheres to the second guideline, without a need for adding parts, it was considered to use this model for the thermal analysis of the CORE hinge, but soon after it became clear that another approach was necessary. Although the model adheres to the second guideline, the model fails to adhere to the first guideline: being representative for the real CORE hinge. In the existing geometric model of the DST, the CORE hinge is not accurately represented. The DST CORE hinge is quite complex, but the representation in the DST model is not. Not only is the shape of the cams simplified, the strips connecting the cams are not present in the model at all. Therefore, a more detailed geometric model of the CORE hinge has to be built in order to obtain accurate results. In the next subsection, the process of building this more detailed model is highlighted.

7.3. Building the geometric model of the DST CORE Hinge

As explained in section 6.2, a geometric model can be built in two ways: either by using ESATAN-TMS Workbench, or by programming the model and running it in batch mode. Working in Workbench is much easier to understand, as this follows a very straight-forward method, which is well documented. The downside of using ESATAN-TMS Workbench however, is the fact that it is more difficult to copy parts, or to apply changes to several identical parts at the same time. Therefore, if a detailed model of a whole satellite or system is made, programming the model is a more convenient method than using Workbench. However, for less experienced engineers, or for small thermal models of components, using Workbench is the preferable method. That is why, for this thesis project, the geometric model will be built in Workbench.

The process of building a geometric model in ESATAN-TMS Workbench can be summarised in two main modelling steps: defining the geometry and defining the radiative case. In this section, a walk-through is given for the geometric modelling process. Additionally, a reflection on the modelling process of the CORE hinge model will be present. In subsection 7.3.1, the geometry definition process is highlighted and in subsection 7.3.2, the process of defining the radiative case is provided. Finally, in subsection 7.3.3, it is explained how to run the radiative case.

7.3.1. Defining the Geometry

Several actions have to be performed to define a geometry in Workbench. In this subsection, a short explanation of these steps is given, and the execution of each step for the CORE hinge model building process is described.

Material Properties Definition

The first step is to define the material properties. Here, two categories exist, which are 'Bulks' and 'Optical Sets'. The Bulks refer to the main materials, like Aluminium or Titanium, of which the geometry is made. These materials are important for calculating the conductive couplings. For each bulk, the density, specific heat and conductivity of the material are defined.

The Optical Sets are the optical coatings that are applied on the geometry. These are necessary for calculating the radiative couplings. The properties of the optical sets are divided in Infrared and Solar properties. In the window that is displayed in figure 7.1, the emissivity/absorptivity, transmissivity and specular reflectivity have to be defined. The diffuse reflectivity is then calculated by ESATAN itself.

For the CORE hinge model, only one bulk and one optical set are applied, as the whole hinge consists of titanium and is coated in black paint. The definition of the black paint is shown in figure 7.1. For the titanium bulk, the density is 4400 kg/m^3 , the specific heat is 565 J/kgK and the conductivity is 7.2 W/mK . Additionally, three extra optical sets have been defined for the non-CORE hinge parts of the model. These are:

1. **SSiC** Used for the secondary mirror, with an emissivity of 0.05 and a absorptivity of 0.254.
2. **Baffle** Used for the baffle, like the name indicates. It is actually the black paint that is used on the inside of the baffle. It has an emissivity of 0.84 and an absorptivity of 0.93.

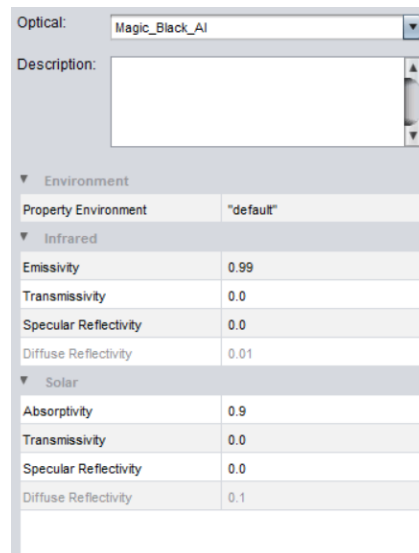


Figure 7.1: Optical Set definition window with the values of the DST CORE Hinge Coating.

3. **Bottom Average** An optical with values averaged over the visible baffle bottom and primary mirror, with baffle black paint and silicon carbide, respectively. Has an emissivity of 0.9 and an absorptivity of 0.95.
4. **MLI** The optical that is used for the outside of the baffle. Has an emissivity of 0.14 and an absorptivity of 0.19.

Geometry Construction

After the Bulks and Optical Sets are defined, the model can be constructed. When the define geometry option is selected, the window of figure 7.2 is opened. On the top of the window, there are three tabs. The Geometric and Properties tab have to be filled out, while the Diagrams tab displays the node and point definition for the selected shape and geometry type. For every geometry that the model consists of, the same properties have to be defined. To illustrate this, the geometric definition window and properties window of one of the parts of the CORE hinge model are shown in figures 7.2 and 7.3, respectively. The parameters under the Geometric tab are the following:

- **Geometry Name** This is the name of the geometry, which will be displayed in the analysis file and in the outputs next to every node number.
- **Shape** This determines the shape of the cross-section of the geometry or the geometry itself. Several shapes are available, which are: cone, cylinder, disc, paraboloid, quadrilateral, rectangle, sphere, trapezoid, and triangle. Note that some of these shapes can be defined as shell and/or solid, some only as a shell and others only as a solid.
- **Geometry Type** Here, it can be defined whether the geometry is a shell or a solid. These refer to the explanation of section
- **Definition Method** The geometry can be defined by parameters, points, or directions. The latter will not be used and is thus not treated here. If defined by points is selected, the corners of the geometry are defined in x,y and z coordinates. If parameters is selected, the dimensions of the geometry are given. The origin of the geometry will then automatically be placed at the origin of the model.
- **Parameters** Here, the parameters or corner points are defined.
- **Transformation** Here, the geometry can be rotated and translated w.r.t. the three axes. This is mainly used to move a parameter defined geometry from the origin of the model to its required position. The application order at the bottom determines the order of the translations and rotations.

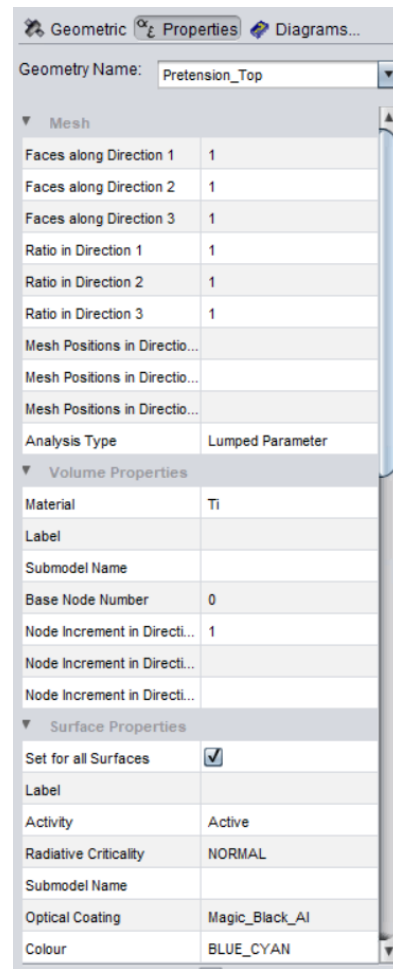
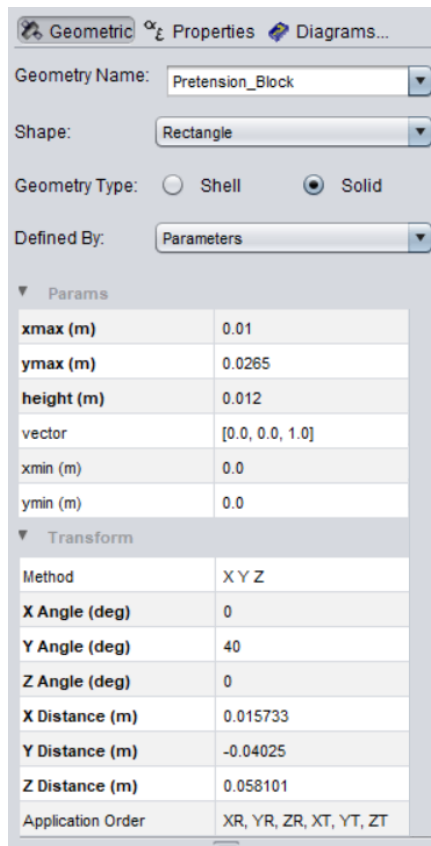


Figure 7.2: The Geometric window of the geometry definition Figure 7.3: The Properties window of the geometry definition

As can be seen in figure 7.3, the Properties tab is divided in three sections.

- **Mesh** Here, the geometry can be divided into multiple nodes. The amount of nodes per direction and, if needed, the ratio per direction can be defined. If the result of these options is not good enough, the starting points of every node along a direction can even be defined.
- **Volume Properties** The Bulk material and node number for the geometry are applied here. If kept empty, the node numbering will be determined by Workbench.
- **Surface Properties** In this part, the Optical Set material of the geometry can be defined, and a colour can be assigned to the geometry, which will be the colour of the geometry in the Workbench display.

As an example, the geometry defined in figures 7.2 and 7.3 leads to a solid rectangle of 10 by 26.5 by 12 mm, which is first rotated by 40° around the y-axis and the origin of which lies at point (15.733; -40.025; 58.101) mm. It consists of one node, and is made of titanium, which is coated in Magic_Black_AI, which is the name of the black paint.

The limited amount of geometry types that can be used in ESATAN causes some challenges in the geometric modelling of the CORE hinge. First, most of the sharp edges in the CORE hinge are filleted. In Workbench, there is no option for adding fillets. Either the filleted edges are not incorporated in the model, or another geometry type, like the triangle geometry, is used to approximate the fillets. The second challenge occurred while modelling the parts of the hinge in which one side of the geometry is curved, whereas the other side is straight. This can either be neglected, or two geometry types could be combined to approximate the real geometry. For simplicity, and because several geometries are needed to model these parts with reasonable

accuracy, it was decided to model these parts with one geometry only.

After all geometries are defined, they have to be assigned to a model. This way, ESATAN knows which geometries it should use for building the model. However, before this is done, the geometries can be grouped together to help structure the eventual model and to create a logical overview of the spacecraft components. The CORE hinge geometric model is subdivided into three main groups, the baffle, the CORE hinge and the rest of the SMSS. The baffle consists of the eight baffle segments and three bottom segments. The SMSS rest consists of all other non-CORE hinge parts that are included in the model.

The main group is of course the CORE hinge itself. This group is subdivided into six parts, each referring to a component of the CORE hinge. These are the lower cam, the upper cam, the plate and the three strips; left, right and middle. This subdivision makes it easier to find nodes of interest and to hide and show different components, as the groups can be hidden or shown with one click. The components were built up one by one, starting with the lower cam and the plate. Afterwards the upper cam was built, and the CORE hinge part was finalised with the strips. Afterwards, the baffle was built and the modelling process was finalised with the SMSS definition. The result of the geometric modelling is described in 7.4.

The final step in the geometry definition stage is to define the conductive interfaces. These indicate which geometries are in contact or fused together and include a contact conductance value for geometries that are in contact. In the case of a fused interface, ESATAN uses the conductivity from the Bulk definition for calculating the conductive coupling. The conductive interfaces can also be automatically generated by ESATAN, but by default, the interfaces are seen as fused. This can, however, be changed by the user.

In the geometric model definition of the CORE hinge, the automatic generation option is used as only a few interfaces had to be changed from fused to contact or not-connected. Furthermore, some of the conductance values are altered slightly to better represent reality as the geometry built in ESATAN will slightly differ from the real geometry. As no margins were taken into account in the model, Workbench identified several interfaces between the cams. However, in real life, there will be some space between the components, so at these points, the interfaces were changed to not-connected.

7.3.2. Defining the Radiative Case

After the geometric model of the satellite has been built, the second modelling step has to be performed: defining the radiative case. A radiative case is defined using the Radiative module of Workbench and consists of three parts: the environment, the orbit and pointing. With the definition of these three parts, ESATAN is able to determine, for every specified point along the orbit of the modelled spacecraft, the attitude of every geometry with respect to the orbited body and the sun. Furthermore, ESATAN is instructed about the infrared temperature and albedo distributions of the orbited body. In this subsection, the environment and orbit definition will be treated. With the pointing definition, it is defined how the modelled satellite is oriented with respect to the orbited celestial body. Furthermore, rotating parts can be defined, such as solar panels always being perpendicular to the sun-planet axis. However, the only important characteristic for the DST is the primary pointing direction, which is nadir pointing, as the telescope shall always be pointed towards the centre of the Earth. The pointing definition is thus not treated further.

The Environment

The environment definition is necessary for ESATAN to know the characteristics of the sun-planet system and the orbited body itself. The environment definition window is shown in figure 7.4. By selecting a particular celestial body, all parameters of the Sun/Planet system are changed accordingly. The sun can also be selected here. Furthermore, it can be selected with respect to which point the inertial reference frame is taken; with respect to the centre of the Sun or to the Vernal point. The latter indicates that the reference frame is with respect to the centre of the planet.

As can be seen in the environment definition window, the environment definition consists of four parts:

- **Sun/Planet System** Here, the characteristic parameters of the celestial body and its orbit around the sun are given, as well as the solar radius. If the Sun is selected as celestial body, only the gravitational acceleration, Sun radius and celestial body image have to be defined. The definition of the celestial body image is only useful for the visualisation of the satellite orbit, and has no influence on the analysis.

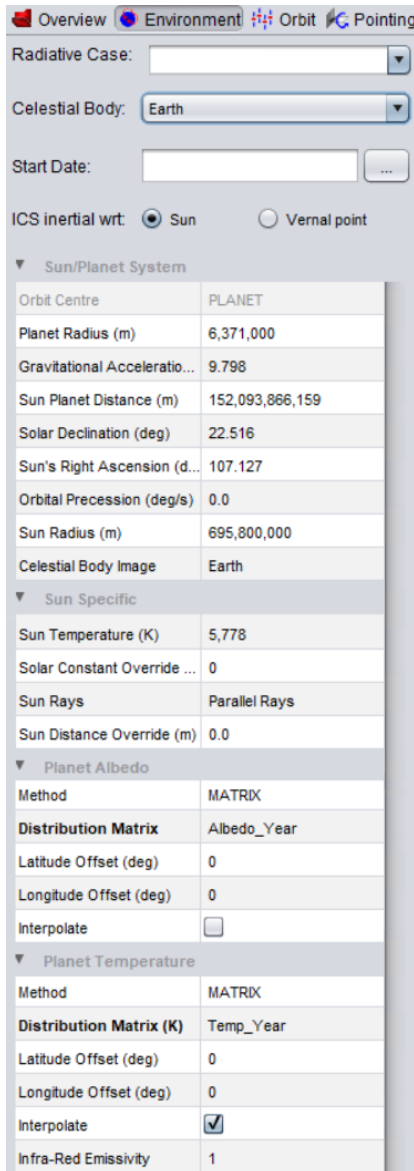


Figure 7.4: Environment definition window for the CORE hinge model

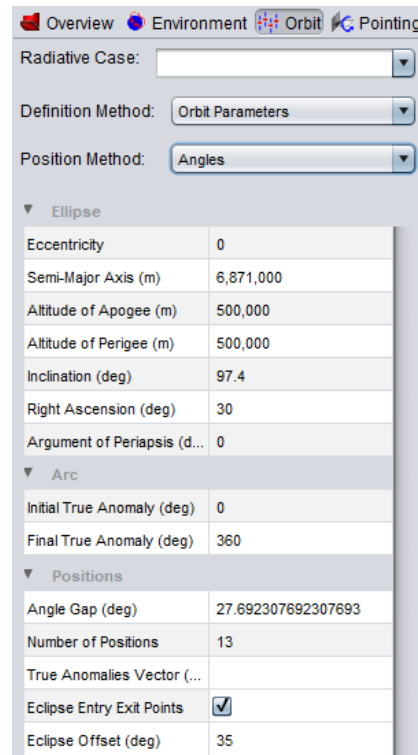


Figure 7.5: Orbit definition window for the CORE hinge model

- Sun Specific** This part is required for calculating the heat flux originating from the Sun and the way the solar rays are incident on the model and planet. If a non-zero solar constant override value is defined, this solar constant will replace the value calculated from the defined Sun temperature. For the sun rays, parallel rays or finite rays can be selected, the latter meaning that the solar rays will be convergent. The angle of the Sun rays is then calculated by Workbench, either from the Sun-planet distance, or from the Sun distance override value.
- Planet Albedo** The planet albedo can be defined in two ways, either by defining a constant value or by defining a matrix. In the matrix, the planet albedo values are given for linearly distributed latitude, longitude combinations.
- Planet Temperature** Here, the same goes as for the planet albedo. Additionally, the infra-red emissivity can be defined. By default, the planet is considered to be a black body, with an emissivity of 1.

As can be seen in figure 7.4, in the CORE hinge model, the planet albedo and temperature values are defined in matrix form, in order to represent the actual albedo and infra-red fluxes more accurately. The result of the

temperature matrix can be seen in figure 7.6, the albedo matrix is very similar, but with different values. The arrays are taken from the most recent DST model [1]. Furthermore, the used Sun and Sun/Planet system data are the default values.

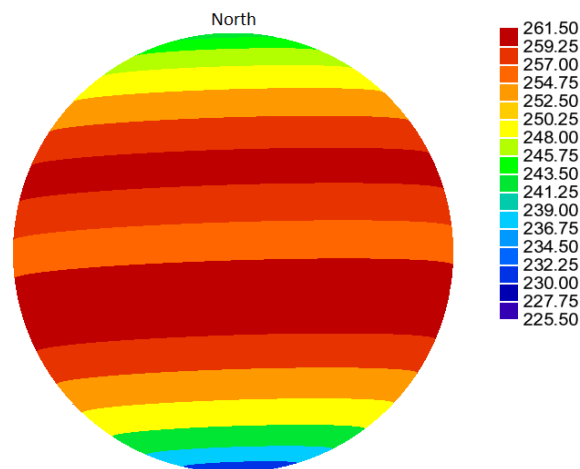


Figure 7.6: Temperature distribution of the Earth from Temperature matrix

The Orbit

Next to information on the planet-sun system, Workbench needs information about the orbit of the satellite itself. This information is provided in the orbit definition tab, which is shown in figure 7.5. The values in this figure are those of the CORE hinge model.

The definition process goes as follows. First, the radiative case has to be named. Then, the definition method has to be selected. Here, two options can be selected. First, the orbit parameters can be given, such as inclination and semi-major axis. The second option is to give an Ephemeris matrix, but this will not be selected and not described here. Then, the position method is selected. This can be angles, or it can be times. Finally, the parameters have to be input in the orbit definition window. As can be seen in this definition window, the orbit parameter definition consists of the following three parts, where the position method only influences the latter two.

- **Ellipse** Here, the orbit of the satellite is defined. For that, the eccentricity, altitude of apogee and perigee are needed, after which the semi-major axis is calculated by Workbench. Furthermore, the inclination, right ascension and argument of periapsis are required. Their definition is shown in figure 7.7, where i is the inclination, ω is the argument of periapsis and Ω is the right ascension. The latter defines the angle between the ascending node of the orbit and the reference line X. The values for the CORE hinge model are retrieved from the most recent orbit definition [2]. Note that the altitudes of apogee and perigee are the distance to the surface of the Earth and not to the centre.
- **Arc** Here, it can be specified which part of the orbit is considered for the analysis case. By default, this goes from 0 to 360 degrees, or from 0 to the time T (orbital period).
- **Positions** This refers to the positions along the orbit at which the orbital fluxes are determined. They can be defined by specifying the angle gap in degrees between two points, after which the number of positions is calculated, or the other way around by defining the number of positions. Furthermore, a vector can be given which defines the true anomaly of every position. Next to the first positions definition, two positions can be added at the eclipse entry and exit points. These can also be offset by several degrees, pushing them slightly towards the sunlit side or the eclipse side of the orbit. If the times position method is selected, the gap between positions is given by a time gap in seconds. The eclipse offset, however, stays in degrees.

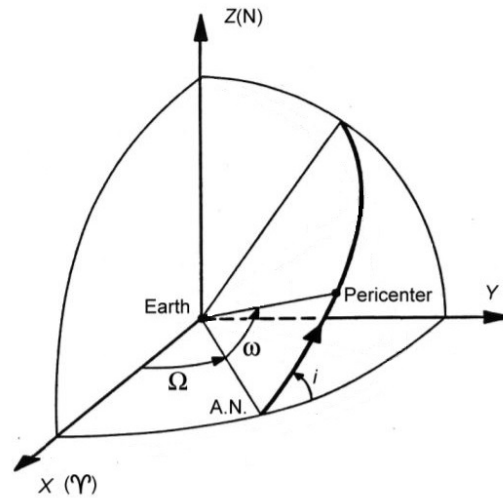


Figure 7.7: Graphical representation of the orbital parameters i , ω and Ω . Obtained from [40] and slightly altered for clarity

7.3.3. Running the Radiative Case

When the radiative case is applied, the window as seen in figure 7.8 is displayed in Workbench. In this figure, the celestial body is shown, and the orbit of the satellite is displayed as well. Where the orbit is green, the satellite is in sunlight, whereas the red part of the orbit shows the eclipsed part of the orbit. The yellow three-dimensional arrow is pointed towards the sun, along the Sun-planet axis. The geometric model is also placed along the orbit, in order to illustrate the starting position of the radiative case. By pressing the buttons below, the other radiative case positions can be shown, and it is also possible to switch on an animation of the different positions. Finally, by clicking on the lower second right icon, all positions will be shown in one view.

In the display window, the displayed size of the planet and the model can be changed. Furthermore, the indications of the ascending node and the periapsis can be switched on and off. The same goes for the planet, the model, the orbit and the sun position arrow.

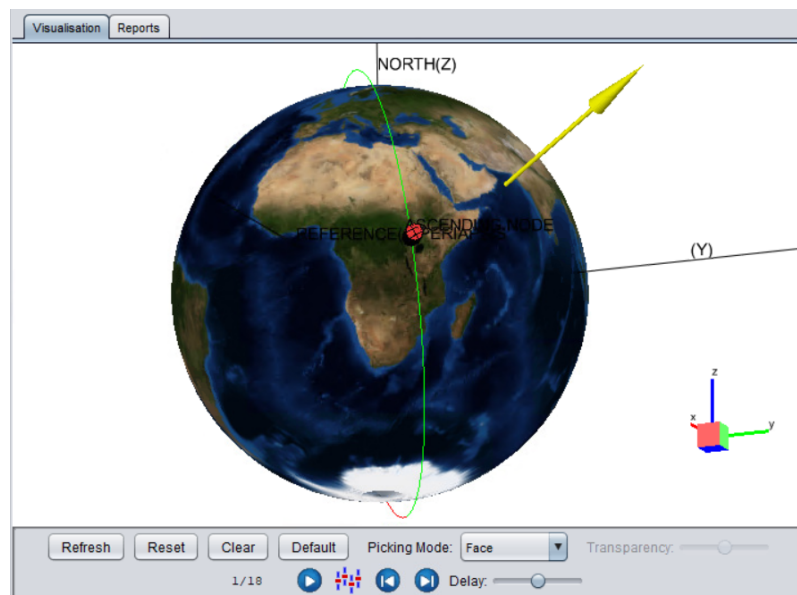


Figure 7.8: Visualisation of the Radiative Case

If the radiative case is as expected, the radiative case can be executed. Before this, Workbench allows the user to change some parameters of the Monte-Carlo ray-tracing algorithm. The ray-tracing procedure will start af-

terwards. ESATAN has three control methods included, each requiring a particular set of control parameters. These methods are the following.

- **Fixed rays** For this control method, a fixed amount of rays is fired from every surface, regardless of the size of the surface. Next to the amount of rays, the ray total cut-off fraction can be defined. Radiative couplings that are a lower fraction of the highest coupling than the cut-off fraction will be assumed to be equal to zero.
- **Line accuracy** Here, a desired accuracy and a required confidence level per face are required as input, after which Workbench determines how many rays have to be fired per surface to reach the required accuracy.
- **Ray density** By selecting this method, the amount of rays that is fired from a surface depends on its surface area, with the ray density defined in the inputs. However, the amount of rays fired is never lower than the fixed rays amount.

Several parameters can be changed for each of the three control methods. The first one is the raytracing seed, which determines the seed for a random number generation during the ray-tracing process. The second parameter is the extinct threshold. This parameter defines the fraction of the initial energy below which an incoming ray will be considered as fully absorbed, in the case of multiple reflections. Finally, it can be decided which calculations will be conducted by the ray-tracing algorithm, by switching them on or off. These are calculating the geometric view factors, the radiative exchange factors, the solar direct flux and solar absorbed flux and finally the direct and absorbed infra-red and albedo flux.

The analysis case of the CORE hinge model is run using the fixed rays method, with a Ray total cut-off of 0.005, 1000 rays from non-critical surfaces, 10.000 rays from normal surfaces and 100.000 rays for critical surfaces. Furthermore, all calculations are performed, except for the UV emission calculations.

7.4. The Resulting Geometric Model of the CORE Hinge

In the previous section, the method for building a geometric model in ESATAN has been described, including an explanation of how this is applied in the modelling of the DST CORE hinge geometric model. The result of the modelling process is highlighted in this section, after which the resulting model is compared to the actual CORE hinge. As already mentioned, the CORE hinge geometric model consists of the CORE hinge and those parts of the DST that influence the thermal behaviour of the hinge. In subsection 7.4.1, the geometric model of the CORE hinge only is described, after which the remainder of the geometric model is treated in subsection 7.4.2. Finally, in subsection 7.4.3, a comparison is made between the geometric model of the CORE hinge only is compared to the actual DST CORE hinge.

7.4.1. The CORE Hinge

The actual CORE hinge consists of six main components, each corresponding to a subgroup of the geometric model. In this subsection, each of these components is shown and a short description of each component is provided. In figures 7.12, 7.14 and 7.16, the CORE hinge geometric model is shown from the front, side and top.

Lower Cam

The lower cam can clearly be seen in the bottom of figures 7.12 and 7.14. It is subdivided into a main cam, consisting of a 100° cylinder segment of width 54 mm and two rectangular blocks, four sub cams, which are built up comparably to the main cam and serve as the contact points to the upper cam, and the sides, which both consist of a triangular prism. In the longitudinal direction, the cylinder segments of the main cam and the sub cams are divided into three nodes, in order to gain a more detailed temperature distribution for these parts. Because this part is perfectly symmetric, it has been decided to not divide the main cam into multiple nodes in the transverse direction.

Upper Cam

The upper cam, which can be seen in figure 7.9, is subdivided into four parts, indicated in different colours. The base is red, the pretension part is blue, the top is green and the spider block is yellow. The base consists of the main cam, the four sub cams that are in contact with the sub cams of the lower cam

and the shear covers, which can be seen in the lower right of the figure. The main cam is built out of four geometries. The main part is a 55° cylinder segment, with a width of 58 mm, which is divided into two nodes in the longitudinal direction and three in the transverse direction. The reason for the latter is the fact that the top of the cam blocks radiation going to the sides of the main cam. It is therefore expected that there will be reasonable temperature differences between the middle and the sides of the cam.

The spider block consists of only two parts: a rectangular block and a triangular prism. The pretension part consists solely of rectangular blocks, each of which consists of one node, as this part has a lower influence on the stability of the hinge. Finally, the top consists of a triangular prism and several quadrilateral prisms. The outer horizontal prisms are actually one geometry, which is divided into two nodes, as this is a big geometry. This is the only geometry where a ratio is defined, which is equal to 0.82, in order to have the same node border as the adjacent horizontal geometries.

At the border between the top and base segments of the upper cam, a curved geometry is connected to several non curved geometries (two quadrilateral prisms and a rectangular block). As the amount of semi-curved geometries available in Workbench is very limited, if there even are any, there are only two solutions. First, curved and non curved geometries can be connected. Second, one curved geometry can be approximated by many triangles. As the latter would lead to many small geometries and thus many small nodes, it was decided to use the first solution, after which the conductive thermal couplings that are determined by ESATAN are replaced by hand-calculated values.

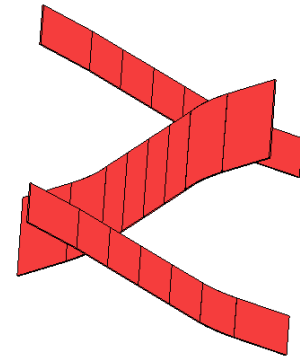
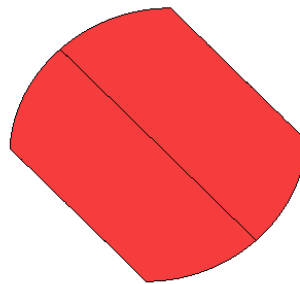
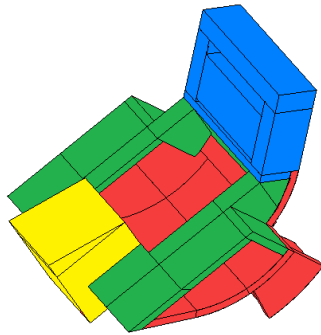


Figure 7.9: Upper cam with different parts in colour

Figure 7.10: Geometric model of the plate

Figure 7.11: Geometric model of the strips

Plate

The plate of the CORE hinge consists of two semi circular shells, which are cut by a hidden vertical plane. As cutting operations can only be performed on shell geometries, the plate is the only geometry that is not of the solid type. For the plate geometries, a thickness of 2 mm is defined, which is equal to the thickness of the plate in the DST CORE hinge.

Strips

There are three strips in the CORE hinge. The side strips are perfect copies of each other and the middle strip is similar to the side strips, but broader. The side strips each consist of one 17.1° cylindrical element, and three thin rectangular blocks. The middle block is divided into four nodes to get a more accurate temperature distribution of the strips. This is done because thermal expansion of the strips has a major influence on the stability of the CORE hinge as a whole. The part that is connected to the top cam has a slight inclination with respect to the middle part, so the conductive thermal coupling calculated by ESATAN is inaccurate. Therefore, this thermal coupling will be calculated by hand.

For the middle strip, which differs more from the side strips than broadness alone, two cylindrical elements are present, instead of one. These are 22.7° and 21.5° long. Note that all four cylindrical elements present in the strips are connected to the main cams over their whole surface area. Also for the mid strip, the middle block is divided into four nodes, to get a more accurate distribution.

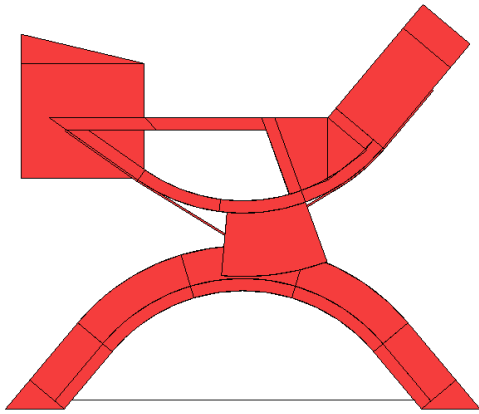


Figure 7.12: Side view of the CORE hinge model

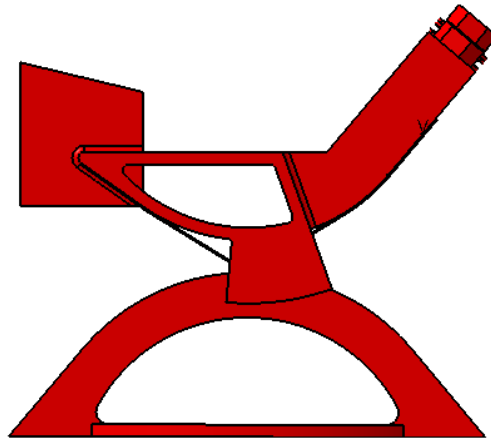


Figure 7.13: Side view of the DST CORE hinge

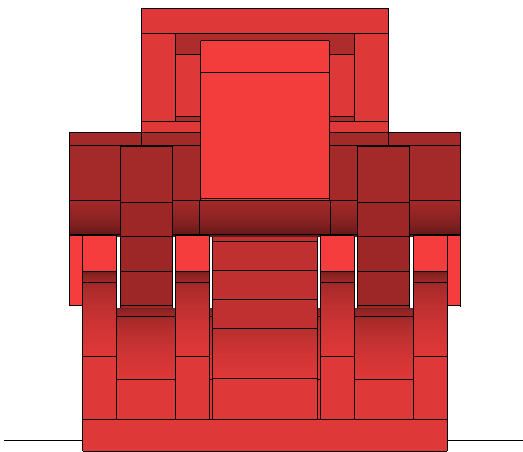


Figure 7.14: Front view of the CORE hinge model

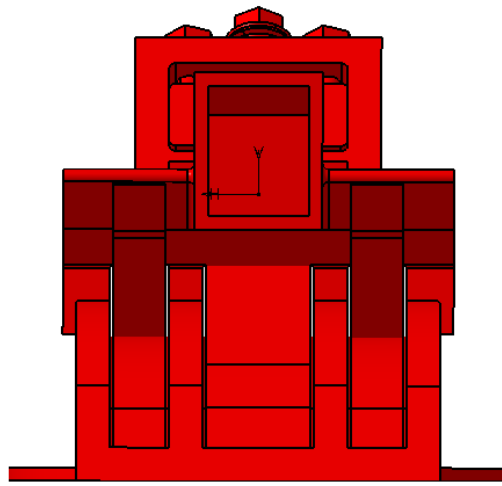


Figure 7.15: Front view of the DST CORE hinge

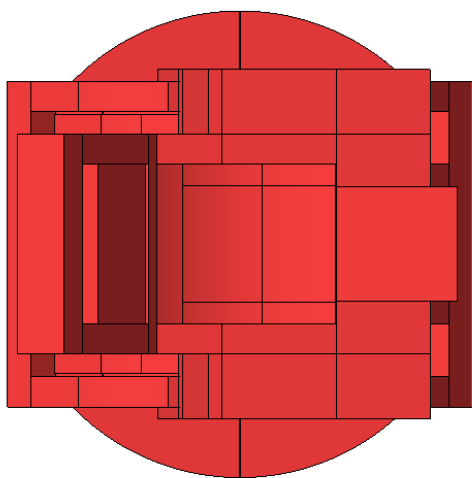


Figure 7.16: Top view of the CORE hinge model

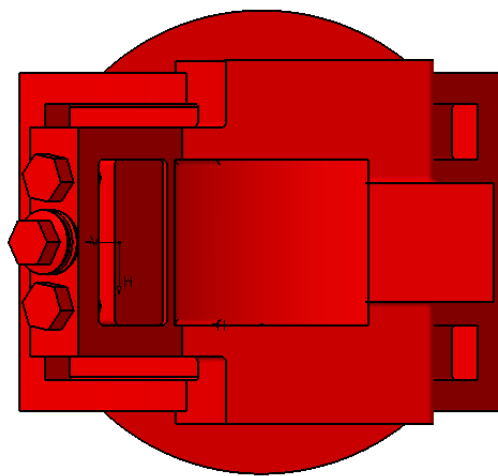


Figure 7.17: Top view of the DST CORE hinge

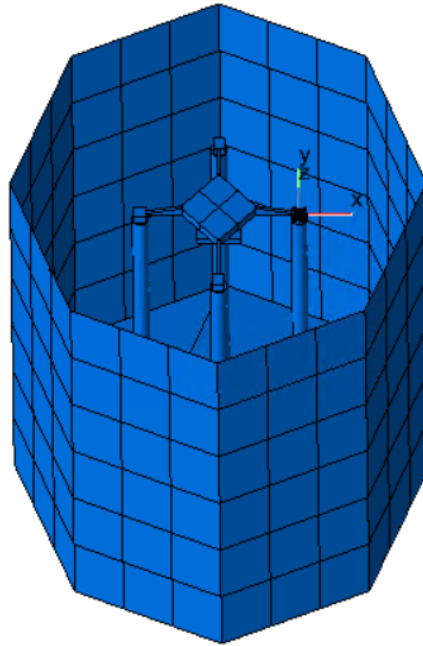


Figure 7.18: The full geometric model

7.4.2. The Other Geometries

In figure 7.18, the whole geometrical model is shown. It can be seen that the origin of the model is not at the centre of the model. This made modelling the rest of the DST slightly more difficult, but will not have an influence on the results of the model.

The baffle is modelled by eight rectangular shells, divided into 6x3 nodes. They surround the baffle bottom, which consists of two trapezium shaped shells and a rectangular shell. They mainly shield the CORE hinge from solar radiation, but also reflect some radiation from the CORE hinge back to the CORE hinge. Due to this, parts of the CORE hinge don't have to be in each others line of sight in order to radiate heat onto each other.

Adding the SMSS has an influence on the amount of solar radiation that is incident on the CORE hinge. The baffle shields the CORE hinge from solar radiation for most of the orbit, but close to the eclipse, some sunlight will pass over the top of the baffle onto the CORE hinge. For that point along the orbit, which is expected to be the most interesting part regarding CORE hinge stability, including the SMSS in the model will make the results more accurate.

7.4.3. Comparison to the DST CORE Hinge

Now that the CORE hinge geometric model is shown and described, the model can be compared to the actual CORE hinge, as built in CATIA. For this, the non-CORE hinge geometries are not considered. In figures 7.12 to 7.17 on the previous page, three views of the CORE hinge CATIA model and the CORE hinge model are shown next to each other, to be able to compare the geometric model of the CORE hinge to the CORE hinge itself. The CORE hinge has been built according to the CATIA, so it is assumed that they are basically the same.

In general, it can be seen that the geometric model is almost the same as the actual CORE hinge, but there are several differences between the two. One of these differences has already been described in subsection 7.3.1, which is the absence of fillets in the model.

The easiest visible difference can be found in the pretension part, as the bolts and washers that apply the pretension to the strips are not present in the model. Because of simplicity reasons and the fact that it is impossible to model drilled holes in ESATAN, it is assumed that the minor influence they have on the temperature of the surrounding parts is negligible. Instead, the bolts have been replaced by conductive interfaces between the pretension and pretension block, as they will conduct heat from the top of the pretension part to the pretension block.

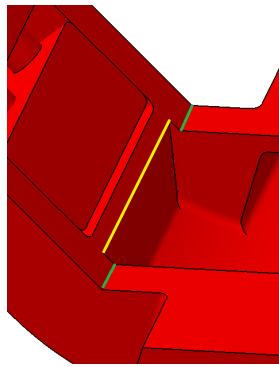


Figure 7.19: Illustration of the difference between the start of the gap (yellow) and the start of the top of the upper cam (green)

If a closer look is taken at the side and top view of the model and actual hinge, more specifically to the spider block, it can be seen that the top part of the upper cam is longer in the model than in the actual hinge. This has to do with a modelling decision regarding the interface between the top and the pretension parts. In the actual hinge, the gap in the upper cam top does not coincide with where the top starts. This difference is illustrated in figure 7.19. This was difficult to model and was thus disregarded. The top is slightly higher in the model than in the actual hinge due to this decision. This height difference is also the cause for the horizontal part being longer in the model, as the angle that the straight part of the main cam makes with the horizontal axis is not altered.

The final difference can be found in the spider block. The pocket that is present in the block is not regarded in the geometric model. This has been done because adding the pocket to the model would make the geometry of the block more complex, while it is not necessary to include it. This is not necessary because the connection between the spider and the CORE hinge should fit perfectly into the pocket. Instead, the connection is modelled as if it is fused to all four sides of the spider block pocket.

8

Thermal Mathematical Model

Following the methodology determined in chapter 6, the results of the geometric model are used in the thermal model. In this thermal model, the geometry is compressed into a nodal network, consisting of nodes that are connected via thermal couplings. Furthermore, the nodes represent the CORE hinge geometry. In this chapter, the process of building the thermal model, referred to as TMM, is described and the chapter will end with an overview of the resulting model and its characteristics. In section 8.1, the TMM definition process is described. Consequently, the influence of the lumped parameter method on the results of the thermal analysis is verified in section 8.2.

8.1. Building the TMM of the CORE Hinge

The purpose of the TMM is to convert a nodal network into the temperature of every part, according to the node characteristics, thermal couplings and heat inputs, that are determined by the GMM. To calculate the temperature of all nodes after a certain time step, the procedure described in subsection 6.2.2 is used. In this section, the process of defining the thermal model of the CORE hinge is described. It is divided into two subsections. In subsection 8.1.1, the creation of the CORE hinge TMM is treated and in subsection 8.1.2, a short description is given of how the thermal model is run.

8.1.1. CORE Hinge TMM Creation

If a thermal model is created in Workbench, the geometric model results and the other thermal model inputs (conductive interfaces, initial conditions and boundary conditions) are used to create a so called analysis file. The function of this file is to translate the defined thermal model from Workbench into a programming file that can be read and followed by ESATAN. It defines both the inputs to the thermal analysis, as well as the analysis methodology.

In the non-standard methods described in section 6.3.1, the analysis file is not generated by Workbench, but is defined from scratch by the user. However, for the DST CORE hinge model, it is possible to use the geometric model that has already been made and described in chapter 7 to create a baseline analysis file. The contents of this file can then be adapted to create the thermal model of the CORE hinge. This baseline file can be created by defining and applying the analysis case, in which the boundary conditions, initial conditions, solution control and output calls are determined. It is not necessary to actually perform an analysis; setting up the analysis case is sufficient. This approach has the advantage that the structure of the thermal model will be error free, which will make it much easier to identify errors and debug the thermal model without problems.

Creating the TMM Baseline

Defining an analysis case is done in the Thermal module of ESATAN by defining the following:

- **General** Here, the analysis case is named and the solver is defined. For most cases this will be ESATAN, but also SINDA/G can be selected.

- **Radiative Data** The radiative input is selected here. Furthermore, it can be decided whether a single radiative case, i.e. one orbit, a chain of different radiative cases, or multiple radiative cases, i.e. multiple orbits, are analysed. For the CORE hinge baseline, the results from the CORE hinge radiative case described in chapter 7 are selected, but they will be removed from the baseline for the actual TMM creation.
- **Boundary Conditions** Boundary conditions are to be defined in the define module, where the geometries are also defined. After their definition, they appear in the boundary condition list in the analysis case definition window.
- **Control Logic** This includes the initial conditions, solution control and the output calls. The initial conditions can be defined in the same way as the boundary conditions, but they can also be defined in the nodal definition. In the solution control, the solution method is defined by selecting one of the pre-defined mathematical solving algorithms. Furthermore, all parameters relevant to the analysis are defined such as the time interval, final time and maximum amount of iterations. In the output calls, the form in which the outputs shall be given is defined. Examples of this are an output file, a csv or excel spreadsheet. Furthermore, it can be defined which parameters should be output and for which nodes.
- **Model Files** Here, the working directory is chosen and the files that are necessary for the analysis are selected. Examples of the latter are libraries, user files or global files.

For the CORE hinge baseline, no initial conditions and radiative data have been selected. Two temperature boundary conditions are defined, one for the connection between the CORE hinge and the spider and one for the connection with the boom. For the analysis, the SLCRNC solver was selected. This is a transient solver, that is based on the Crank-Nicolson method, which is an implicit forward-backward differencing method. Finally, it has been decided to request the outputs in an output file, which can easily be displayed in Notepad++, and a Thermal Model Data (TMD) file, which can be displayed in ThermNV. ThermNV is a graphical post-processing program that is included in the ESATAN package.

The TMM baseline file consists of the following parts.

- **Locals** This is where the bulk and optical properties are defined, as well as other constants that are used later in the file.
- **Nodes** Here, all nodes are defined. These are obtained from the geometric model of the CORE hinge.
- **Conductors** This is where the thermal couplings between nodes are defined. These are also obtained from the geometric model of the CORE hinge.
- **Initial** The initial and boundary conditions are defined here.
- **Execution** This is where the solution control is defined. This includes the solver and the analysis parameters.
- **Outputs** The output calls are defined here.

When the baseline file has been created, its contents can be adapted to represent the wanted thermal model. This process is described next.

Adapting the TMM Baseline

As explained in subsection 6.3.2, the solid and surface nodes of the geometric model will be combined into one diffusion node. A diffusion node is just a node for which the temperature will be calculated during the thermal analysis. As an example, another node type is the boundary node, which will always have the same temperature. This temperature is defined in the analysis file. The first step in the adaption process is to perform this combination.


In table 8.1, an overview of the transformation process is given for the middle strip component of the CORE hinge. This process is straightforward. As can be seen in figure 8.1, for solid geometries, every node definition is divided into three lines. The first and third line are the same for every node, and contain the node number, name and initial temperature and the position of the node centre, respectively. The second line of the solid

```

D5 = 'cam01_1', T = 0.0,
C = 4.987424E-007 * Cp_Ti * Dens_Ti,
FX = -0.0177766, FY = -0.00250000, FZ = 0.0270280;

D6 = 'cam01_1', T = 0.0,
A = 0.000102, ALP = 0.900000, EPS = 0.990000,
FX = 0.0192328, FY = -0.00250000, FZ = 0.0292421;

```



```

D5 = 'cam01_1', T = 0.0,
C = 4.987424E-007 * Cp_Ti * Dens_Ti,
A = 0.002352, ALP = 0.900000, EPS = 0.990000,
FX = -0.0177766, FY = -0.00250000, FZ = 0.0270280;

```

Figure 8.1: Illustration of the Node Combination

nodes, like node D5, contains the heat capacity of the node. Finally, the surface nodes' second line contains the surface area and the optical properties of the surface, like in node D6.

The nodes are combined by adding the second line of a surface node to the definition of the solid node, between the second and third lines. Then, the surface area of all surface nodes are added together. This is repeated for every diffusion node in the thermal model. The result for one of the nodes is shown in figure 8.1.

Table 8.1: Node transformation for the middle strip geometries. As geometry Strip_mid is divided into four parts, it consists of four nodes

Geometry Name	# Thermal	# Geometric	
	Diffusion	Solid	Surface
Strip_mid (1)	D79	D481	D485, D489, D493, D497, D501
Strip_mid (2)	D80	D482	D486, D490, D494, D498
Strip_mid (3)	D81	D483	D487, D491, D495, D499
Strip_mid (4)	D82	D484	D488, D492, D496, D500, D502
Strip_mid_curve	D83	D503	D504-D509
Strip_mid_curve2	D84	D510	D511-D516
Strip_mid_final	D85	D517	D518-D523
Strip_mid_block	D86	D524	D525-D530

In the second step of the baseline adaptation, a QI input is added to every node definition, which will be the total flux incident on each node. This, in turn, will be the summation of all fluxes on every surface nodes of a diffusion node. This QI is added to the first line, after the initial temperature definition. The process of calculating and adding the fluxes together is described in subsection 9.1.2.

The third step, combining the radiative thermal couplings, is the most labour intensive step, because of the high amount of thermal couplings in the model. The description of a thermal coupling in the analysis file is indicated by $GR(i,j) = \text{value}$. Here, GR indicates that the coupling in question is a radiative coupling and the arguments behind it are the radiating and the receiving nodes, respectively. For every radiative coupling, the node numbers are changed to their equivalent in the thermal model, according to the transformation of which an example is shown in table 8.1. When this is done, many couplings occur multiple times. These duplicates are added together to get the thermal couplings for the thermal model. This can be done in a fast way by copying all entries to an excel file, after which a pivot table is used to perform the additions. The approach is based on the notion that, for both the sending and the receiving diffusion nodes, the radiative couplings of all surfaces added together is equal to the radiative coupling of the corresponding diffusion node.

The notion can be explained as follows. Firstly, the temperature of all surface nodes is equal, as the surface nodes are converted into one node. Furthermore, radiative heat transfer is directly proportional to the GR, which, in turn, is directly proportional to the view factor times the area of a face. Because of the fact that the temperature of all nodes are equal, adding the thermal couplings of the surfaces together is the same as adding the heat radiated from all surfaces together. This, in turn, is equal to the combined radiative heat loss. Adding the thermal couplings together thus results in the total heat lost of the diffusion node.

Secondly, as the radiative heat transfer from node i to j only depends on the surface area of the sending node

i, the same goes for adding together the radiative couplings of all receiving surface nodes to get the coupling for the resulting diffusion node.

After the radiative couplings are transformed, some conductive thermal couplings needed to be altered or added because of the following reasons. First, ESATAN is unable to identify conductive interfaces between round surfaces. Therefore, it was not possible to generate a contact conductance where the cam halves roll over each other. This thus had to be calculated by hand. The hand calculation process is described in the next paragraph. Another conductive coupling that had to be calculated by hand is the connection between the plate and the lower cam. As the plate geometries have been cut, ESATAN is not able to find an interface between them and the lower cam. Instead, the thermal coupling was calculated by hand.

Second, because of the limited types of geometries in Workbench, some of the fused interfaces in the top of the upper cam are not fully accurate. Because of limits of compatibility between curved and flat surfaces, the interface determined by Workbench is shorter than in reality. Therefore, these thermal couplings had to be increased in value. This is illustrated in figure 8.2, where the yellow lines are identified interfaces and the red line is the actual interface between the nodes. The multiplication factors can be calculated by dividing the accurate interface length by that determined by ESATAN, which is around two in the example.

Finally, as the pretension bolts are omitted from the geometric model, the resulting conductive couplings within the pretension structure were added manually.

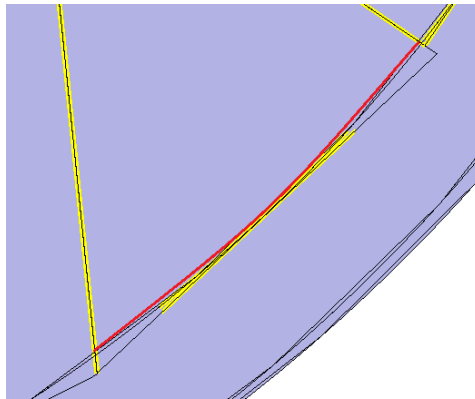


Figure 8.2: Illustration of the shorter interface identified by Workbench (yellow) and the actual interface (red)

In order to calculate the conductive heat transfer between nodes by hand, equation 8.1 is used [26].

$$GL(i, j) = \frac{kL}{A} \quad (8.1)$$

In this equation, $GL(i, j)$ is the conductive coupling between node i and j , k is the thermal conductivity, L is the distance between the nodes and A is the surface area of contact. As the nodes are not placed in a rectangular grid, the distance between nodes is calculated by adding the two distances between the node centres and the middle of the conductive interface together.

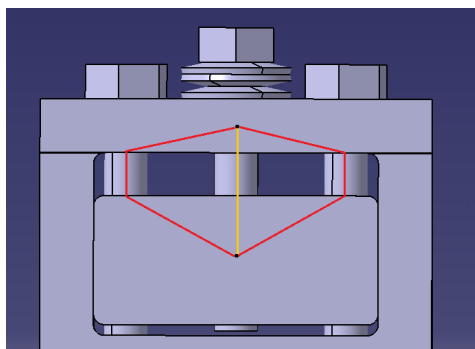


Figure 8.3: Illustration of the conduction paths in preload structure

For two of the hand calculated conductive couplings, the calculation process is not straightforward. These are the contact between the cams and the interfaces in the pretension structure. For the contact between the cams, the conductive coupling not only depends on the distance between the node centres, but also on the contact conductance. This conductance is dependent on, among others, surface roughness and contact pressure. Using Hertzian contact mechanics, the contact surface area can be calculated, with which the conductance without the contact conductance is determined. This is done using equation 8.2 [3]. This equation calculates the half-width b of the contact area of two coaxial cylinders, as displayed in figure 8.4.

$$b = \sqrt{\frac{2PR}{\pi E^*}} \quad (8.2)$$

In this equation, P is the pretension force, R is the reduced radius of curvature and E^* is the contact modulus. The latter two are determined using equations 8.3 and 8.4, respectively. Here, R_i is the radius of curvature of the cylinders (or the cams in the CORE hinge), E_i is the Young's modulus of the cylinder and ν_i is the poisson ratio.

$$\frac{1}{R} = \frac{1}{R_1} + \frac{1}{R_2} \quad (8.3) \quad \frac{1}{E^*} = \frac{1 - \nu_1^2}{E_1} + \frac{1 - \nu_2^2}{E_2} \quad (8.4)$$

Including the contact conductance in the calculation leads to a lower conductance, as it acts as a barrier for conductive heat flow. It has been determined that the thermal coupling calculated using equation 8.1 is very small when compared to the other conductive couplings in the model (only one to five percent). Therefore, it has been concluded that the influence of adding the contact conductance, which lowers the thermal coupling, is negligible. Therefore, the conductive thermal coupling for this interface has been calculated as if the interface were fused.

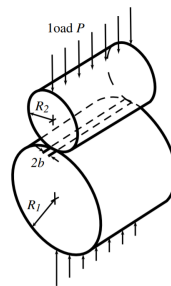


Figure 8.4: Illustration of the contact area due to load P

The bolted connections for the couplings in the pretension structure act as the conductive interface between the holder and the pretension block. As can be seen in figure 8.3, there are three, symmetrically placed bolts, the middle one of which does not reach the pretension bottom. Therefore, there are three and two conductive paths, for the top and the bottom, respectively. In order to calculate the total thermal coupling, the couplings from the different load paths have to be added together. The three conductive paths from the preload top to the preload block are shown in figure 8.3. For the calculation of each contribution to the conductive coupling, the contact area in equation 8.1 is taken equal to the area of a bolt.

8.1.2. Running the Thermal Model

The easiest way of running the thermal model of the CORE Hinge is to run it in Workbench. In order to do this, a new project is made in Workbench, which will only include an analysis case (thus no geometries or radiative case). In this analysis case, it is not necessary to define radiative data, boundary conditions or a control logic, as those are already defined in the analysis file. The only information that is relevant for Workbench are the working directory, where the output files and the files necessary for the analysis are saved, and the analysis file. It is handy if the analysis file is saved in the working directory, but this is not strictly necessary. Once the analysis case has been applied, it can be run via Workbench.

8.2. Influence of Lumped Parameter Method on Results

In section 6.1, the expectation was mentioned that a lumped parameter model of the DST CORE hinge will be accurate enough for the goal of this thesis, in spite of the loss of information that comes with discretised models. Whether this is true, is determined by a sensitivity analysis, which is described in this section. In subsection 8.2.1, the method of this verification is described, after which the results are described in subsection 8.2.2.

8.2.1. The Method

In order to test the hypothesis, it has been decided to compare the results of two thermal models. The first model is the model described in the previous section and chapter 7. This model will be referred to as the base model. The second model is based on that model, with the only difference that in this model, every node of the first model is divided into multiple nodes. Therefore, this model consists of more nodes, which leads to a more accurate determination of the temperature distribution of the CORE hinge. This model will be referred to as detailed model.

When more and more nodes are included in a model, the distance between nodes approaches zero, converging to a continuous model, which provides the temperature at every location on the hinge. In the detailed model, the larger amount of nodes will serve to approximate a continuous model. It has been decided to divide every node into three nodes, as a model with many more nodes would make the modelling and analysis time consuming. As most geometries are much longer in one direction than in the other two, this is easy for most geometries. The other geometries are divided into 9 or 27 nodes. Because of these geometries, the detailed model contains 3.9 times as much nodes as the base model. Note that in both models, the non-CORE hinge geometries have been omitted, as these make the model only more difficult and do not add much to the goal of this sensitivity analysis.

It is expected that adding more nodes will have an increasingly smaller influence on the results. Therefore, this amount of nodes gives a reasonable insight in the influence of the lumped parameter selection on the results of the analysis.

The results of both models are compared to each other to determine the influence of the lumped parameter method on the results. For this, it is important to consider the definition of the nodal temperature in a lumped parameter model. As explained in section 6.1, the temperature of a node is not the average temperature over the node, but is the temperature that the component would have at the node centre location. This means that the temperature has to be compared at the same location to compare the results of both models. As most nodes will be divided into 3 nodes per direction, this is quite simple, as the middle node centre in the second model corresponds to the node centre of the original node. For those nodes that are divided into an even number of nodes, the average of the two centre nodes is used.

8.2.2. Results

In order to see the difference between the less detailed and more detailed model, the temperatures for every geometry are determined for two different time steps. For this, the first ($t = 567s$), and the final ($t = 5674s$) time steps are selected, as this will provide understanding of the influence over time. It is expected that the differences at the final time step are bigger, because the difference will have had more time to accumulate.

Table 8.2: Minimum, average and maximum difference in temperature between the two models at time $t = 567$. The differences are calculated with respect to the temperature difference between the hottest and coldest nodes ($= 100 K$). Thus, one percent is equivalent to 1 K

Component	Minimum (%)	Average (%)	Maximum (%)
Lower Cam	0.05	0.79	1.45
Upper Cam	0.03	0.44	1.01
Strip Left	0.01	0.81	1.48
Strip Right	0.15	1.35	2.56
Strip Middle	0.08	0.44	1.15

The minimum, maximum and average procentual differences are given in table 8.2, for the five different components of the CORE hinge. In table 8.3, the same is done for the final time step. Note that for both time steps, one percent equals around 1K difference. As can be seen in the tables, the component with the highest average temperature difference between the two models is the right strip. For this strip, the maximum difference is 3.06 %, which is still a small deviation. For all other components, the average difference is smaller than 1.5 %, even for the final time step. Additionally, for most nodes, the difference is smaller than 2.5 % in both time steps. The amount of nodes with a difference higher than 2.5 % is one in the first and five in the final time step (1.1 % and 5.5 %, respectively).

The fact that the difference between the models is no more than a few percent, even for the time step with the biggest expected difference, leads to the conclusion that the influence of making the nodes smaller is rather small and within the expected accuracy. Therefore, using the lumped parameter method will only have a minor influence on the results of the thermal analysis. The assumption that the thermal model, using the lumped parameter method, is accurate enough is therefore valid. However, if it would turn out that a higher accuracy of the results is necessary, it is good to keep in mind that the method is not perfect.

Table 8.3: Minimum, average and maximum difference in temperature between the two models at time $t = 5674$. The differences are calculated with respect to the temperature difference between the hottest and coldest nodes ($= 101.8$ K). Thus, one percent is equivalent to 1.02 K

Component	Minimum (%)	Average (%)	Maximum (%)
Lower Cam	0.11	0.92	2.16
Upper Cam	0.04	1.31	2.80
Strip Left	0.20	0.70	1.08
Strip Right	0.61	1.84	3.06
Strip Middle	0.08	0.84	1.90

Next to the major conclusion stated above, some other observations have been made. Firstly, the results of the right strip show a much larger deviation than those of the left strip, especially for the second time step. It is theorised that the lumped parameter method shows a larger deviation for places that have a lot of incident radiation, as in the model, the right strip is on the sun side of the hinge and the left strip is on the shadow side. This is not surprising, as the local presence of radiation increases temperature differences, due to which temperature extremes can arise.

As most of the CORE hinge is blocked from solar radiation, which is by far the biggest radiation source, this has no major influence on the results of the model. The fact that the radiation has such an effect in this sensitivity analysis is caused by the absence of the baffle geometries.

Secondly, even though the time between the two selected time steps is large, the average difference at this time step is only 2 times as large as the first step (0.64 % versus 1.12 %). It can even be seen that the difference for the left strip is smaller at the final step. This indicates that the accumulation effect of the temperature difference over time is not as important as expected. Instead, the presence of radiation seems to be much more important. This is especially true after comparing the results at intermediate time steps, the results of which differ over time. For the time step $t = 2270$ s, for instance, the procentual differences are smaller than for the first time step. This has one exception, however, which is the fact that not the right strip, but the left strip is less accurately calculated. As indicated by the previous point, the most probable cause of this is the fact that the solar direction is coming from the opposite direction due to which the left strip receives more (solar) radiation and the right strip receives less.

9

Thermal Analysis and Results

In the previous chapter, the process of building the thermal model of the DST CORE hinge has been described. In this chapter, the thermal analysis that has been performed with this model is described. Several things have to be noted. In section 9.1, the method of the thermal analysis is described. In section 9.2, the results of the analysis are highlighted. Finally, in section 9.3, a discussion is conducted of the results of the thermal analysis.

9.1. Method of the Analysis

Because of the length of an orbit, and the fact that the changes in temperature that the hinge will experience during the orbit are slow for the most part of the orbit, the thermal loads will only be determined during those phases of the orbit during which the temperatures changes fastest. During the modelling process, especially the creation of the radiative cases for the geometric model, it has become clear that there are two phases during which this is the case. These are the minutes before the start of the eclipse and after the end of the eclipse. This can be explained as follows. First, the temperatures in the hinge change fastest when the radiation that the hinge receives is biggest. During eclipse, the only relevant radiation is the infra-red radiation that is received from the Earth. On the day side, the baffle blocks the radiation coming from the Sun, as the telescope will always be pointed at the Earth. However, closer to the night side of the orbit, the telescope is pointed more and more perpendicular to the Sun-Earth axis, after which the telescope is pointed slightly in the direction of the Sun. Due to this, some solar radiation will actually hit the CORE hinge, as the baffle no longer protects the hinge from the radiation. It is here that the temperature of the CORE hinge will quickly rise, which leads to thermal strain and loads. This is illustrated in figure 9.1. In this figure, two situations are displayed. At the left is the DST at the middle of the day side of the orbit, in which the solar rays hit the bottom of the baffle. This thus heats up, which is displayed by the red line next to it. The DST at the top is where it goes into eclipse. Here, it can clearly be seen that the solar rays pass by the baffle and hit the top of the SMSS, which is made possible by the attitude of the DST with respect to the Sun.

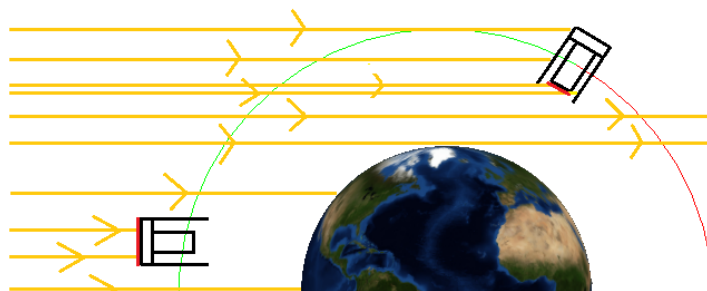


Figure 9.1: Illustration of the solar radiation that hits the DST at two places along the orbit (mid-day and near eclipse)

9.1.1. Hinge of Interest

Not all four hinges will receive the same amount of solar radiation. This depends on the attitude of the telescope with respect to the sun and is illustrated in figure 9.2, where the sunlight comes from the direction of the viewer. The hinge that is closest to the sun (hinge 1) will receive the smallest amount of radiation, as this hinge has the most protection from the baffle. The hinge that is furthest away from the sun (hinge 2) will not necessarily receive the highest amount of radiation, as the spider will block part of the radiation. If the telescope is rotated by several degrees, hinge 2 will have more clearance from the spider and the side of the hinge will receive more radiation. This case is considered to be a worst-case scenario. Therefore, it will be used for the analysis, where the DST is rotated by 20 degrees clockwise.

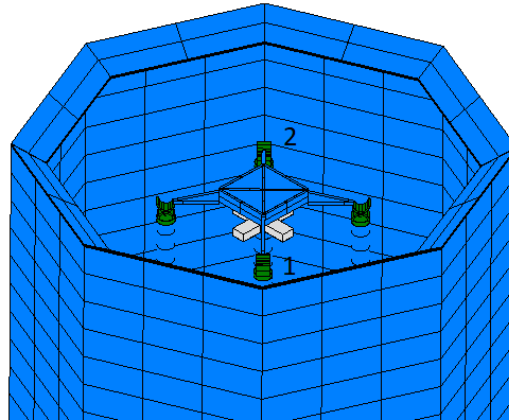


Figure 9.2: The SMSS as seen from the direction of light, with furthest and closest hinges numbered

9.1.2. Input

The thermal analysis that will be performed for the two phases where the temperatures in the hinge change fastest, is done as follows. First, the geometric model of the CORE hinge is used to determine the radiation that every node receives. These results are determined for every four degrees of the orbit, for a total of 40 degrees per phase. This amounts to a total time difference of 630 seconds, and a time difference of 63 seconds between every position. The entry and exit phases start at 60 and 260 degrees, respectively.

For each position, the solar, albedo and planet infra-red radiation per node will be added, and the resulting total radiation, or total flux, of each geometry are added to get the total radiation per thermal model node. Excel is used for these additions; the radiation results from the radiative case are output to a .csv file, which can be imported into excel. This leads to an excel file with the total received radiation per node per position along the orbit, which will be used in a later stage.

Initial Conditions

The other input that is needed is the initial temperature of all nodes. Normally, a steady-state analysis is performed to get the initial temperatures for the transient analysis. In this analysis, another approach is taken, as the analysis is focused on the near-eclipse parts of the orbit. In this analysis, a model of the DST is used to obtain the initial temperatures of the CORE hinge model. This DST model is used in the standard way, where the initial values are determined via a steady state analysis. Afterwards, a transient analysis is used to determine the temperatures of the CORE hinge nodes at the start of the period of interest. As the DST is a more accurate description of the whole DST than the geometric model - including non-CORE hinge geometries - described in section 7.4, the DST model will be used to determine the initial temperatures for the analysis, as well as the temperatures of the boundaries over the whole phase.

For this model, the radiative case runs from -20 degrees to 260 degrees. Here, the solar, albedo and Earth IR radiation are determined for every 40 degrees of the orbit. This includes the whole eclipse exit phase, as the temperature of the non-CORE hinge components of the DST, which are included as boundary nodes in the model, will rise during this part of the orbit. To incorporate this in the model, the average temperature of the boundaries is used. Finally, it has to be noted that for the exit phase, the temperatures of the hinge that is opposite to the hinge that is used for the entry phase will be used. This is done because in the exit phase the opposite hinge will have more radiation with respect to the entry phase.

Component	Nodes	Temp. (K)
Lower Cam	D3-D29	8.70
Side Strips	D30-D43	8.76 / 9.26
Upper Cam Top	D44-D61	9.20
Upper Cam Bottom	D62-D74	9.33
Upper Cam Other	D75-D78	8.96
Middle Strip	D79-D86	8.70 -> 9.26

Table 9.1: Initial conditions for the entry phase

Component	Nodes	Temp. (K)
Lower Cam	D3-D29	-0.13 / 0.66
Side Strips	D30-D43	-1.94 / 0.75
Upper Cam Top	D44-D61	-1.5 / -1.88
Upper Cam Bottom	D62-D74	-1.4
Upper Cam Other	D75-D78	-2.86
Middle Strip	D79-D86	-1.94 -> -0.13

Table 9.2: Initial conditions for the exit phase

In table 9.1 and 9.2, the initial temperatures of the CORE hinge model are displayed for both the entry and exit phases, respectively. Note that nodes one and two, corresponding to the plate geometry, are not mentioned, as they are part of the boundary conditions. Because of the limited accuracy of the CORE hinge in the DST model, several components receive one temperature. Other components receive two different temperatures, as part of the component might have a substantially different temperature from the remainder. Finally, the temperatures for the nodes of the middle strip are assigned a range of temperatures, which are determined from the temperature of the node they are connected to. In the tables, Upper Cam Other refers to the straight upper cam components and the spider block.

Boundary Conditions

In the DST, the CORE hinge is connected to the spider and the boom. As those components are not included in the thermal model, three boundary conditions are included in the model, to simulate the connection between the CORE hinge and the rest of the DST. Three boundary conditions, and not two, as the plate is divided into two nodes in the model. These boundary conditions apply to the two plate nodes and the spider connection node and are equal to the temperatures of the geometries as determined in the DST thermal model. The spider connection node is part of the non-CORE hinge nodes and is connected to the spider block. For the entry and exit phase, respectively, the values of these boundary conditions are given in tables 9.3 and 9.4 for the initial, middle and final time steps.

Table 9.3: Boundary Conditions for the entry phase

Component	Node	t = 0 (K)	t = 315 (K)	t = 630 (K)
Plate	D1/D2	8.48	8.30	19.00
Spider Connect	D714	-0.23	5.00	28.00

Table 9.4: Boundary Conditions for the exit phase

Component	Node	t = 0 (K)	t = 315 (K)	t = 630 (K)
Plate	D1/D2	-6.18	-9.50	-3.80
Spider Connect	D714	-22.5	-14.00	25.20

9.1.3. The analysis

After the initial conditions and boundary conditions are put into the TMM, the thermal model of the CORE hinge is ready to be used for determining the temperature distribution of the CORE hinge for every 63 seconds of both the entry and exit phases. In this subsection, a short description is given of the way that the thermal analysis is carried out.

As described in the previous subsection, for the two phases, the total flux per node has been determined for every 4 degrees of the orbit. The first step of the analysis is to run the thermal model with the total flux from position one, with the end time being equal to 63 seconds and a time step of 6.3 seconds. This results in the temperatures at the second position. Afterwards, the initial temperatures are replaced with the final temperatures of the first position and the total flux of the second position is put in the model. Afterwards, the model is again run for 63 seconds, which leads to the temperatures at the third position. The same process is repeated for every position, which leads to the final temperature at 630 seconds. Next to the inputs and boundary conditions, the temperature of the boundary nodes, which correspond to the non-CORE hinge components of the DST, are changed for every time step.

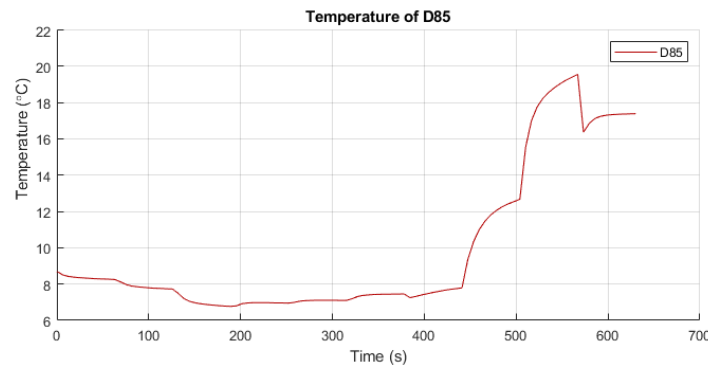


Figure 9.3: First result of the temperature of node D85 (part of the middle strip)

However, after applying the described steps, the temperature progression in between the positions shows strange behaviour. This can be seen in figure 9.3, which displays the temperature progression of node 85. Note that similar behaviour is present for all other nodes. Given the temperature difference between the start and end of a period, the temperature changes quickly at the beginning of a period, and flattens towards the end. Then, at the start of the next period, the temperature changes quickly again and flattens afterwards. Furthermore, in the final period, the temperature decreases quickly at first, but then increases towards the final temperature. It is very unlikely that the result shown in figure 9.3 is an accurate representation of the temperature progression of the node in real life. Instead, the results show that an analysis in which the inputs are not updated for every time-step does not work properly.

To solve this problem, the inputs could be updated for every 6.3 seconds, leading to linear temperature progression between each time-step. However, with this solution, it will take a much longer time to perform the analysis than with the current period of 63 seconds. This is caused by the way that the analysis is performed. For every time-step, the inputs have to be altered manually, which is time-consuming because not all inputs can be related to one corresponding node of the DST model and because errors can occur if it is performed too fast. However, with an interval of 63 seconds, the period in which the solar radiation hits the CORE hinge is captured over multiple positions, while the time spent on the analysis is kept to a reasonable level. It was decided to change the time step from 6.3 to 63 because of this. This leads to less accurate results for times between positions, but to more accurate results for every 63 seconds.

In the next section, the results of this analysis are highlighted.

9.2. Results

For both phases of the orbit, the temperatures of all nodes are known for eleven points in time, ranging from 0 to 630 seconds from the beginning of each phase. In this section, the most important results of the thermal analysis will be treated.

In all graphs in this section, the data points are indicated by dots, which are connected by dashed lines. These mean that the exact temperature progression between the dots is not known; they are solely included to make the temperature progression easier to see.

9.2.1. Entry Phase

During the entry phase, the telescope is in that part of the orbit in which more and more solar radiation is blocked by the Earth. Therefore, the average temperature of the telescope will decrease during this phase, while the temperature of the parts that are in sunlight is still increasing. As the CORE hinges are shielded from the sun by the baffle, their temperature will decrease. However, as explained in section 9.1, for part of this phase, the baffle will not protect the hinges from the solar radiation. Therefore, the peak temperature for the CORE hinges is expected to occur during this entry phase. The moment at which the solar radiation starts to hit the hinge is at time $t = 378s$.

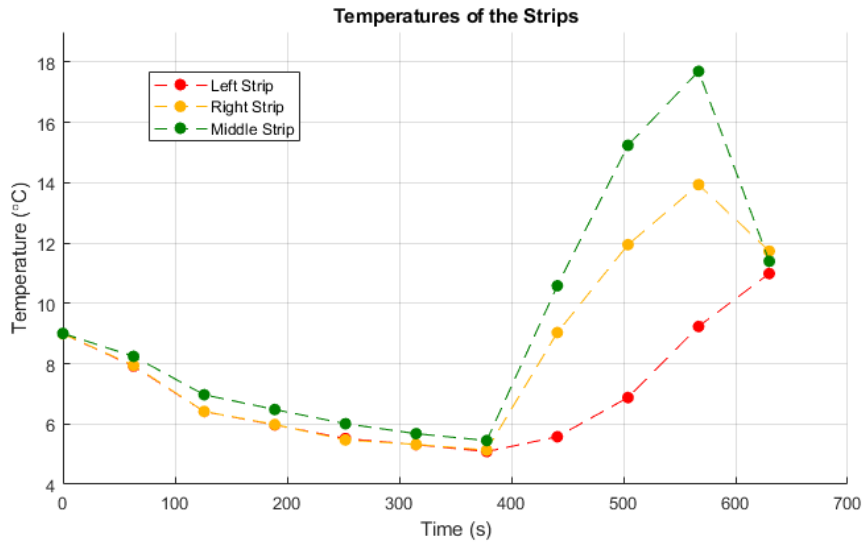


Figure 9.4: Average temperature progression of the three strips in the entry phase

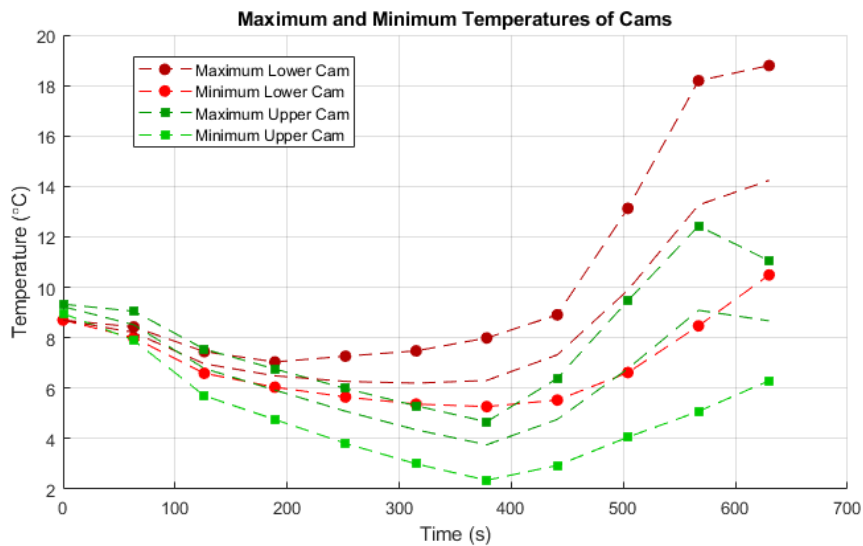


Figure 9.5: Maximum and minimum temperature progression for the lower and upper cams in the entry phase, including the average temperature as a dashed line, to allow an easy comparison to the strip temperatures.

In figures 9.4 and 9.5, the most important results of the entry phase are displayed. These are the average temperature of the three strips and the maximum and minimum temperatures of the two cams, respectively. The reason for only showing the average temperature of the strips, and not the maximum and minimum temperatures is the fact that the strips are only one node wide and the fact that the average temperature of the strips will determine the and shrinking of the strips, irrespective of the minimum and maximum temperature. For

the cams, the geometry is more complex and the influence of the temperature distribution on the mechanical behaviour of the hinge is thus bigger. Therefore, the maximum and minimum temperatures of the cams are shown. In appendix A, additional figures are present in which the temperature progression of the strips is displayed for every node. Furthermore, a figure is included in which the minimum and maximum temperatures of the upper cam are divided into three parts: the base, the top and the pretension components. For the exit phase results, similar graphs will be displayed.

In the entry phase figures, it can be seen that the average temperature of the strips and upper cam are very similar and decreasing while no sunlight reaches the CORE hinge. The decrease in temperature is however flattening, which is probably caused by sunlight that starts to reflect off the inside of the baffle and the spider. What is most interesting here is the fact that the lower cam stops to cool down before the upper cam does, which can be seen in both the maximum, average and minimum temperatures. Stronger, there is at least one node in the lower cam which starts to heat up almost 200s before the strips do, which is reflected in the maximum temperature line. The opposite was expected as the upper cam is on top of the lower cam and because the upper cam is connected to the spider, which has a higher temperature. The most logical explanation for this is that the lower cam receives more of the radiation that reflects off the inside of the baffle than the upper cam, causing it to heat up earlier.

After the initial phase, where the temperature of the hinge is decreasing, from time $t = 378$ s onwards, a fast spike in temperature can be seen at the strips, which coincides with the first moment in which solar radiation hits the CORE hinge. It can be seen that the temperature of the left strip heats up much slower than the other two strips, which is due to the sunlight being blocked by the spider. From the same time onwards, the cams also heat up, but this happens much slower than the heating of the strips. This is caused by the 50 times higher heat capacity of the cams, due to which it takes more time for them to heat up.

After time $t = 567$ s, the solar radiation is no longer present in the CORE hinge. This is also reflected in the temperatures of the hinge, as the temperature of the upper cam and the right and middle strips is decreasing. However, the temperature of the lower cam and left strip still increases.

This can be explained by the fact that it takes a while for the heat to dissipate. This dissipation happens first at the upper cam, as this cam has the most exposure to space. Because the lower cam mostly radiates to the bottom of the upper cam, the lower cam only starts to cool down when the upper cam has done so. This may explain why the left strip temperature still increases after time $t = 567$ s. It can be seen that at this point in time, the average temperature of the lower cam is higher than that of the left strip. This indicates that the higher temperature of the lower cam conducts more heat to the strip than the amount of heat that the strip loses because of radiation to the baffle and conduction to the cooler upper cam.

9.2.2. Exit Phase

During the exit phase, the telescope will leave the eclipse, and the average temperature of the telescope will start to rise. After 126 seconds, sunlight will start to hit the CORE hinges. In the exit phase, the lowest temperatures along the orbit of the DST are recorded, as the telescope will have had the most time to cool down at the end of the eclipse period. In figures 9.6 and 9.7, the most important results of the entry phase are displayed. Just like in the previous subsection, these include only the average temperature of the three strips and the maximum and minimum temperature of the two cams. Furthermore, similar additional figures are placed in Appendix A.

The results of the exit phase show similar behaviour as in the entry phase, but there are also several differences. First, the temperature of the right and middle strip will quickly increase when the sunlight hits the CORE hinge and the left strip does not, just like in the entry phase. However, in the exit phase, the temperature of the left strip starts to increase even later than in the entry phase. Second, the temperature of the strips starts to decrease quickly when the solar radiation no longer hits the hinge, but now this happens even faster than in the entry phase.

These two differences can be explained by the much lower temperature of the surrounding components. Due to this temperature difference, heat is lost much faster than in the entry phase. This is further supported by the fact that, while the middle strip is much warmer than the right strip at time $t = 252$ s, their temperatures are almost the same at time $t = 315$ s.

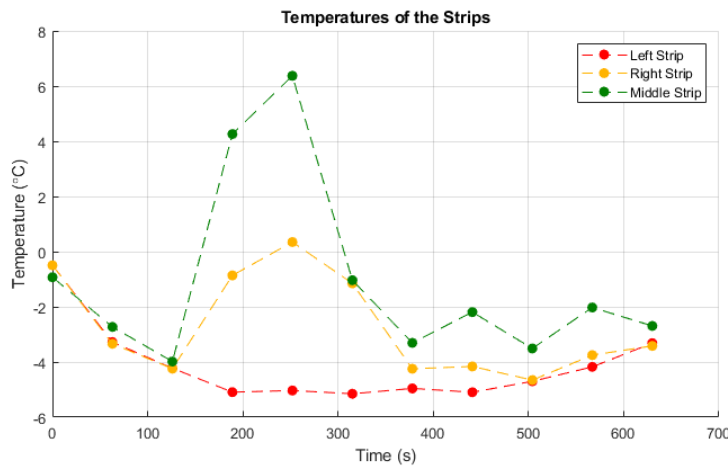


Figure 9.6: Average temperature progression of the three strips in the Exit phase

For the temperature progression of the cams, the first part is similar to that of the strips. First, the temperature of the cams decreases, after which, at time $t = 126$ s, the temperature starts to increase. However, only the maximum temperature in both cams and the average temperature in the upper cam increase substantially. The average temperature of the lower cam slightly increases for the first period, but decreases afterwards. This is probably due to a different attitude with respect to the sun than in the entry phase, which causes less solar radiation to reach the lower cam. The minimum temperature of the upper cam increases very lightly, which means that the coldest part of the upper cam is (almost) not reached by the solar radiation. This minimum temperature does increase more substantially later, but only when the whole telescope starts heating up as a result of it leaving the eclipse part of the orbit.

After point $t = 252$ s, the maximum temperature of the lower cam starts to decrease, while the upper cam keeps heating up. When considering the average temperature, the temperature rise is even almost non-existent and decreases one period before that. This means that less solar radiation hits the CORE hinge in this exit phase, as the lower cam receives almost no solar radiation in this phase. After point $t = 315$ s, the upper cam does cool down, which indicates that the upper cam is still in sunlight at $t = 268$ s, while the lower cam is not.

In the following periods, the temperature of both the lower and upper cams decrease quickly, but this decrease flattens out and at the end of the phase the cams start to heat up again. The same happens with the average temperature of the strips, as can be seen in figure 9.6. This is caused by the solar radiation that hits the baffle. Due to the sunlight only hitting the baffle and not the CORE hinge and SMSS, it takes some time for the heated up baffle to radiate its gained heat to the components inside of it.

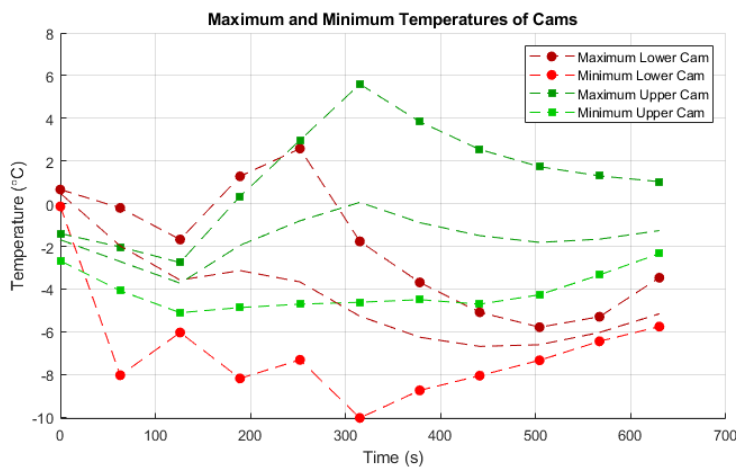


Figure 9.7: Maximum and minimum temperature progression for the lower and upper cams in the exit phase, including the average temperature as a dashed line, to allow an easy comparison to the strip temperatures.

The final interesting result in the exit phase is the behaviour which occurs in the middle strip from time $t = 368$ s onwards and in the minimum temperature of the lower cam until time $t = 315$ s. Here, the temperature does not decrease or increase continuously, but the temperature goes up and down. This behaviour does not occur at one or two nodes, but is a wider-spread phenomenon within the results. Furthermore, it does not occur as explicit in the entry phase.

The main cause of this behaviour is the following. Because of the relatively big time step of 63 seconds, the temperature differences between nodes, which lead to radiation and conduction between those nodes, are only determined once every 63 seconds. Therefore, if at the start of a period, a node has a higher temperature than its neighbours, it will cool down at a constant rate for the full 63 seconds. Even if the temperature decreases to values lower than the temperature of the surrounding nodes, the temperature will continue to drop until the next period is reached. For that following period, the temperature of the node at the start is lower than its surroundings and thus it will heat up with a constant rate for 63 seconds, leading to a higher temperature, etc. The extent of the behaviour is dependent on the amount of connections to other nodes and the amount of external heat a node receives; the less nodes a node is connected to, and the lower the external heat that a node receives, the bigger the influence of this behaviour on the results.

9.2.3. Conclusions for the mechanical analysis

In the thermal analysis, two phases of the orbit were analysed which were expected to show the biggest temperature differences in the DST CORE hinge. This was done as these are the most unfavourable conditions for the stability of the hinges and therefore serve as a worst-case scenario. As it turns out, the biggest temperature differences and the highest overall temperature of the CORE hinge occur during the entry phase of the orbit. Therefore, this is the most interesting phase to perform a mechanical analysis of, and thus, the results of this phase will be used in the mechanical analysis described in chapter 10.

9.3. Discussion of the Results

Although the thermal analysis has led to interesting and valuable results, several improvements have been identified for the analysis to make the results more accurate. These are described in this section.

The first improvement has to do with the input data. In the current analysis, the input, such as the incident flux per node, is updated every 63 seconds. The values of the incident flux are calculated at the beginning and end of each period, after which the average value is used as input. This has two implications.

First, as the inputs are constant for every 63 seconds, changes that occur in real-life are not represented in the results. In real-life, the temperature of the boundary conditions will constantly change, but in the model, they are assigned a constant value for every period. This causes the results to be different from the real-life behaviour. Second, the value of the flux is dependent on the moment in time at which the flux is determined. This can be seen, for instance, at the maximum temperature of the upper and lower cams in the exit phase in figure 9.7. According to the results, the heating up of the upper cam lasts 63 seconds longer than that of the lower cam. This would implicate that the upper cam is in sunlight for 63 seconds longer than the lower cam. However, this is probably only a few seconds in reality. What happens here is the following. At the moment that the incident solar flux is determined, the sunlight has just left the lower cam, but is only just hitting the upper cam. The result of this is that the upper cam has a high value of incident flux, while the lower cam has a low value. Therefore, the upper cam heats up for another 63 seconds, while the lower cam cools down.

To (partly) solve the issue above, the input specification could be done more often than the current 10 times, for instance every 6.3 seconds. The determination period would then have a much lower influence on the results, as the difference in the inputs would be reflected in the result for a shorter time. Additionally, increasing the amount of input specification points leads to more detailed information on the progression of the temperature distribution of the CORE hinge, as the temperatures are given for smaller time steps than before. However, as stated at the end of subsection 9.1.3, this will increase the time spent on this analysis very quickly.

Another improvement that could be applied in the model has to do with the representation of the non-CORE hinge geometries in the geometric and thermal models. In the current method, the baffle is divided into eight boundary nodes. Each node corresponds to one geometry of the geometric model and thus to one of the eight sides of the baffle. This is chosen to limit the amount of nodes that the baffle consists of, as for every node, the temperature has to be determined from the results of the DST model and added manually every period. However, the temperature of a baffle side is not constant. The difference between the maximum and

minimum temperatures of a side can be as large as several tens of Kelvins. Additionally, not every point along the baffle has the same influence each node of the CORE hinge, as the view factors are different along the height and width. Due to this, it is not so easy to determine the equivalent nodal temperature for the baffle. Instead, each baffle side could be divided into multiple nodes, allowing for a more accurate temperature distribution along the baffle.

10

Mechanical Analysis

With the results from the thermal analysis, the inputs for the mechanical analysis can be calculated. This mechanical analysis is conducted to be able to determine the adherence of the CORE hinge to the stability of the secondary mirror and in-orbit drift requirements. In this chapter, the mechanical analysis is described, from the method and the mechanical model to the results. In section 10.1, a change of methodology is explained. Consequently, in section 10.2, the mechanical model is described and in section 10.3, the new method of the mechanical analysis is treated. In section 10.4, the results of the mechanical analysis are highlighted. Finally, in section 10.5, the results of the analysis are discussed.

10.1. Changing the method

The first idea for the thesis work was to spend a similar amount of time on both the thermal and on the thermo-mechanical analysis. However, during the thesis, it turned out that more time had to be spent on the thermal analysis to achieve useful results. This was deemed important, as a meaningful mechanical analysis cannot be performed if the thermal input is non-applicable and inaccurate.

By spending more time on the thermal analysis, however, less time is available for the thermo-mechanical analysis than anticipated. Considering this, it is best for the outcome of the thesis to apply several changes to the methodology of the mechanical analysis, including a different method for determining the inputs for this analysis. These changes are described in this section.

The following two method changes are considered to be the most effective in decreasing the time that is needed for the mechanical analysis, while keeping the results relevant.

The first method change is related to the way that the inputs to the mechanical model are determined from the thermal results. The stability of the CORE hinge will be mainly influenced by the expansion of the strips. As the strips are much bigger in the longitudinal direction as compared to the other two directions, the thermo-mechanical behaviour of the strips is not that difficult to predict; they will mostly expand in the longitudinal direction. Additionally, with some assumptions, the expansion and displacement of the cams can also be predicted. Therefore, it has been decided to not use thermo-mechanical analysis software, but to calculate the stresses and displacements within the CORE hinge by hand.

The notion that the strips are the main driver for the stability of the hinge is based on two reasons. Firstly, the strips will be affected the most by the incoming orbital fluxes, because of their relatively low mass and heat capacity. Secondly, because the length of the strips is three times as big as compared to the radius of the cams, their expansion due to temperature changes is much bigger than that of the cams.

The second change that is made to improve the efficiency of the mechanical analysis, is the level of detail of the mechanical model. Initially, it was decided to couple multiple interface models to get a detailed mechanical model of the CORE hinge. Instead, a less detailed model will be used, that is still expected to be able to give an insight in the behaviour of the hinge, but that only consist of the elements as shown in figure 3.4. A description of this model and its components is given in section 10.2.

10.2. Mechanical Model

According to the methodology that has been presented in section 5.3, a mechanical model has to be built before the mechanical analysis can be performed. In this section, the mechanical model of the CORE hinge is described. After a short description of the mechanical model, three subsections are included. In subsection 10.2.1, the link between the mechanical model and the CORE hinge is described. In subsection 10.2.2, the way that the stiffness of the springs and friction between the cams are modelled is explained. Finally, in subsection 10.2.3, the remainder of the inputs for the mechanical model are highlighted.

The mechanical model can be seen in figure 10.1. It is not fully representative for the real behaviour of the CORE hinge, as the only two degrees of freedom in the model are in the z-direction. Thus, the model is not able to predict displacement into the x and y directions. However, in the z-direction, it is able to identify the response of the CORE hinge to changing loads within the hinge.

There are two differences between the mechanical model of the CORE hinge and the model described in section 3.2.1. First, the spring constants around mass 2 in Lake's model are different, while they are equal in the CORE hinge model. Second, the friction element does not connect the wall to mass 2, but it connects the wall to mass 1. The displacement δ is then the resulting displacement of mass 1 under the influence of force F .

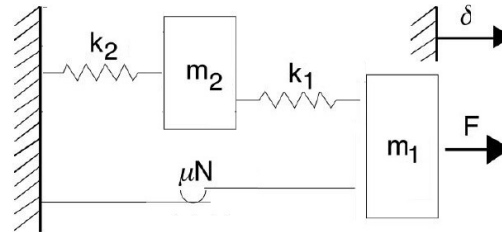


Figure 10.1: Illustration of the mechanical model

10.2.1. Representing the CORE Hinge

For the mechanical analysis, the lower cam is selected as the base with respect to which the displacements will be determined, as this part is connected to the boom and the upper cam will move with respect to the lower cam. This is represented by the fixed wall. The model further contains two masses. Mass 1, which represents the mass of the upper cam, and mass 2, which represents the mass of the strips. All three strips are lumped together in this one mass, as they are symmetrically placed between the hinges (The mid strip is twice as wide as the side strips). The connection that the strips form between the upper and lower cams is represented by spring k_1 and spring k_2 . The frictional element between m_1 and the wall represents the friction between the two cams if they roll over each other. Finally, force F represents the force that is exerted on the upper cam due to the preload and the expansion of the strips.

10.2.2. Modelling Stiffness and Friction

The strips in the CORE hinge are represented by a point mass that is connected to the upper cam by a spring with spring constant k_1 and connected to the lower cam by a spring with constant k_2 . In the model of the CORE hinge, the spring constants of both springs combined represent the spring constant of the strips. To calculate spring constants k_1 and k_2 from the equivalent spring constant of the three full strips, it can be used that, for springs in series, their spring constants can be added together, but only if they are equal to each other. Therefore, k_1 is taken as equal to k_2 . This leads to the following equations of motion:

$$m_1 \ddot{x}_1 = -k_1 x_1 + k_1 x_2 - N \operatorname{sgn}(\dot{x}_2) + F_a \quad (10.1)$$

$$m_2 \ddot{x}_2 = -(k_2 + k_1) x_2 + k_1 x_1 \quad (10.2)$$

In order to calculate the spring constant equivalent of the stiffness of the strips, equation 10.3 can be used.

$$k = \frac{EA}{L_{strip}} \quad (10.3)$$

Here, L is the total length of the strip in m, E is the modulus of elasticity in Pa and A is the cross-sectional area of the strip in m^2 . Due to temperature changes, however, the length, width and thickness of the strips will change. Therefore, the change in cross-sectional area will be bigger than the change in length. However, as temperature induced changes are very small, the spring constant is assumed to be constant for the temperature range of the strips.

The friction element, that represents the friction between the cams, is modelled using Coulomb friction. This means that the frictional element is proportional to the coefficient of kinetic friction and the normal force along the frictional interface, according to $F_{friction} = \mu_k \cdot N$. In the case of the CORE hinge, the normal force is equal to the applied preload.

10.2.3. Inputs to the model

Several inputs to the mechanical model are not known yet. In this subsection, a description will be given of how the inputs to the mechanical model are determined.

Spring Constant

The spring constant representative of the stiffness of the strips is calculated as follows. Using equation 10.3, the spring constant of all three strips is calculated. Then, as for springs in parallel, the equivalent spring constant is equal to the sum of springs, the individual values are added together to get the total spring constant. Because of the high modulus of elasticity of Titanium, this will lead to a high value. Each of the side strips has a constant of 35.6 MN/m, and the constant of the middle strip is equal to 62.4 MN/m.

However, these constants do not act in the axial direction, as the strips are fixed to the upper cam at an angle. By multiplying the spring constants of the strips by the sinus of the angle between the horizontal axis and the strips - 50° for the middle strip and 35° for the side strips - leads to a total equivalent spring constant of 60.1 MN/m.

Preload

In the detailed mechanical design of the SMSS, it has been determined that a preload has to be applied in the CORE hinge, to keep the cams from separating [18]. It has been determined during the mechanical testing phase that the cams are required to be pressed together by a 1kN force. This leads to a required preload force on the strips of 1388 N. This is equivalent to a normal force on the cam interface equal to 1000 N [39]. Due to the preload, the cams are in touch until the force that acts on the upper hinge via the middle strip exceeds the preload of 1388 N.

Friction force

As stated before, the friction force will be equal to $\mu_k N$, where μ_k is the kinetic coefficient of friction of Titanium, and N is the normal force that is exerted on the cams. The rolling resistance coefficient of steel on steel is 0.002 [34]. As the CORE hinge will be made out of Titanium Ti-6Al-4V, which has a slightly lower coefficient of friction than steel (0.3 [29] vs 0.42 [24]), the rolling resistance of the frictional contact in the CORE hinge will be taken as equal to 0.0015.

Force F Acting on the Upper Cam

This force F is the force that acts on the upper cam. It is equal to the z component of the preload force, which is 1000 N, minus the thermal load. As long as the thermal load is lower than the preload, the cams will be in contact and no problems occur. However, if the operation force exceeds the preload, the difference between them will excite mass 1 of the mechanical model. With the equations of motion, the response of the upper cam will be determined by considering the displacement δ .

10.3. Analysis Methodology

As stated in chapter 5, there are two different types of requirements for the M2 mechanism. With the mechanical model described before, it is possible to determine the lateral stability of the CORE hinge along the Z-axis.

This coincides with the most strict stability requirement and is thus the most interesting. As described in section 10.1, the input to the mechanical model will be determined by considering the expansion and shrinkage of the strips and the cam due to changes in temperature. However, this is not the only application of the thermo-mechanical results. With the expansion and shrinkage of the strips and the cams, it is possible to determine the in-orbit drift in the z direction, and around the x and y axes. Just like with the stability, these refer to the strictest requirements on the in-orbit drift. Therefore, the mechanical analysis will consist of two parts: the stability of the CORE hinge and the in-orbit drift of the CORE hinge. In this section, the method of the mechanical analysis is described. In subsection 10.3.1, the assumptions that are made for the analysis are given. In subsection 10.3.2, it way that the thermal loads are determined is highlighted. In subsection 10.3.3, the determination of the stability is treated, while in subsection 10.3.4, the determination of the in-orbit drift is treated.

10.3.1. Assumptions

For the mechanical analysis, the following assumptions have been made.

- The strips are assumed to be rigid and clamped at both sides
- The displacements within the CORE hinge due to the thermal behaviour of the hinge are in the micro scale. Therefore, the resulting rotations are very small as well. Because of this, it is assumed that despite the angular changes, the angle between the z-axis and the strips remains constant at 40 and 55 degrees for the mid strip and side strips, respectively
- The thermal progression of the cams is assumed to only influence the radius of the cams
- Rotations of the around different axes are assumed to be uncoupled

10.3.2. Determine the Thermal Loads

The main driver for the mechanical inputs is the expansion of the strips. For determining the thermal loads, the thermal results of the entry phase are used, as during this phase, the highest temperatures are reached. Because of the assumption that the strips are clamped at both sides, an equation can be derived to calculate the internal force due to thermal stresses. The basis for this derivation is the stress-strain relation: $\sigma = E\epsilon$. The thermal strain can be calculated using $\epsilon^T = \alpha_{th} \cdot \Delta T = \Delta L$, and for the stress: $\sigma = F/A$. These equations can be combined to get equation 10.4

$$E = \frac{F}{A} \cdot \frac{1}{\Delta L} \quad (10.4)$$

By multiplying both sides with $A\Delta L$ and rewriting the result, we get that $F = EA\Delta L$, which is, in turn, equal to $F = EA\alpha_{th}\Delta T = EA\alpha_{th} \cdot (T_i - T_0)$. This indicates that, as the modulus of elasticity of Titanium E, the cross-sectional area A, the coefficient of thermal expansion α_{th} and the temperature progression and thus T_i are known, the only unknown is the initial temperature. This temperature is the base temperature; the temperature at which the preload is applied. This temperature has not been specified yet, so this will be done now.

In order to minimise the friction in the hinge, the preload should not be too high. In the thermal analysis, the lowest average temperature of the middle strip, to which the preload is applied, is -4°C . Due to shrinkage of the strip, the tensile load, started by the preload, will increase if the temperature decreases. To have a maximum load in the middle strip to be no larger than four times the applied preload of 1388 N, the tensile load will be applied at a temperature of 5°C . This way, the load in the middle strip will not be higher than 5.56 kN, while the expansion of the strips is also kept in check.

Now, equation 10.4 can be used to calculate the thermal loads in the strips for the duration of the entry phase.

10.3.3. Determine the Stability

The mechanical model is used to determine the stability of the CORE hinge. The subject of the analysis, the entry phase, can be divided into two parts. In the first part, the thermal load is always smaller than the preload, and in the second part, the temperatures rise such that the thermal load exceeds the preload, leading to compressive stresses in the strips. The compressive force that is the result of this, is the force F in the equations of motion. In figure 10.2, the thermal loads over the course of the entry phase are shown in red. The black horizontal line indicates the preload and the green line indicates the resultant force F, that will be used

as input for the analysis. As can be seen in the figure, the preload force is exceeded between $t = 315$ s and $t = 378$ s, at $t = 348$ s. From this moment, the upper cam will be able to move. Therefore, the period between is the phase of interest and thus, the mechanical model will be run with the resultant force from $t = 348$ s to $t = 568$ s.

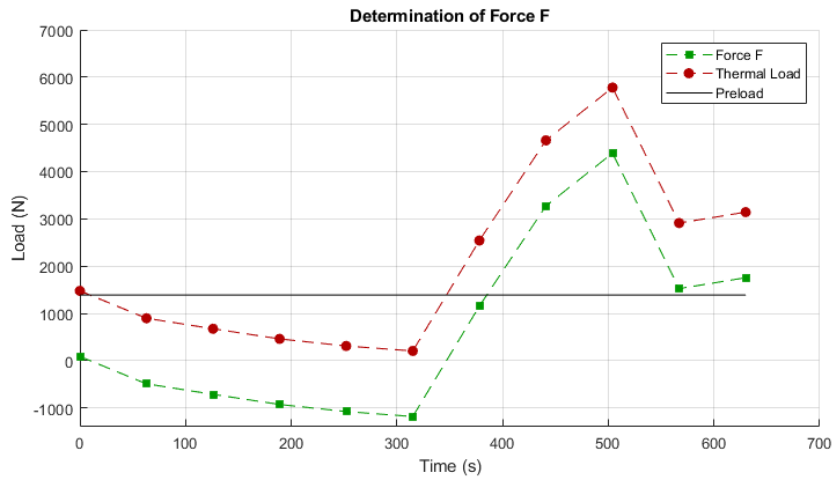


Figure 10.2: Three loads: preload, thermal load and resultant force

The results of the stability analysis are treated in subsection 10.4.

10.3.4. Determine the In-Orbit Drift

The thermal expansion of the cams and the strips will be used to determine the compliance of the CORE hinge with the in-orbit drift requirements. With these expansions, the lateral and angular displacement of the upper hinge with respect to the CORE plate are determined. The thermal expansion of the strips can be calculated by using the following equation: $\Delta L = \alpha L_0 \Delta T$, where L_0 is the initial length, α is the coefficient of thermal expansion, which, for Titanium, is equal to $8.9 \mu\text{m}/\text{K}$, and the temperature difference is equal to the average temperature of the strip minus the initial temperature of the strip.

The average temperature of a strip is calculated using equation 10.5, where n is the number of nodes that the strip consists of, L_i is the length of the node i and L_s is the total length of the strip. For the average temperature of the cams, the lengths L_i and L_s are replaced by the volumes of the nodes.

$$T_{avg} = \frac{\sum_{i=1}^n T_i \cdot L_i}{L_s} \quad (10.5)$$

From the expansion of the cams and the strips, the in-orbit drift behaviour is calculated as follows.

To determine the vertical displacement of the top of the CORE hinge, the increase in cam radius of both cams is calculated using the method described in the previous paragraph. Then, the result for both cams is added together to get the total displacement.

The expansion of the strips will be used to determine the angular displacement of the upper cam. This is done with the following two steps. First, the vertical expansion component of each strip is calculated, by multiplying the expansion ΔL by the cosine of the angle that the strip makes with the z-axis. This leads to three vertical displacements, one for each strip. These displacements are indicated by z_{mid} and z_{side} in figure 10.3. With the vertical displacements, the rotations around the x and y axes can be calculated for every position of the thermal results.

To calculate the rotation around the x-axis, the average vertical displacement of both side strips is used, together with the vertical displacement of the middle strip. These are indicated in figure 10.3. The rotation due to the extension of the strips is then calculated using equation 10.6.

$$\alpha = \tan^{-1} \left(\frac{|z_{side\,avg} - z_{mid}|}{\Delta y} \right) \quad (10.6)$$

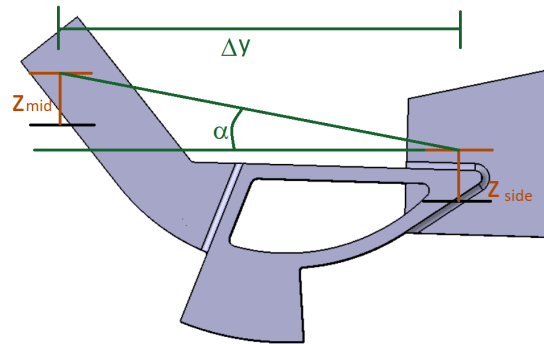


Figure 10.3: Illustration of the displacements and rotations of the upper cam

A similar procedure is followed for calculating the rotation around the y-axis. But this time, instead of the average vertical displacement of the side strips and the vertical displacement of the middle strip, the difference between the vertical displacement of both side strips will be divided by the horizontal distance between them.

With the results of the above procedure, which are displayed in figures 10.4 and 10.6, the in-orbit drift can be calculated for the displacement along the z-axis, and the rotations around the x and y axes respectively.

10.4. Results of the Mechanical Analysis

The results of the mechanical analysis are described in this section. It is divided into two parts, the first part is related to the in-orbit drift requirements for the M2 mechanism, while the second part is related to the stability requirements. In subsection 10.4, the conclusions of the results are stated.

In-Orbit Drift

The results regarding the in-orbit drift of the displacement and the rotation of the upper cam of the CORE hinge are shown in figures 10.4 and 10.6, respectively. When compared to the thermal results of the cams, described in section 9.2, it can be seen that the behaviour is very similar. In the first half of the entry phase, the cam displacements decrease, where the upper cam even shrinks a little. After time $t = 378$ s, the temperature of the cams starts to increase, and so does the expansion of the cams. The maximum expansion of the full hinge is at the end of the phase. Here, at time $t = 630$ s, only the upper cam starts to cool down and shrink already. After time $t = 630$ s, the displacement starts to decrease again. The highest displacement is around $0.6 \mu\text{m}$, which is lower than the required $2 \mu\text{m}$ for the whole SMSS.

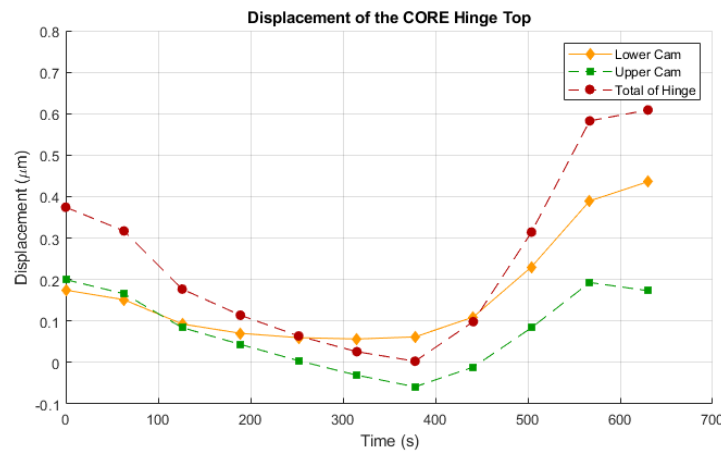


Figure 10.4: Displacement of the CORE hinge top along the optical axis (z)

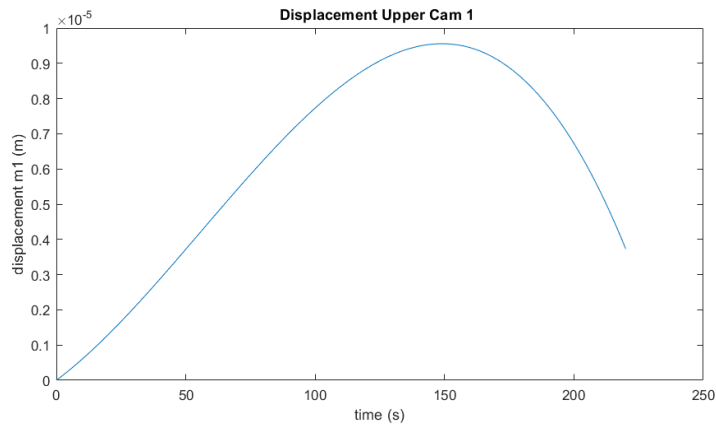


Figure 10.5: Displacement of the upper cam of the CORE hinge along the z-axis

However, according to the analysis of the mechanical model from section 10.2, the maximum value of the vertical displacement is actually $9.8 \mu m$, which is higher than the previous result of $0.6 \mu m$. Therefore, this is the maximum displacement of the upper cam and it is much higher than the maximum displacement stated in the requirements.

The results for the angular in-orbit drift show slightly different behaviour than the lateral in-orbit drift. In the first half of the entry phase, the rotation of the upper cam around the y-axis stays below $0.5 \mu rad$. However, at the moment at which the strips are hit by the sunlight, the rotation quickly rises towards a value of almost $50 \mu rad$. The rotation of the upper cam around the x-axis shows already much more variation and has a much higher value in the first half of the phase than the y-axis rotation; the rotation slightly decreases from 12 to $3 \mu rad$. It is therefore not that surprising that the CORE hinge rotates even more around the x-axis than around the y-axis during the second half of the phase, reaching almost $80 \mu rad$. The most reasonable explanation for these high values of rotation, when compared to the required maximum of $6 \mu rad$, is the variation in radiation that each of the strips receives. The right strip receives more solar radiation than the left strip and the middle strip receives even more radiation than the right strip. Due to this, the vertical displacement along the upper cam varies quite a bit, leading to substantial rotations of the upper cam with respect to the lower cam.

The influence of these rotations on the angular drift of the secondary mirror is more difficult to predict, as this is influenced by the drift of the spider and is thus dependent on each of the four CORE hinges, not only one. To draw conclusions regarding the compliance of the SMSS with the angular in-orbit drift requirements, the displacements of all CORE hinges should be considered, as well as their resulting influence on the drift of the spider. What can be stated, however, is that the fast temperature changes in the CORE hinges can lead to rotations of the secondary mirror that are much bigger than required.

Stability

As described in section 5.3, the stability requirements consider vibrations with a frequency above 1 Hz. By zooming in on the graph in figure 10.5, figure 10.7 is obtained. In this figure, it can clearly be seen that the displacement response of the upper cam actually consists of two additional frequencies that are higher than 1 Hz, namely 3333 Hz and 19600 Hz. The amplitudes for these frequencies are $2E-5 \mu m$ and $4.2E-4 \mu m$, respectively. These are both much lower than the $1 \mu m$ that is specified in the requirements, so according to these results, the stability requirements are easily met by the CORE hinge.

Conclusion of the Mechanical Analysis

It can be concluded from the results presented before, that the CORE hinge stability complies with the requirements of the SMSS. However, during the entry phase, the lateral and angular in-orbit drift of the CORE hinge are higher than the maximum values as stated in the requirements of the secondary mirror support structure. This means that either the other components of the SMSS have to compensate for this, or that the SMSS currently does not comply with the requirements.

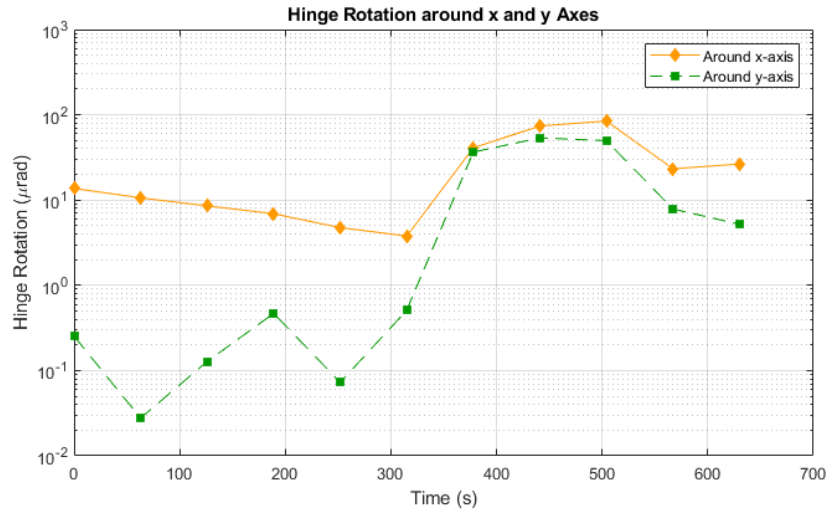


Figure 10.6: Rotations of the upper cam with respect to the lower cam

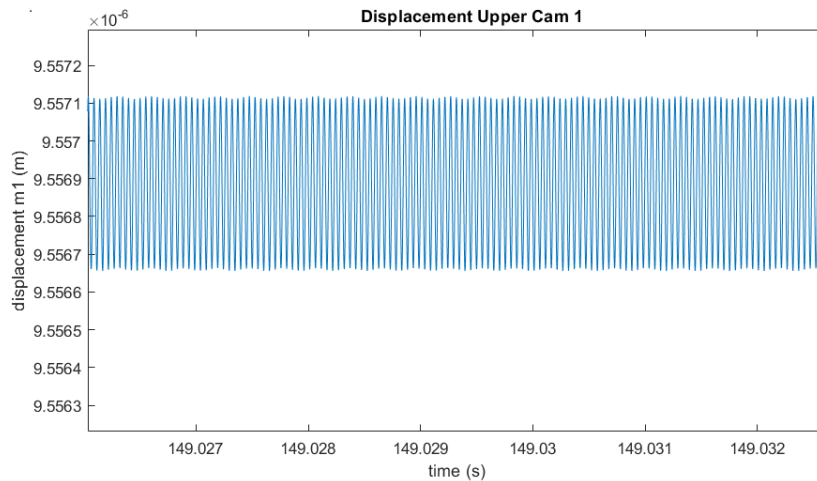


Figure 10.7: Displacement of the upper cam of the CORE hinge along the z-axis

The main cause for the high in-orbit drift within the CORE hinge is the fast increase of the temperature of the strips and the cams to lesser extent, that occurs in the second half of the entry phase. Luckily, a way to solve this problem has been identified. The best way to decrease the rotations and displacements in the CORE hinge is to decrease temperature differences between the different components. As the main cause for the temperature differences in the CORE hinge is the fact that the baffle does not protect the CORE hinge from solar radiation for the whole orbit, it is proposed to elongate the baffle such that it will always protect the CORE hinge from solar radiation. The advised elongation is 0.2 m. This leads to a total length of the baffle of 2.85 m, which is lower than the limit height of 2.9 m [2]. By elongating the baffle, the temperature variations around the hinge will be kept in check, leading to more stable and predictable behaviour, which is beneficial for both the design and operation of the Deployable Space Telescope.

10.5. Discussion of the Mechanical Results

In the previous section, the results of the mechanical analysis have been presented. However, it is worthwhile to keep in mind that some of the assumptions that have been made in the process influence the accuracy of the results when compared with real-life behaviour, although this does not mean that the stated conclusions are invalid. In this section, the limits to the accuracy of the results are discussed.

The first assumption that limits the accuracy of the results is the assumption that the strips are always rigid. As the strips are quite thin, only 0.3mm versus a length of slightly under 80mm, they cannot deal as good with compression as they can deal with tension. For the period when the thermal load is smaller than the preload and the strips shrink, this does not pose a problem, as the strips are under tension. However, from the moment that they expand so much that the thermal load exceeds the preload, which happens in the second half of figure 10.2, the strips will bend away from the cams. Although it has to be taken into account that the preload is increased if the cams expand, this is not enough to compensate for the loss of stiffness. This results in an overestimation of the angular in-orbit drift of the CORE hinge.

Another assumption that has implications for the accuracy of the angular in-orbit drift results is the assumption that the cams will only expand and shrink in de radial direction. Because of the complexity of the cams and the temperature variation along them, the shape of the cams is also likely to change, leading to much more unpredictable behaviour.

The final assumption that will be treated in this section is the assumption that the rotations of the upper cam around different axes are uncoupled. This assumption makes it possible to determine the rotations individually, but in real-life, the different rotations influence each other. Furthermore, in the CORE hinge, the rotation due to the vertical displacements of the two side strips is influenced by the vertical displacement of the middle strip. Because of this, the rotation of the hinge might vary over the width, height or length of the upper cam. This kind of behaviour cannot be determined with the current method.

Because of the reasons described above, it could be useful to perform a more detailed thermo-mechanical analysis of the CORE hinge, which was planned for this thesis originally, in order to get a more detailed and accurate characterisation of the lateral and angular stability and in-orbit drift behaviour of the CORE hinge. Furthermore, the influence of elongating the baffle can be determined to more detail. It is expected that the best results can be achieved with a computer program, like SINAS IV.

It is however debatable how much such an analysis would contribute to the DST project. An analysis of the full secondary mirror support structure, including a simple representation of the CORE hinges, has been performed by Ilja Akkerhuis [1], whose thesis ran nearly parallel to this thesis. Because of this, a more detailed analysis of the DST CORE hinge is not considered necessary.

11

Conclusions

The Deployable Space Telescope is a space telescope that uses foldable optical elements in order to achieve mass and volume reductions compared to state-of-the-art telescopes, without limiting the ground resolution of the telescope. The project, which was initiated in 2014, has gone through the preliminary optical and mechanical design phases and is currently nearing the end of the conceptual mechanical design phase. However, before the detailed mechanical design can be started, there is a need for an analytical characterisation of the thermal behaviour of the CORE hinges in the Secondary Mirror Support Structure (SMSS) in order to determine whether the current design of the CORE hinges complies with the functional requirements of the SMSS. The goal of this thesis is therefore to fulfil this need by performing a thermal and mechanical analysis of the CORE hinge, with the end goal of determining the compliance of the hinge with the SMSS requirements.

To determine the compliance of the CORE hinge design to the requirements, a mechanical analysis will be performed, the inputs to which come from a thermal analysis of the CORE hinge. For the thermal analysis, several methods are possible. The selected method is called the combination method and combines the use of a geometric model for determining the inputs to the thermal model with the flexibility of using only a thermal model.

Although a thermal and geometric model of the DST had already been built, it was decided to build a completely new model, as the representation of the CORE hinge in the DST model was inaccurate. The most detailed part of this model is the CORE hinge itself, which has been modelled with 90 % accuracy, while the non-CORE hinge components were simplified. The thermal model of the CORE hinge was created separately from the geometric model but the nodes in the thermal model correspond exactly to the nodes in the geometric model. The non-CORE hinge geometries, on the other hand, are included in this model as boundary nodes only.

The fact that ESATAN was selected to perform the thermal analysis has implications for the accuracy of the results. ESATAN uses the lumped parameter method, which has a much rougher mesh than, for instance, the finite-element method. However, it has been verified that the thermal results of the lumped parameter model of the CORE hinge are only slightly different from the results of the finer meshed finite-element method; the difference was only one percent on average, with a maximum difference of three percent. This implies that the software selection does not influence the applicability of the results.

During the entry phase, which is the phase right before the DST enters the eclipse part of its orbit, the highest temperatures of the CORE hinge are reached, as well as the fastest temperature changes. Especially the temperature of the right and middle strips that connect the two cams shows unstable behaviour during this phase. The middle strip has the highest maximum temperature, which is equal to 18 °C, while the left strip has a maximum average temperature of only 11 °C. This difference is caused by the variation in sunlight along the CORE hinge. Surprisingly, the lower cam records the highest temperature of the two cams, with a maximum average temperature 14 °C against 8.5 °C for the upper cam.

Although valuable results have been obtained, two improvements of the thermal analysis have been identified. With these improvements, the temperature distribution of the CORE hinge will be determined more often than the current 63 seconds interval. Furthermore, the influence of the baffle on the thermal behaviour of the hinge would be represented more accurately.

According to the results of the mechanical analysis, the CORE hinge design satisfies the requirement for the lateral stability along the optical axis of the CORE hinge, with a stability of $4.2 \cdot 10^{-4} \mu m$. However, the in-orbit drift requirement is not satisfied, with a maximum drift of $9.8 \mu m$. Furthermore, the angular in-orbit drift requirement around the x and y axes is not satisfied, with a maximum drift of 80.5 and $54 \mu rad$, respectively.

Because the focus of this thesis has shifted more towards the thermal analysis, the mechanical model has been made less detailed and the method for the thermo-mechanical analysis has been changed. For this method, three assumptions have been made that decrease the modelling accuracy of the mechanical analysis as opposed to a full thermo-mechanical analysis.

However, although the accuracy of the analysis has its limits, it can be concluded that the baffle of the Deployable Space Telescope is too short to protect the CORE hinge from solar radiation for the whole orbit. Due to this, the secondary mirror support structure (SMSS) shows in-orbit drift behaviour that does not comply with the functional requirements. Therefore, it is advised to increase the baffle length from 2.65 m to 2.85 m, such that the CORE hinge is fully protected from solar irradiation. When this is done, there is no reason to assume that the CORE hinge is unsuited for the SMSS and it is not necessary to look for alternatives.

12

Recommendations

Several recommendations for future work have been identified in addition to the recommendation to elongate the baffle that was presented in the conclusions. This includes activities that can be done to build forward upon this thesis and activities that could be done to improve the current work. These recommendations are presented in this chapter.

Up until this moment, an analytical characterisation of the CORE hinge of the Deployable Space Telescope has been carried out. Furthermore, mechanical and thermal test have been conducted with a prototype of the CORE hinge [39][23] and a thermo-mechanical analysis of the SMSS have been carried out [1]. It is recommended to perform an experimental mechanical analysis of the SMSS, as this is a good next step in the design and analysis of the Deployable Space Telescope. The goal of these tests should be to characterise the macro and micro-dynamic behaviour of the SMSS to determine its compliance with the stability and in-orbit drift requirements. This can then be combined with the results of the thermo-mechanical analysis of the SMSS to draw definitive conclusions on the design of the SMSS and to determine whether design changes are necessary.

However, not enough is known yet about the operational loadings that the SMSS is subjected to [39]. This includes loads during launch, deployment and operational loads. Therefore, it is necessary to first determine the operational mechanical loadings that the SMSS is subjected to before the tests are carried out.

The second recommendation has to do with the solid geometries in ESATAN. In subsection 6.3.2, it is stated that building a relatively small geometric model solely out of solid geometries is expected to be inaccurate. However, it would be beneficial if an accurate model of the CORE hinge could be included in the geometric model of the DST. This has several reasons. The first reason has to do with the thermal model of the CORE hinge. Instead of translating the non-CORE hinge geometries into a limited number of boundary nodes, these geometries can be represented by many nodes, like in the geometric model, without much extra work. Furthermore, it will be very easy to increase or decrease the mesh size, or to apply other changes to these components. Due to this, the thermal and geometric models will be much more flexible and it will be much easier to determine the influence of different design choices.

To find out what the influence of the solid nodes is on the model, it is recommended to research the influence of solid geometries on the result of the DST thermal analysis. If this has only minor influence, then a thermal analysis of the full DST could be performed with a model of the DST that includes an accurate representation of the CORE hinges. This would lead to useful information for the mechanical testing about the operational loads that the SMSS is subjected to by the thermal and radiation environment of the DST.

Bibliography

- [1] I. Akkerhuis. Deployable Space Telescope: Redesign of the Secondary Mirror Support Structure. *Delft University of Technology*, 2020.
- [2] J.W. Arink. Thermal-mechanical design of a baffle: for the deployable space telescope. Master's thesis, Delft University of Technology, 2019.
- [3] B. Bhushan. *Modern tribology handbook. 1. Principles of tribology*. CRC press, 2001.
- [4] R.V. Cadman. Rolamite-geometry and force analysis. *Journal of Manufacturing Science and Engineering*, 91(1):186–191, 1969.
- [5] J.R. Cannon. Compliant mechanisms to perform bearing and spring function in high precision applications. Master's thesis, Brigham Young University-Provo, 2004.
- [6] J.A. Clark and M.E. Korybalski. Algebraic methods for the calculation of radiation exchange in an enclosure. *Wärme-und Stoffübertragung*, 7(1):31–44, 1974.
- [7] M. Corvers. Design of a primary mirror deployment mechanism for a deployable space telescope. Master's thesis, Delft University of Technology, 2018.
- [8] D. Dolkens. A deployable telescope for sub-meter resolutions from microsatellite platforms. Master's thesis, Delft University of Technology, 2015.
- [9] D. Dolkens and J.M. Kuiper. Design and end-to-end modelling of a deployable telescope. In *International Conference on Space Optics—ICSO 2016*, volume 10562, page 1056227. International Society for Optics and Photonics, 2017.
- [10] D. Dolkens, J.M. Kuiper, B.T.C. de Goeij, and E.K.A. Gill. Design and Optimization of a deployable telescope for earth observation. *Delft University of Technology*, 2016.
- [11] ESTEC/ESA. Sinas IV: Interpolation of lumped parameter thermal node temperatures (from e.g. ESATAN) to thermo-elastic input data (with MSC.NASTRAN). URL <https://exchange.esa.int/restricted/sinas/>. Accessed on 2020-09-22.
- [12] T.R. Gritter. Literature review. *Delft University of Technology*, 2020.
- [13] P.A. Halverson. Multi-stable compliant rolling-contact elements. Master's thesis, Brigham Young University-Provo, 2007.
- [14] P.A. Halverson, L.L. Howell, and S.P. Magleby. Tension-based multi-stable compliant rolling-contact elements. *Mechanism and Machine Theory*, 45(2):147–156, 2010.
- [15] J.D. Hinkle, L.D. Peterson, K. Klein, M. Levine, and C.Y. Peng. Submicron friction mechanics at ambient and cryogenic temperatures. In *UV/Optical/IR Space Telescopes: Innovative Technologies and Concepts II*, volume 5899, page 589910. International Society for Optics and Photonics, 2005.
- [16] P. Kansakar and F. Hossain. A review of applications of satellite earth observation data for global societal benefit and stewardship of planet earth. *Space Policy*, 36:46–54, 2016.
- [17] E.A. Korhonen. Design of a deployable baffle for the deployable space telescope. Master's thesis, Delft University of Technology, 2019.
- [18] A. Krikken. Design of the Secondary Mirror Support Structure. Masters' Thesis. *Delft University of Technology*, 2018.

- [19] M.S. Lake and M.R. Hachkowski. Design of mechanisms for deployable, optical instruments: Guidelines for reducing hysteresis. *Langley Research Center*, 2000.
- [20] M.S. Lake, P.A. Warren, and L.D. Peterson. A revolute joint with linear load-displacement response for a deployable lidar telescope. *American Institute of Aeronautics and Astronautics*, 1996.
- [21] M.S. Lake, L.D. Peterson, M.R. Hachkowski, J.D. Hinkle, and L.R. Hardaway. Research on the problem of high-precision deployment for large-aperture space-based science instruments. In *AIP Conference Proceedings*, volume 420, pages 188–198. AIP, 1998.
- [22] M.S. Lake, J.E. Phelps, J.E. Dyer, D.A. Caudle, A. Tam, J. Escobedo-Torres, and E.P. Kasl. Deployable primary mirror for space telescopes. In *Advanced Telescope Design, Fabrication, and Control*, volume 3785, pages 14–25. International Society for Optics and Photonics, 1999.
- [23] S. Leegwater. An Experimental Characterisation of Mechanical and Thermal Behaviour in CORE Hinges. Masters' Thesis. *Delft University of Technology*, 2019.
- [24] Engineering Library. Coefficient of friction, 2020. URL <https://engineeringlibrary.org/reference/coefficient-of-friction>. Accessed on 2020-10-01.
- [25] J.W. Lopes Barreto. Deployable space telescope: Optimal boom design for high precision deployment of the secondary mirror. Master's thesis, Delft University of Technology, 2017.
- [26] ITP Engines UK Ltd. *ESATAN-TMS Thermal Engineering Manual*, volume 1. ITP Engines UK Ltd., 2015.
- [27] H.M.Y.C. Mallikarachi and S. Pellegrino. Optimized designs of composite booms with tape spring hinges. In *51st AIAA/ASME/ASCE/AHS/ASC Structures, Structural Dynamics, and Materials Conference 18th AIAA/ASME/AHS Adaptive Structures Conference 12th*, page 2750, 2010.
- [28] Maptiler. The beauty of our planet from space, 2018. URL <http://www.maptiler.com/blog/2018/06/the-beauty-of-our-planet-from-space.html>. Accessed on 2019-12-23.
- [29] AZO Materials. Titanium and titanium alloys - wear behaviour and lubrication, 2004. URL <https://www.azom.com/article.aspx?ArticleID=2618>. Accessed on 2020-10-01.
- [30] A. Merstallinger, M. Sales, E. Semerad, and B.D. Dunn. Assessment of cold welding between separable contact surfaces due to impact and fretting under vacuum. *ESA Scientific & Technical Memoranda*, 279: 57, 2009.
- [31] D. Risselada. Phase diversity for the deployable space telescope. Master's thesis, Delft University of Technology, 2018.
- [32] N. Sclater and N.P. Chironis. *Mechanisms and mechanical devices sourcebook*, volume 2. McGraw-Hill New York, 1996.
- [33] S. Seriani and P. Gallina. A storable tubular extendible member (stem) parallel robot: Modelization and evaluation. *Mechanism and Machine Theory*, 90:95–107, 2015.
- [34] Engineering ToolBox. Rolling friction and rolling resistance, 2008. URL https://www.engineeringtoolbox.com/rolling-friction-resistance-d_1303.html. Accessed on 2020-10-01.
- [35] G. van Marrewijk. Design of an aberration correction system for a deployable space telescope. Master's thesis, Delft University of Technology, 2018.
- [36] B.T. Van Putten. Design of the deployment mechanism for the primary mirror elements of a deployable space telescope. Master's thesis, Delft University of Technology, 2017.
- [37] T.T.D. Van Wees. Thermal modelling and analysis of the deployable space telescope. Master's thesis, Delft University of Technology, 2019.
- [38] M.G.S. Voorn. Deployment Mechanisms of the Deployable Space Telescope: Literature Study Review. *Delft University of Technology*, 2018.

-
- [39] M.G.S. Voorn. Initiating the Testing Phase of a Deployable Space Telescope. Masters' Thesis. *Delft University of Technology*, 2019.
- [40] K.F. Wakker. *Fundamentals of Astrodynamics, Lecture Notes AE4874*. TU Delft, Faculty of Aerospace Engineering, 2015.
- [41] P.A. Warren and L.D. Peterson. Experimental characterization of the nonlinear post-deployment micro-mechanics of precision deployable space structures. In *37th Structure, Structural Dynamics and Materials Conference*, page 1586, 1996.
- [42] P.A. Warren, L.D. Peterson, and J.D. Hinkle. Submicron mechanical stability of a prototype deployable space telescope support structure. *Journal of spacecraft and rockets*, 36(5):765–771, 1999.
- [43] C.V. White and M.B. Levine. Microdynamic issues in large deployable space telescopes. In *Optomechanical Engineering 2000*, volume 4198, pages 163–171. International Society for Optics and Photonics, 2001.
- [44] D.F. Wilkes. Rolamite-a new mechanical design concept. 1967.
- [45] D.F. Wilkes. Roller-band devices, 1969. US Patent 3,471,668.

A

Results of Thermal Analysis

In this appendix, several additional figures are placed to the figures present in chapter 9, which provide a slightly more detailed insight in the results of the thermal analysis. Four figures are included for both the entry and exit phases of the analysis.

A.1. Entry Phase

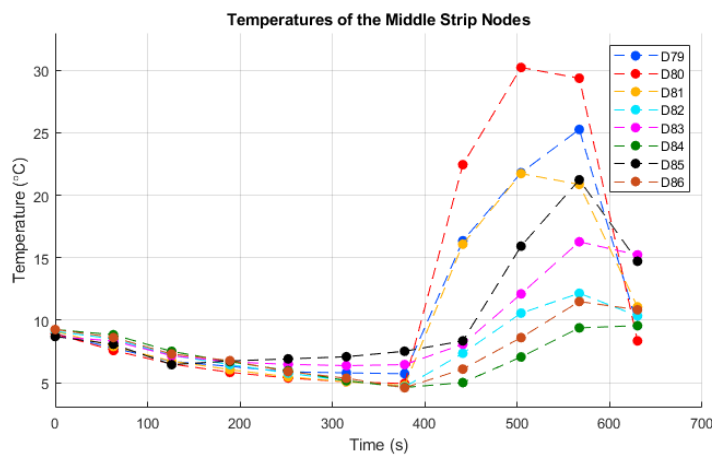


Figure A.1: Temperature progression of all nodes of the middle strip for the entry phase

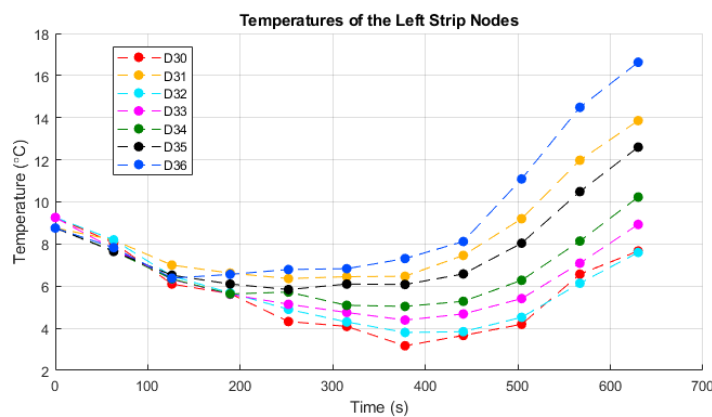


Figure A.2: Temperature progression of all nodes of the left strip for the entry phase

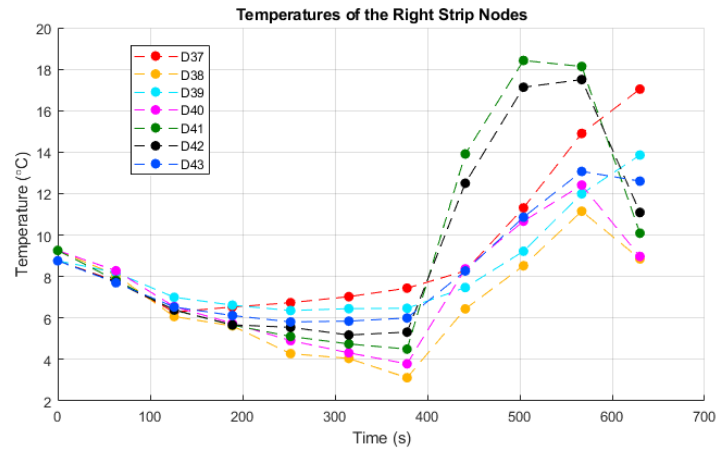


Figure A.3: Temperature progression of all nodes of the right strip for the entry phase

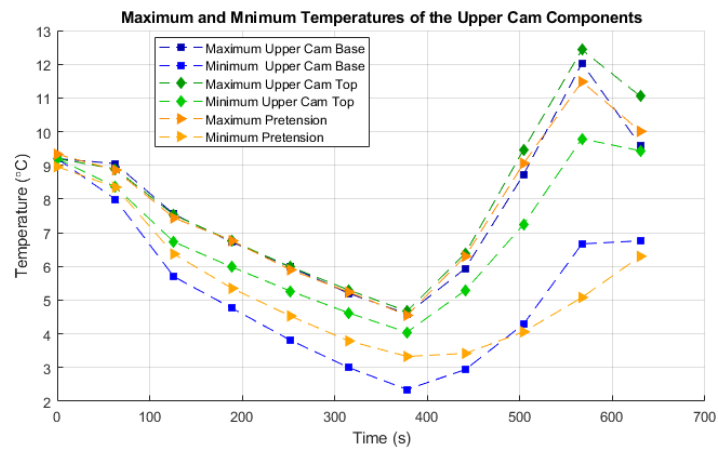


Figure A.4: Minimum and maximum temperatures of the main upper cam components for the entry phase

A.2. Exit Phase

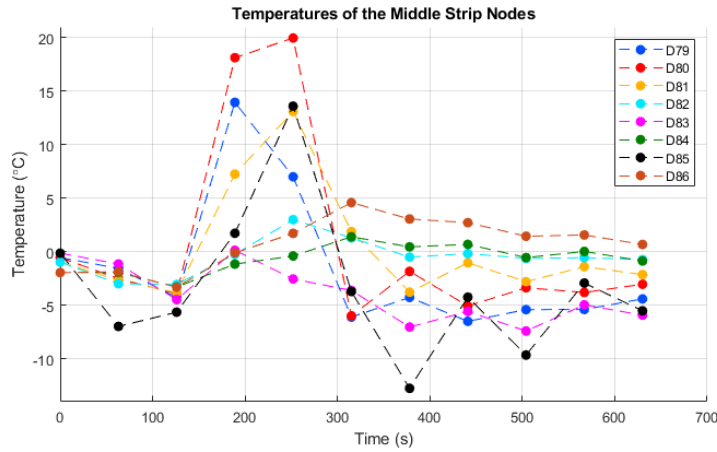


Figure A.5: Temperature progression of all nodes of the middle strip for the exit phase

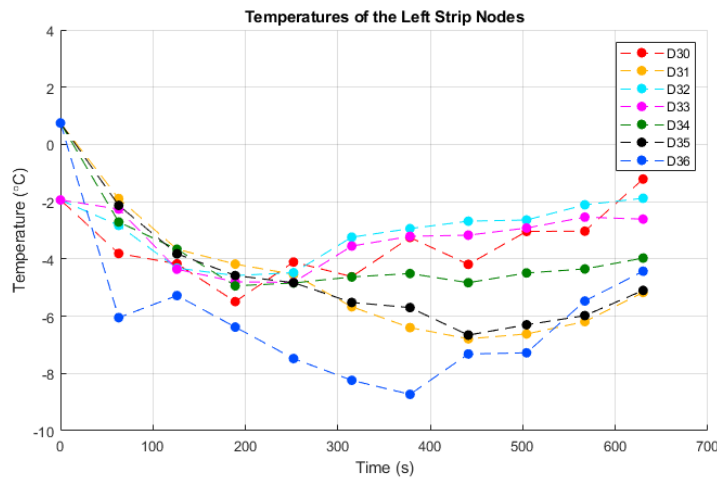


Figure A.6: Temperature progression of all nodes of the left strip for the exit phase

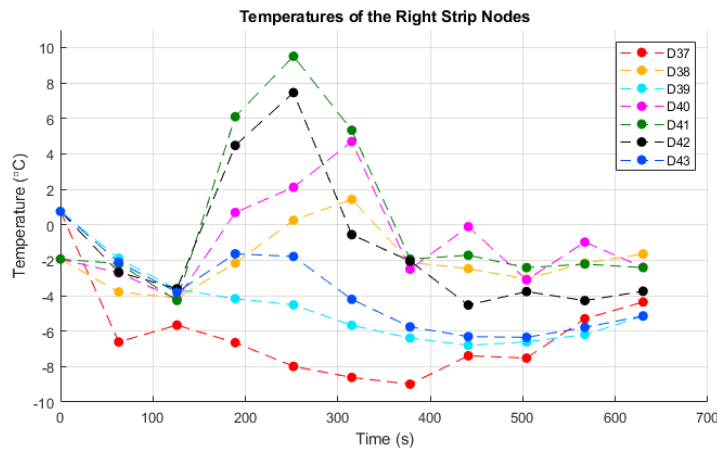


Figure A.7: Temperature progression of all nodes of the right strip for the exit phase

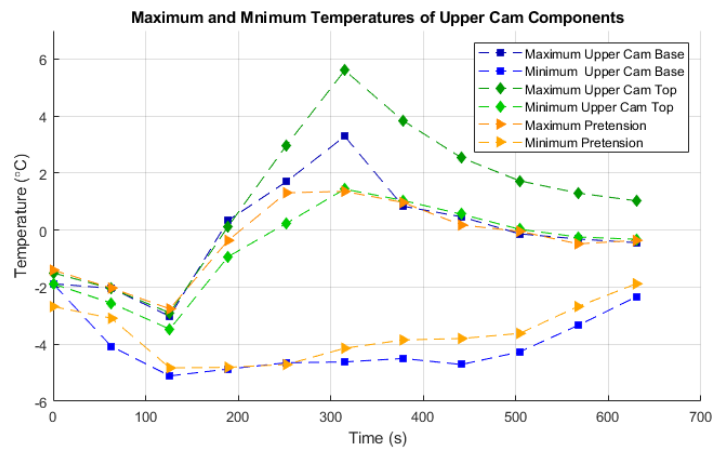


Figure A.8: Minimum and maximum temperatures of the main upper cam components for the exit phase

B

Requirements

In this appendix, the relevant functional requirements described in section 5.4 are shown. The following six requirements regard the in-orbit drift.

M2-MEC-10 *The M2 mechanism in-orbit drift shall be equal or less than 4 μm measured along the X axis of the telescope coordinate frame.*

M2-MEC-11 *The M2 mechanism in-orbit drift shall be equal or less than 4 μm measured along the Y axis of the telescope coordinate frame.*

M2-MEC-12 *The M2 mechanism in-orbit drift shall be equal or less than 2 μm measured along the Z axis of the telescope coordinate frame.*

M2-MEC-13 *The M2 mechanism in-orbit drift shall be equal or less than 6 μrad measured around the X axis of the telescope coordinate frame.*

M2-MEC-14 *The M2 mechanism in-orbit drift shall be equal or less than 6 μrad measured around the Y axis of the telescope coordinate frame.*

M2-MEC-15 *The M2 mechanism in-orbit drift shall be equal or less than 12 μrad measured around the Z axis of the telescope coordinate frame.*

The following six requirements regard the M2 mechanism stability.

M2-MEC-18 *The M2 mechanism stability shall be equal or less than 4 μm measured along the X axis of the telescope coordinate frame.*

M2-MEC-19 *The M2 mechanism stability shall be equal or less than 4 μm measured along the Y axis of the telescope coordinate frame.*

M2-MEC-20 *The M2 mechanism stability shall be equal or less than 2 μm measured along the Z axis of the telescope coordinate frame.*

M2-MEC-21 *The M2 mechanism stability shall be equal or less than 6 μrad measured around the X axis of the telescope coordinate frame.*

M2-MEC-22 *The M2 mechanism stability shall be equal or less than 6 μrad measured around the Y axis of the telescope coordinate frame.*

M2-MEC-23 *The M2 mechanism stability shall be equal or less than 12 μrad measured around the Z axis of the telescope coordinate frame.*
